Theory of Microwave to Optical Photon Upconversion Using Erbium Doped Crystals

Peter Somerville Barnett

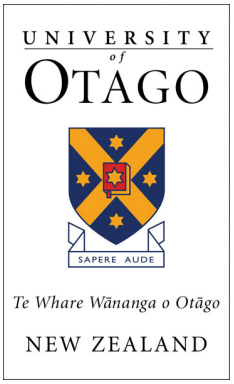

A thesis submitted for the degree of

Master of Science

at the University of Otago,
Dunedin, New Zealand

November 2019

Abstract

The subject of this thesis is coherent conversion from microwave photons to optical photons. This has applications for quantum computing, and would allow interfacing between superconducting qubits and optical fibres. Specifically, we will focus on photon conversion via erbium ions in a doped crystal.

We model a device which has an erbium doped crystal inside overlapping microwave and optical cavities. Input microwave photons are combined with photons from an optical pump laser via interactions with the erbium ions. This will produce optical output photons carrying the same quantum information as the input microwave photons. We develop a description of the interaction between the atoms and the light fields, accounting for both loss effects in the single atoms, and inhomogeneous broadening of the ensemble. Our theory is compared with experimental data, and shows good agreement.

We explore various phenomena which arise in this system, including the effects of temperature and microwave power.

It is shown that the description of this device from earlier work is not valid in the regime where the conversion efficiency is greatest. Hence, this work is necessary to be able to predict the maximum conversion efficiency.

We develop a linearised model which is accurate in the regime where the microwave and optical fields are small, such as the regime used for quantum information. This model is used to maximise the photon number conversion efficiency of the device. We predict conversion efficiencies above 20%, far higher than has been achieved experimentally with using rare earth ions. Modifying our device should further increase the conversion efficiency to above 80%.

Acknowledgements

Firstly, I need to thank my supervisor Assoc. Prof. Jevon Longdell. Your support, knowledge and positivity has been much appreciated, and much needed during this past year. I am amazed by your ability to explain complicated subjects intuitively and with patience. Thanks for taking me on as a theory student in an experimental lab, and thank you for cultivating a great working environment in LTJ.

Thank you to the other members of LTJ for good company and discussion throughout the year. I especially need to thank Gavin King, who performed the experiments mentioned in this thesis, and who always had time to explain them to me.

I've enjoyed my time in the physics department over the past few years, and I'm grateful to all the people, past and present, who have kept things running smoothly.

Thank you to the Sangster household, for housing me and giving me some respite from Dunedin while finishing this thesis.

Thanks to my friends inside and outside the physics department, without whom life would be a lot more miserable.

And thank you to my family for their constant support and care.

Peter Barnett, December 2019

Truth ... is much too complicated
to allow anything but approximations

JOHN VON NEUMANN

Contents

Chapter 1

Introduction

In this introductory chapter we will outline the motivation and potential application for this research. This will begin with an overview of quantum computing; why people want to build quantum computers and what problems they may be able to solve, and what approaches there are to realising quantum computing hardware.

We will outline the application of microwave to optical photon upconversion for quantum computing, and discuss various methods being proposed and demonstrated. This work will focus on a method for upconversion using rare earth ions, and so we will discuss the various atomic properties that make rare earth ions well suited to this application. Finally, this chapter will end with an outline of this thesis, including which parts are original work.

1.1 Quantum Computing

Quantum computing is a much hyped technology, promising faster algorithms and more secure encryption than is physically possible using classical computers. However, the hardware for actually performing useful quantum computations is still in its infancy. Recently, for the first time a quantum computer has been able to perform a task faster than is currently possible using a classical computer [1]. While this is a significant achievement, the computation performed was specifically designed to show that a quantum computer can solve some problems faster than a classical computer. For quantum computers to perform useful computations the hardware must be developed further.

The key difference between classical and quantum computers comes from how they store and process information. Classical computers typically store the information in *bits*, which must take one of two possible values usually

denoted 0 and 1. Computation is performed using logic gates, which return 0 or 1 based on the input from one or more bits. For example in classical computation, an AND gate will return 1 if both of the inputs are 1 and will return 0 otherwise, while the OR gate will return 1 if either of the inputs are 1.

For a quantum computer the information is stored as quantum bits or *qubits*, which can exist in a coherent superposition of both 0 and 1 states [2]. Similarly to classical computation, quantum computation is performed by applying quantum logic gates, which will take the state of one or more qubits and will return an output. The output may be a superposition state, and additionally two or more output states may be entangled [3]. The properties of superposition and entanglement for qubits mean that there are fundamentally different tools available to use in quantum algorithms compared with classical algorithms. This means that quantum computers should be able to perform some calculations faster than is possible with classical computers.

A classic example of a quantum algorithm that can outperform classical computers is Shor's algorithm for integer factorisation [4]. This algorithm is able to find the prime factors of an integer in polynomial time, much faster than the current best classical alternative. This caused a stir because RSA encryption, one of the most widely used encryption algorithms, relies on it being computationally intractable to factorise large integers. As it stands RSA encryption is secure from current classical algorithms, which are very slow to factorise large integers [5]. With a powerful enough quantum computer, Shor's algorithm would be able to break RSA encryption. This isn't currently a worry because to date the largest integer which has been factorised is 15 [6, 7], far smaller than what would be required to break RSA encryption[1].

A less sinister example is the HHL algorithm for solving linear systems of equations [10]. This is an algorithm for solving the system of linear equations $\mathbf{A}x = b$, where $\mathbf{A}$ is an $n \times n$ matrix. This algorithm can solve this system of equations in time logarithmic in n, given certain constrains on $\mathbf{A}$, including that $\mathbf{A}$ must be invertible and have a low condition number [11]. For a classical algorithm the time would scale as n^2 for merely reading the elements in A, and so the time would increase even more than this to solve the system of equations. This algorithm could prove very useful because solving systems of linear equations has wide ranging and important applications including modelling electrical networks [12], finite element problem solving [13] and machine learning [14].

To actually implement these quantum algorithms we need to build a

[1]Integer factorisation of 21 has been reported using a version of Shor's algorithm [8], although this is disputed [9].

quantum computer. The quantum computation will be performed by applying quantum logic gates to a system of qubits. Physically, a qubit can be any two state quantum system which will encode the $|0\rangle$ and $|1\rangle$ states. Current examples of qubits include trapped ions [15], ultracold atoms in optical lattices [16, 17], atomic nuclear spins [18], quantum dots [19, 20], photons [21], and nitrogen valency centres in diamond [22].

One of the main qubit designs currently used are superconducting qubits [23, 24]. These are essentially a simple circuit which comprises a loop of superconducting wire with a capacitor and a Josephson junction [25]. With just the loop and capacitor this would be a simple LC circuit, which acts as a quantum harmonic oscillator and hence has equally spaced energy levels. This would mean that more than two of the energy levels will be accessible, because the same frequency that drives the circuit into the first excited state could further drive it into higher states. The Josephson junction is included to allow the circuit to act as a two state system. This introduces a nonlinearity, which means that the energy levels will no longer be equally spaced. If the transition frequencies are different enough such that the frequency driving the first transition will not drive any other transitions then we can ignore all the other energy levels and treat this as a two state system.

Superconducting qubits generally operate at microwave frequencies. This means the energy difference between the $|0\rangle$ and $|1\rangle$ states is generally in the 5-10 GHz range. Because of this small energy gap the effects of thermal noise can be very large, and superconducting qubits generally need to be cooled to around 20 mK.

Working at microwave frequencies has significant disadvantages for transmitting the quantum information. Several proposals for quantum networks [26] and distributed quantum computing would require us to be able to send quantum information between devices without destroying the coherence and entanglement between qubits [27]. When transmitting information using microwave photons via coaxial cables there are relatively large losses of around 1 dB/m which makes transmitting information over even moderate distances undesirable. Additionally, the effect of thermal noise can overwhelm the signal from the microwave photons. On the other hand, optical photons have energies several orders of magnitude larger than microwave photons and so are immune to the same loss and thermal noise effects. Optical photons can also be transmitted very long distances with little attenuation via optical fibres. The minimum attenuation in typical silica optical fibres is 0.2 dB/km, for light with a wavelength of 1550 nm. This has the additional advantage that there is already optical fibre infrastructure in place for the conventional internet, so it would be convenient to be able to use this infrastructure for our quantum networks.

This means it would be convenient to be able to convert from the microwave photons, which interface with our superconducting qubits, to optical photons which can be efficiently transmitted long distances. For this conversion process, it is essential that the quantum coherence remains intact, this means the input microwave photons and the output optical photons must have the same relative phase. This process of converting photons of a lower frequency to a higher frequency is called *upconversion*, specifically we are looking at microwave to optical upconversion.

1.2 Microwave to Optical Upconversion

There are several experimental approaches for achieving microwave to optical upconversion that we will discuss in this section [28]. At its core this upconversion process involves converting a microwave photon, with frequency around 5–10 GHz, to optical light[2]. Often the upconverted light has a wavelength of around 1550 nm to correspond to the minimum attenuation window in silica fibres, this corresponds to a frequency of around 193 THz. The upconverted optical photons will have several orders of magnitude more energy than the input microwave photons. To achieve this increase in frequency, microwave to optical upconversion involves combining an input microwave photon, with one or more optical photons, such that the output is an optical photon with the same relative phase as the microwave photon. Each of the different approaches for microwave to optical upconversion aim to mediate an interaction between the microwave photons and input optical light such that they be combined.

1.2.1 $\chi^{(2)}$ Nonlinear Materials

Some systems for upconversion use nonlinear optical materials with a large $\chi^{(2)}$ nonlinearity [29, 30, 31]. In standard linear materials two electromagnetic fields can exist in a superposition and not interact with each other. However in nonlinear materials, if the combined electric field is large enough then the two fields may interact. For upconversion, the $\chi^{(2)}$ nonlinearity allows the input microwave field to interact with the electric field from an input optical pump and create an output field with frequency equal to the sum of the input frequencies.

For these systems to work, the optical electric field inside the nonlinear material must be very large, and so these systems often use whispering gallery

[2]For this work we are including near-infrared light, with wavelengths up to 2500 nm in the definition of optical light.

mode resonators made out of nonlinear materials [32, 33]. These can be placed inside a microwave cavity to enhance the microwave field.

1.2.2 Optomechanical Systems

Currently the upconversion systems with the highest conversion efficiency are optomechanical systems. In these systems the microwave field and the optical field are both coupled to a mechanical resonator, which mediates the interaction between the fields [34, 35]. In one such system the microwaves were coupled to an LC circuit, where one of the capacitor plates was connected to a mechanical resonator [36]. The mechanical resonator was also connected to a membrane at one of the nodes of an optical Fabry–Pérot cavity, as the membrane moves it shifts the position of the node in the cavity and so will affect the wavelength of the cavity. The Fabry–Pérot was also strongly driven by a pump laser. Using an optomechanical system, conversion efficiencies as high as 47% have been achieved [37].

1.2.3 Rydberg Atoms

A novel approach to upconversion has been demonstrated using clouds of ultracold Rydberg atoms [38, 39]. Rydberg atoms have very large electric dipole moments for transitions ranging from microwave to optical frequencies [40]. These large dipole moments mean that the transitions can be very strongly coupled to the microwave and optical fields. To achieve upconversion using Rydberg atoms, several different transitions are pumped, in such a way that when a microwave field excites one of the transitions this will lead to an output photon of the desired optical frequency.

1.2.4 Collective Spin Systems

In magnetically ordered materials microwaves are able to excite collective spin excitations called magnons [41, 42, 43]. These magnons are able to interact with input optical light either via Brillouin scattering or by exciting some kind of electronic transition, such that they can output an upconverted optical photon. This has been demonstrated in yttrium iron garnet resulting in low conversion efficiencies [44], and proposed using rare earth crystals [45].

1.2.5 Rare Earth Ion Doped Crystals

Finally, crystals doped with rare earth ions can be used for upconversion, which is the focus of this thesis. In these systems, each rare earth ion is used

as a three level system. One of the ground hyperfine levels can be split by an applied magnetic field into two spin states separated by a microwave transition. The third level will be one of the electronic excited states, separated from the lower states by optical transitions. A pump laser is applied to drive one of the optical transitions, such that when a microwave photon excites the spin transition, it will be further driven in the electronic excited state. The atom will then decay into the ground state, emitting an upconverted optical photon.

Specifically, this thesis will focus on using a crystal of yttrium orthosilicate (Y_2SiO_5) commonly called YSO, doped with erbium ions. Erbium is especially of interest because it has an optical transition of 1536 nm, which makes it very well suited for generating photons to send via optical fibres. To date the highest conversion efficiency achieved using rare earth ions used a crystal of Er:YSO, and the conversion efficiency was 1.26×10^{-5} [46].

1.3 Rare Earth Ions

The rare earths elements are a series of elements in the periodic table ranging from lanthanum (atomic number 57) to lutetium (atomic number 71)[3]. In this section we will discuss the properties of the rare earths which make them promising candidates for upconversion. At the end there will be a discussion on the specific properties of erbium, because this is the element which this thesis will focus on.

1.3.1 Atomic and Ionic Properties

The rare earths all have very similar chemical properties, mainly due to their electron configuration. In their ionic forms, the rare earths are almost always found in the 3+ oxidation state, meaning that they have a charge of +3, with a few exceptions for 2+ and 4+ ions.

In the 3+ oxidation state the rare earth ions will generally have full 5s, 5p and 6s orbitals, and 4f orbitals will only be partially full. Interesting properties arise because the electrons in the partially full 4f orbitals are held closer to the nucleus than the 5s, 6s and 5p electrons (Figure 1.1). This means that the further out 5s, 5p and 6s electrons can screen the inner 4f

[3]Scandium and yttrium have similar chemical properties and so are often included as part of the rare earths [47]. For this discussion of the rare earths we will leave them out because they have different electronic properties, due to the lack of 4f electrons, and so are not particularly relevant for our purposes. The subset that we are considering is also called the lanthanides or lanthanoids.

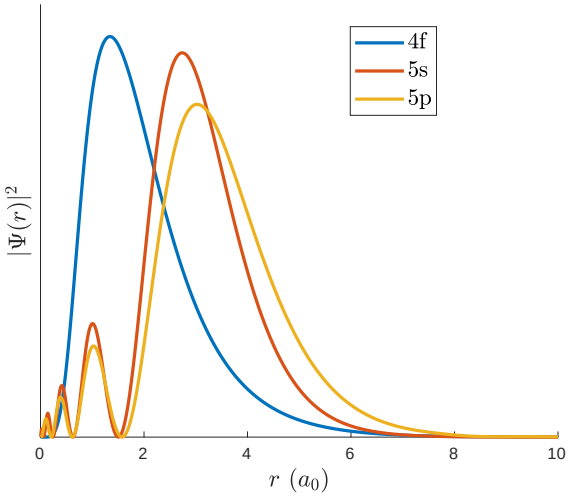

Figure 1.1: The radial electron density for the rare earth ion Pr^{3+} for the 4f, 5s and 5p orbitals. The distance from the nucleus r is measured in units of the Bohr radius a_0. The electron density of the 4f orbital is significantly closer to the nucleus than the 5s and 5p orbitals. The data is from for this figure is from [48].

electrons from the effects of the environment (including from the effects of a host lattice). Electronic 4f–4f transitions in the rare earths range from UV to IR, and due to the effect of screening these transitions can have very narrow linewidths. These linewidths remain narrow even when the ions are doped into a host lattice.

Rare earth ions are usually doped into crystals containing Y^{3+} or La^{3+} ions because these have similar atomic radii to most rare earth ions. This means that a rare earth dopant ion can be substituted for a Y^{3+} or La^{3+} ion without much distortion of the host lattice.

1.3.2 Linewidths

For ions doped into a crystal, each transition is associated with two different linewidths. The homogeneous linewidth is the linewidth for a transition of a single ion, while the inhomogeneous linewidth is the linewidth associated with the entire ensemble of dopant ions inside the crystal.

Homogeneous Broadening

The homogeneous linewidth is the linewidth of a transition for a single atom, and as its name suggests it is the same for all the dopant ions in a crystal. Homogeneous broadening arises from the decay of the single atom transitions.

For a single ion, each transition has a homogeneous linewidth Γ_h, which is related to the coherence time T_2 of the transition,

$$\Gamma_h = \frac{1}{T_2} \tag{1.1}$$

If there were no other processes causing the excited state of a transition to lose population, the coherence time would be related to the excited state population lifetime T_1 by $T_2 = 2T_1$. However, there will be additional loss effects due to interactions with the environment which cause the excited state to lose coherence and increase the homogeneous broadening, so in general,

$$T_2 \leq 2T_1$$

We can characterise these additional processes with an additional dephasing rate Γ_D,

$$\frac{1}{T_2} = \frac{1}{2T_1} + \Gamma_D \tag{1.2}$$

Often the additional dephasing effects will be much greater than the excited state population decay rate, and so they will primarily determine the homogeneous linewidth Γ_h. The additional dephasing will be due to interactions with the environment that the ion is in, such as interactions with the host lattice and other dopant ions.

Inhomogeneous Broadening

When measuring the absorption or transmission for a rare earth doped crystal, at low temperatures the linewidth will generally be much greater than the homogeneous linewidth. This is because of inhomogeneous broadening, which is a phenomenon caused by having an ensemble of dopant ions, where each individual ion has a slightly different environment in the host lattice [49]. Even though the homogeneous linewidth of a transition is the same for each atom, the effect of having a slightly different environment will mean that the transition *frequency* is slight different. As demonstrated in Figure 1.2 all the homogeneous lines with slightly different central frequencies will add together to make the linewidth in the crystal much larger [50]. The individual ions will form a distribution around the centre of the inhomogeneous line, when the number of atoms is large enough the inhomogeneous lineshape will be a convolution of this distribution with the Lorentzian homogeneous linewidth. When the width of the inhomogeneous distribution is much larger than the homogeneous linewidth, the inhomogeneous lineshape can be approximated just by the inhomogeneous distribution of ions.

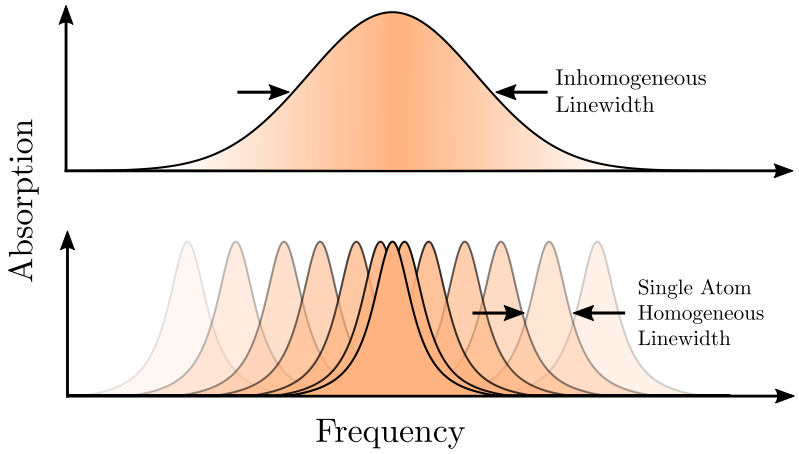

Figure 1.2: Diagram showing how the homogeneous linewidths from single atoms combine to give the inhomogeneous linewidth. The top plot shows a Gaussian distribution representing the inhomogeneous linewidth. The lower plot shows lots of single atom absorption peaks, with more homogeneous peaks closer to the centre of the inhomogeneous distribution. The single atom peaks add together to give the inhomogeneous line profile.

Inhomogeneous broadening will affect both the optical electronic transitions and the microwave spin transitions between Zeeman levels with the same electronic state.

1.3.3 Properties of Er^{3+}

Erbium is a member of the rare earths, and is of particular interest because it has an optical transition close to 1550 nm. It has atomic number 68, and there are several stable isotopes of erbium that occur in relatively high abundance (Table 1.1). For this work we will be considering a crystal of

Isotope	Neutrons	Abundance	Nuclear Spin
^{162}Er	94	0.139%	0
^{164}Er	96	1.601%	0
^{166}Er	98	33.503%	0
^{167}Er	99	22.869%	+7/2
^{168}Er	100	26.978%	0
^{170}Er	102	14.910%	0

Table 1.1: Atomic properties of the stable isotopes of erbium

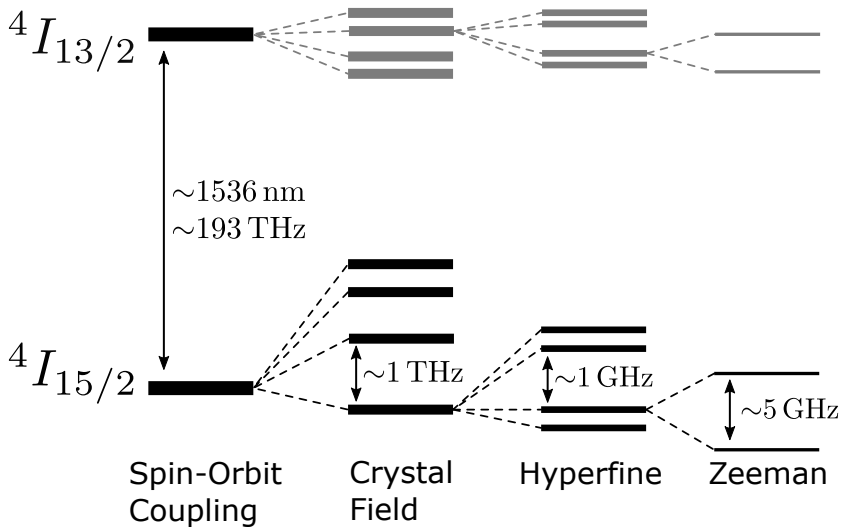

Figure 1.3: Different types of energy level splitting for a Er^{3+} ion doped in a crystal. Only ^{167}Er has hyperfine splitting because it is the only stable isotope of Erbium with non-zero nuclear spin. For the experiment described in this work, the size of the Zeeman splitting of ~ 5 GHz is for ^{170}Er with an applied magnetic field around 0.2 T.

yttrium orthosilicate (YSO), which is doped with ^{170}Er.

Energy Levels of Er^{3+} in YSO

In erbium, as with the rest of the rare earths, there are several factors which influence the splitting of the energy levels (Figure 1.3).

The 4f energy levels are not degenerate in the rare earths because of strong spin-orbit coupling and coulomb repulsion between the electrons. In erbium the 4f energy levels $^4I_{15/2}$ and $^4I_{13/2}$ are split almost entirely due to the spin–orbit coupling interaction, which leads to a transition at around 1536 nm. When the ions are embedded in a host lattice, the interactions with the crystal field will cause further splitting of the $^4I_{15/2}$ and $^4I_{13/2}$ levels, this splitting is on the order of 1 THz. Because of the size of this splitting, at cryogenic temperatures generally only the lowest crystal field level will be occupied.

^{167}Er is the only stable isotope with non-zero nuclear spin. This means the interaction between the nuclear spin and the electron spin causes hyperfine splitting of the crystal field levels. For this work we are focusing on using ^{170}Er which doesn't have any nuclear spin, and so there is no hyperfine splitting.

When a magnetic field is applied the energy levels will be split due to

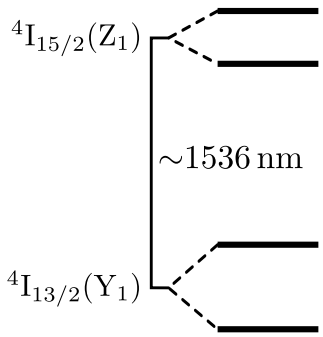

Figure 1.4: The upper and lower Zeeman levels for the $^4I_{15/2}$ and $^4I_{13/2}$ levels of erbium. Each of the Zeeman transitions is a microwave frequency transition, and transitions between $^4I_{15/2}$ and $^4I_{13/2}$ levels are optical transitions.

Zeeman splitting, which is described by this Hamiltonian,

$$\hat{H}_{\text{Zeeman}} = \mu_B \mathbf{B} \cdot \mathbf{g} \cdot \mathbf{S} \tag{1.3}$$

Where μ_B is the Bohr magneton, $\mathbf{B}$ is the applied magnetic field, $\mathbf{g}$ is the g-tensor for the energy level, and $\mathbf{S}$ is the electron spin operator. In erbium $\mathbf{g}$ is highly anisotropic, which means that the energy, and hence the Zeeman splitting, will change dramatically depending on how the magnetic field is aligned. For this work, we will consider Zeeman splitting of both the $^4I_{15/2}$ and the $^4I_{13/2}$ levels, these have different g-tensors, and so will have different splitting for the same applied magnetic field. We are considering the case where the applied magnetic field is aligned such that the Zeeman splitting of these levels will be around 5 GHz for magnetic field magnitude of around 0.2 T.

1.3.4 Erbium for Upconversion

For this work about using erbium ions for upconversion, we will only consider four atomic energy levels. These are the upper and lower Zeeman levels of $^4I_{15/2}(Z_1)$ and $^4I_{13/2}(Y_1)$ (Figure 1.4). $^4I_{15/2}(Z_1)$ and $^4I_{13/2}(Y_1)$ are the lowest crystal field levels of electronic states $^4I_{15/2}$ and $^4I_{13/2}$ respectively, and are separated by an optical transition around 1536 nm. When a magnetic field is applied these two levels will be Zeeman split. Both Zeeman pairs will be separated by microwave frequencies.

The original proposal for using an erbium doped crystal for upconversion which this work is based on is from [51], with similar proposals in [52, 53]. [51] considered a scheme using both Zeeman levels of the $^4I_{15/2}$ state and one of the levels from $^4I_{13/2}$. In this scheme, the lower Zeeman transition is driven with microwaves, which could have come from a superconducting qubit

system. The transition from the upper Zeeman level of $^4I_{15/2}$ to the $^4I_{13/2}$ level is driven with a coherent pump laser. This will produce an upconverted optical field.

In [51] the transitions are driven off resonance, which allows us to neglect any population in the excited states. The upconversion happens via an off-resonant Raman process. This allows the *adiabatic approximation* to be applied which assumes the dynamics of the atoms can be neglected. The microwave and optical fields will be enhanced by putting the erbium doped crystal in overlapping microwave and optical cavities. The optical cavity will have modes resonant with both the pump laser and the upconverted light.

Upconversion has been achieved in experiments using Er^{3+}:YSO [54, 46], but with conversion efficiencies far less than 100%. The aim of this work is to develop a more complete theoretical model for these experiments, which will allow us to better predict ways to improve conversion efficiency.

1.4 Thesis Outline

The overall goal of this thesis is to develop an accurate model of the double cavity upconversion system proposed in [51]. In Chapter 2, we will start by developing a model for the microwave and optical cavity fields interacting with an erbium doped crystal. In Chapter 3, we will develop a model for the erbium atoms interacting with the light fields, which will fit into the cavity field model from the previous chapter. Chapter 4 will focus on developing fast and accurate numerical methods for simulating this upconversion system. This chapter will have a large focus on dealing with the effects of inhomogeneous broadening, where all the atoms are in slightly different environments. In Chapter 5 the model we have developed in the previous chapters will be compared with experiments as a check that it works. In this chapter we will also discuss experimental parameters. In Chapter 6, we will develop a simplified model for very small microwave and optical output fields, which is the regime relevant to quantum information applications. In Chapter 7, we will investigate the system using the full model from Chapter 4, and then compare the full model with the adiabatic approximation model from [51] and the model developed in Chapter 6. Finally, in Chapter 8 we will look at finding realistic experimental parameters which will maximise the conversion efficiency.

1.4.1 Description of Original Work

This thesis includes both original work, and work from those who have come before me. As Sir Isaac Newton wrote to Robert Hooke,

If I have seen further it is by standing on the sholders of Giants

The work that is not original will be referenced in the text, but for clarity here is a description of which work is original.

In Chapter 2, starting using the description of the device from [51] and the formalism from [55, 56] I have developed equations for the cavity fields which take the form of coupled simultaneous equations. In Chapter 3, the model for a single atom has been modified from [46] to allow for variable complex fields. I have also adapted this model which used the spin transition of the ground electronic state to use the spin transition of the excited state. The numerical methods in Chapter 4 developed for dealing with the inhomogeneously broadened ensemble of atoms are original work. In Chapter 5, the experiments were performed by Gavin King, and the simulations are my work. The simplified model developed in Chapter 6 based on perturbations of the density matrix is original. For Chapter 7, all the work except for the adiabatic approximation from [51] is my own, as is the entirety of Chapter 8.

Chapter 2

Double Cavity Upconversion Device

This chapter will outline the proposed device for converting microwave photons into optical photons. The device is composed of overlapping microwave and optical cavities, with the cavity fields interacting with a crystal doped with Er^{+3} ions. We describe the upconversion mechanism due to the interaction between the atoms and cavity fields. From here we develop equations describing the steady state cavity fields, based on the input-output methods from [55].

This chapter is similar to the work in [51], except here we are including the effect of intrinsic loss from the cavities, and not making approximations about interactions between the fields and the atoms. This give us coupled nonlinear equations for the cavity fields.

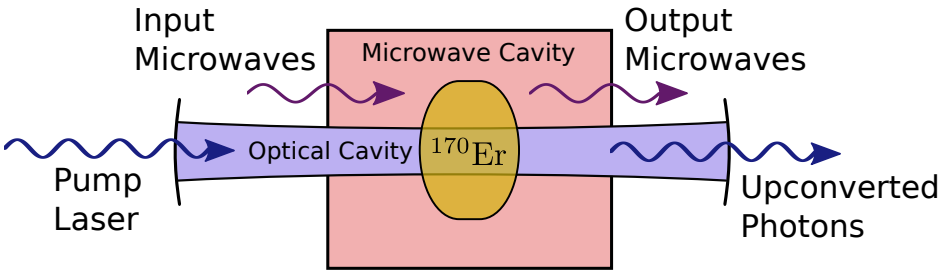

Figure 2.1: Diagram showing the system with two cavities and crystal doped with ^{170}Er. One of the modes of the optical cavity is driven by an optical pump laser, the microwave cavity is excited by input microwave photons. An input microwave photon and a pump laser photon are combined via an interaction with the ^{170}Er atoms to produce an optical upconverted photon.

2.1 Description of Upconversion Process

The system for upconversion that this work will focus on involves a crystal doped with ^{170}Er ions in two overlapping optical and microwave cavities driven by a coherent pump laser (Figure 2.1), this was suggested theoretically in [51] and has been demonstrated experimentally in [54]. The aim is to combine a microwave photon and a photon from the optical pump laser which will result in an optical photon at the frequency equal to the sum of the two input frequencies.

In this scheme, ^{170}Er ions are used as a three level Λ system; the lower two levels have an energy difference in the microwave range, and the upper level is separated by an optical transition. The two lower states will be two spin states of the electronic ground state $^4\mathrm{I}_{15/2}(\mathrm{Z}_1)$, which are Zeeman split with an external magnetic field. The third level is one of the Zeeman levels of the excited electronic state $^4\mathrm{I}_{13/2}(\mathrm{Y}_1)$. There are two Zeeman levels in the optical excited state, but we choose just one of these levels for our three level system (Figure 2.2).

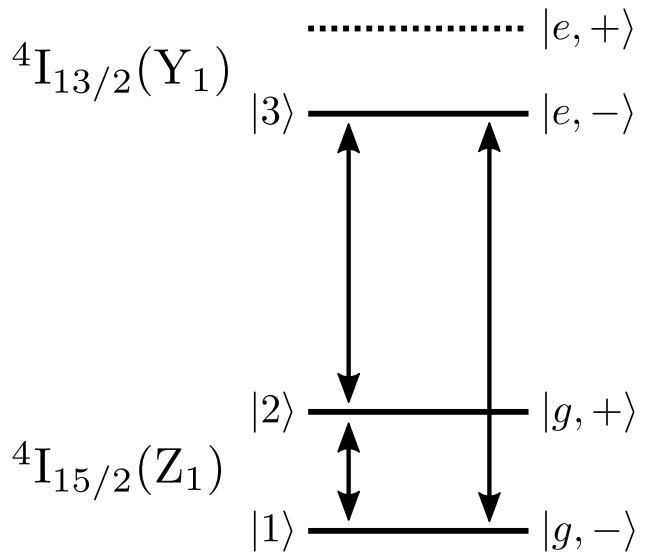

Figure 2.2: Diagram showing four atomic energy levels, the levels labelled $|g,-\rangle$ and $|g,+\rangle$ are the two Zeeman split levels of the electronic ground state, likewise $|e,-\rangle$ and $|e,+\rangle$ are the two Zeeman split levels of the electronic excited state. The three levels used for the lambda system are labelled $|1\rangle$, $|2\rangle$, $|3\rangle$. In this configuration the $|e,+\rangle$ level is not used.

For different configurations, different atomic energy levels will be used as different levels in the conversion process, for example the highest energy level in the lambda system may be the lower Zeeman level of the excited electronic state, or the upper Zeeman level. To avoid confusion, the atomic energy levels

will be referred to by their electronic and spin states, and the levels used for the conversion process will be labelled $|1\rangle$, $|2\rangle$, $|3\rangle$. The atomic energy levels will be labelled g and e for the ground and excited electronic states, and $-$ and $+$ for the lower and upper Zeeman levels.

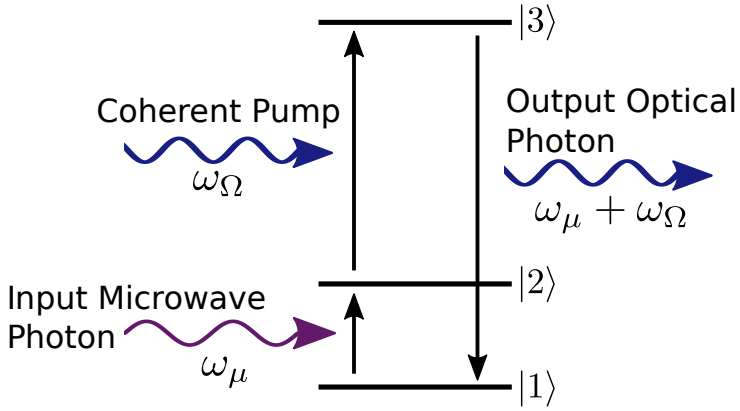

Figure 2.3: Energy level diagram for the lambda system, demonstrating the upconversion process. The input microwave photon and coherent pump both drive the atom into a higher energy level, and then the decay back to the ground state will emit an output optical photon with the frequency equal to the combined frequencies of the inputs.

In the conversion process as shown in Figure 2.3, a microwave photon in the microwave resonator will excite the spin transition of an Er ion to the second level, $|1\rangle \rightarrow |2\rangle$. The pump laser is resonant with the $|2\rangle \rightarrow |3\rangle$ transition, and will drive the atom into the upper excited state $|3\rangle$. The atom will then emit an optical photon and fall back to the ground state, $|3\rangle \rightarrow |1\rangle$. Because energy and momentum must be conserved, the frequency of the optical output photon will be equal to the sum of the two input frequencies,

$$\omega_o = \omega_\Omega + \omega_\mu \tag{2.1}$$

where ω_o is the frequency of the optical output, ω_Ω is the frequency of the optical pump laser, and ω_μ is the frequency of the input microwave photon.

There is an alternative scheme which uses the microwave Zeeman splitting of the excited electronic state rather than the ground state (Figure 2.4). In this scheme the atom is driven by the pump laser into the lower spin state of the electronic excited state, and then it is further excited into the upper spin state by an input microwave photon. As with the other scheme, the atom will then emit an optical photon and fall back into its ground state.

To begin with we will just consider the upconversion process which uses the ground state spin transition; this will later be easily translated to the process which uses the excited state transition.

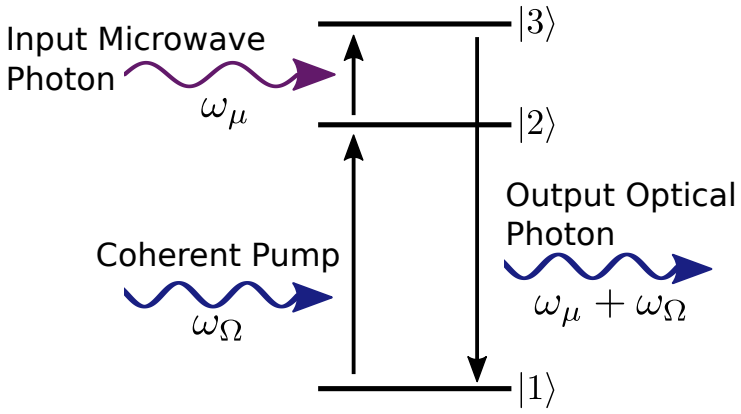

Figure 2.4: Energy level diagram of the upconversion process using the excited state spin transition, showing the input microwave photon, coherent pump and upconverted output photon.

2.2 System Hamiltonian

The Hamiltonian for the upconversion device, using the ground state spin transition, can be written as [51]

$$\hat{H}_{\text{sys}} = \hat{H}_{\text{fields}} + \hat{H}_{\text{atoms}} + \hat{H}_{\text{int}}, \tag{2.2}$$

where

$$\hat{H}_{\text{fields}} = \omega_{co}\hat{a}^\dagger\hat{a} + \omega_{c\mu}\hat{b}^\dagger\hat{b} \tag{2.3}$$

$$\hat{H}_{\text{atoms}} = \sum_k \omega_{13,k}\sigma_{33,k} + \omega_{12,k}\sigma_{22,k} \tag{2.4}$$

$$\hat{H}_{\text{int}} = \sum_k g_{o,k}\hat{a}\sigma_{31,k} + g_{\mu,k}\hat{b}\sigma_{21,k} + \Omega_k\sigma_{32,k} + \text{h.c.} \tag{2.5}$$

$\hat{H}_{\text{fields}}$ is the Hamiltonian which describes the energy of the light fields in the cavities, ω_{co} and $\omega_{c\mu}$ the frequencies of the optical and microwave cavities respectively. $\hat{a}$ and $\hat{b}$ are the annihilation operators for the optical and microwave fields respectively.

$\hat{H}_{\text{atoms}}$ describes the excitations of the atoms, and $\hat{H}_{\text{int}}$ describes the interactions between the atoms and the cavity fields. The sums refer to the sums over every individual atom, which will differ because the atoms will have slightly different transition frequencies due to inhomogeneous broadening. These different frequencies will influence the interaction between the atoms and the fields; for example, an atomic transition closer to the frequency of one of the light fields will interact more strongly. There will also be inhomogeneity

in the coupling constants $g_{o,k}$ and $g_{\mu,k}$, which will depend on the frequency of the light fields and the position of the atom in the cavity modes.

For the kth atom, $\omega_{13,k}$ and $\omega_{12,k}$ are the atomic transition frequencies for $|1\rangle \rightarrow |3\rangle$ and $|1\rangle \rightarrow |2\rangle$ respectively, and $\sigma_{33,k}$ and $\sigma_{22,k}$ describe the population of $|3\rangle$ and $|2\rangle$. $\sigma_{nm,k}$ for $n \neq m$ is the atomic transition operator for the transition $|m\rangle \rightarrow |n\rangle$, and $g_{o,k}$ and $g_{\mu,k}$ are the couplings between the optical and microwave transitions and the light fields. Ω_k is the Rabi frequency for the $|2\rangle \rightarrow |3\rangle$ transition driven by the pump laser and increases with pump power.

2.3 Finding Equations for the Cavity Fields

In this section we will use input-output formalism from [55] to find equations for the cavity fields in our device. We will begin with a quantum treatment, where the cavity fields are operators, and then make a semi-classical approximation where the classical fields are treated as complex numbers. This allows us to model the quantum interactions between the atoms and the cavity fields, while also giving convenient equations for the classical cavity fields.

The cavities are each treated as being two-sided, meaning each cavity can have input and output from two ports. For the microwave cavity this could mean there are two coaxial connectors, and for the optical cavity there could be two partially reflective mirrors. For each cavity, there will be input through one side, or in some cases through neither. The coupling to the input and output fields will depend on the coupling losses of each cavity, and each cavity will also have some amount of intrinsic loss. Intrinsic loss refers to any loss of energy from the cavity field that is not through one of the two ports.

2.3.1 Input-Output Equations

The general equation of motion for the intra cavity field of a lossy two-sided cavity with annihilation operator α is given by [57]

$$\frac{\mathrm{d}\hat{\alpha}}{\mathrm{d}t} = -i[\hat{\alpha}, \hat{H}_{\mathrm{sys}}] - \frac{2\gamma_c + \gamma_i}{2}\hat{\alpha} + \sqrt{\gamma_c}\hat{\alpha}_{in,1} + \sqrt{\gamma_c}\hat{\alpha}_{in,2} + \sqrt{\gamma_i}\hat{\alpha}_{in,i}$$

where $\hat{H}_{\mathrm{sys}}$ is the Hamiltonian for inside the cavity, γ_c is the coupling loss via the ports of the cavity, γ_i is the intrinsic loss, $\hat{\alpha}_{in,1}$ and $\hat{\alpha}_{in,2}$ represent the input fields into cavity through the two ports, and $\alpha_{in,i}$ represents input into the cavity not through the ports.

Commutators

To find how our optical and microwave cavity modes evolve we need to evaluate their respective commutators. The annihilation operators follow standard bosonic commutation relations,

$$[\hat{a}, \hat{a}^\dagger] = [\hat{b}, \hat{b}^\dagger] = 1 \tag{2.6}$$

$$[\hat{a}, \hat{a}] = [\hat{b}, \hat{b}] = 0. \tag{2.7}$$

So for $\hat{a}$ we have,

$$\begin{aligned}[\hat{a}, \hat{H}_{\text{sys}}] &= \left[\hat{a}, \omega_{co}\hat{a}^\dagger\hat{a} + \sum_k g^*_{o,k}\hat{a}^\dagger\sigma_{13,k}\right] \\ &= \omega_{co}\hat{a} + \sum_k g^*_{o,k}[\hat{a}, \hat{a}^\dagger]\sigma_{13,k} \\ &= \omega_{co}\hat{a} + \sum_k g^*_{o,k}\sigma_{13,k}.\end{aligned}$$

Equivalently for $\hat{b}$ we have

$$[\hat{b}, \hat{H}_{\text{sys}}] = \omega_{c\mu}\hat{b} + \sum_k g^*_{\mu,k}\sigma_{12,k}$$

So for our two cavity modes, the input-output equations are,

$$\frac{\mathrm{d}\hat{a}}{\mathrm{d}t} = -i(\omega_{co}\hat{a} + \sum_k g^*_{o,k}\sigma_{13,k}) - \frac{2\gamma_{oc} + \gamma_{oi}}{2}\hat{a} + \sqrt{\gamma_{oc}}\hat{a}_{in,1} + \sqrt{\gamma_{oc}}\hat{a}_{in,2} + \sqrt{\gamma_{oi}}\hat{a}_{in,i} \tag{2.8}$$

$$\frac{\mathrm{d}\hat{b}}{\mathrm{d}t} = -i(\omega_{c\mu}\hat{b} + \sum_k g^*_{\mu,k}\sigma_{12,k}) - \frac{2\gamma_{\mu c} + \gamma_{\mu i}}{2}\hat{b} + \sqrt{\gamma_{\mu c}}\hat{b}_{in,1} + \sqrt{\gamma_{\mu c}}\hat{b}_{in,2} + \sqrt{\gamma_{\mu i}}\hat{b}_{in,i} \tag{2.9}$$

where γ_{oc} and $\gamma_{\mu c}$ are the coupling losses for the optical and microwave cavities, γ_{oi} and $\gamma_{\mu i}$ are the intrinsic losses, $\hat{a}_{in,1}, \hat{a}_{in,2}$ and $\hat{b}_{in,1}, \hat{b}_{in,2}$ represent the input fields through the ports, and $\hat{a}_{in,i}$ and $\hat{b}_{in,i}$ represent any other inputs.

At this stage we make a semi-classical approximation, and rather than treating our cavity fields as operators they simply become complex numbers. Additionally, this means our atomic transition operators, and the input fields will also be treated as complex numbers. For our microwave and optical cavities we are only going to have input through one of the ports, and so we neglect any input from port 2 of each cavity as well as any other inputs,

$a_{in,2} = b_{in,2} = a_{in,i} = b_{in,i} = 0$. With this, our input output equations for the classical fields are

$$\frac{\mathrm{d}a}{\mathrm{d}t} = -i(\omega_{co}a + \sum_k g^*_{o,k}\sigma_{13,k}) - \frac{2\gamma_{oc} + \gamma_{oi}}{2}a + \sqrt{\gamma_{oc}}a_{in} \tag{2.10}$$

$$\frac{\mathrm{d}b}{\mathrm{d}t} = -i(\omega_{c\mu}b + \sum_k g^*_{\mu,k}\sigma_{12,k}) - \frac{2\gamma_{\mu c} + \gamma_{\mu i}}{2}b + \sqrt{\gamma_{\mu c}}b_{in} \tag{2.11}$$

Boundary Conditions

Equations 2.10 and 2.11 describe the fields *inside* the cavities, but practically we care about the outputs from the cavity. A boundary condition relates the intra cavity field to the input and output fields,

$$a = \frac{1}{\sqrt{\gamma_{oc}}}(a_{in} + a_{out}),\ b = \frac{1}{\sqrt{\gamma_{\mu c}}}(b_{in} + b_{out}) \tag{2.12}$$

and because we are assuming there is no input to the cavity from one side,

$$a_{out} = \sqrt{\gamma_{oc}}a,\ b_{out} = \sqrt{\gamma_{\mu c}}b \tag{2.13}$$

Frequency Domain

So far we have been dealing with our cavity fields in the time domain, where $a = a(t)$ and $b = b(t)$, however by solving our input-output equations in the frequency domain we can see how the system behaves with different input frequencies.

The classical fields can be found in terms of their frequency components using the Fourier transform relations,

$$\tilde{a}(\omega_o) = \frac{1}{\sqrt{2\pi}}\int_{-\infty}^{\infty} e^{i\omega_o t}a(t)\mathrm{d}t \tag{2.14}$$

$$\tilde{b}(\omega_\mu) = \frac{1}{\sqrt{2\pi}}\int_{-\infty}^{\infty} e^{i\omega_\mu t}b(t)\mathrm{d}t \tag{2.15}$$

where ω_o and ω_μ are the optical and microwave input frequencies. Taking the Fourier transform of our input-output equations we have

$$-i\omega_o\tilde{a} = -i(\omega_{co}\tilde{a} + \sum_k g^*_{o,k}\sigma_{13,k}) - \frac{2\gamma_{oc} + \gamma_{oi}}{2}\tilde{a} + \sqrt{\gamma_{oc}}\tilde{a}_{in} \tag{2.16}$$

$$-i\omega_\mu\tilde{b} = -i(\omega_{c\mu}\tilde{b} + \sum_k g^*_{\mu,k}\sigma_{12,k}) - \frac{2\gamma_{\mu c} + \gamma_{\mu i}}{2}\tilde{b} + \sqrt{\gamma_{\mu c}}\tilde{b}_{in} \tag{2.17}$$

2.3.2 Cavity Field Equations

We can now formulate equations for the microwave and optical cavity fields in terms of the input frequencies, which is the primary goal of this chapter. Defining the detunings between the input fields and the cavities,

$$\delta_o = \omega_o - \omega_{co} \tag{2.18}$$

$$\delta_\mu = \omega_\mu - \omega_{c\mu} \tag{2.19}$$

we can rearrange Equations 2.14 and 2.15 to form expressions for the cavity fields $\tilde{a}$ and $\tilde{b}$ in terms of these detunings,

$$\tilde{a}(\delta_o) = \frac{-i\sum_k g^*_{o,k}\sigma_{13,k} + \sqrt{\gamma_{oc}}\tilde{a}_{in}}{(2\gamma_{oc} + \gamma_{oi})/2 - i\delta_o} \tag{2.20}$$

$$\tilde{b}(\delta_\mu) = \frac{-i\sum_k g^*_{\mu,k}\sigma_{12,k} + \sqrt{\gamma_{\mu c}}\tilde{b}_{in}}{(2\gamma_{\mu c} + \gamma_{\mu i})/2 - i\delta_\mu} \tag{2.21}$$

These equations are coupled via the atomic terms, which are functions of the cavity field amplitudes and frequencies, $\sigma_{13,k} = \sigma_{13,k}(a, b, \delta_o, \delta_\mu)$, $\sigma_{12,k} = \sigma_{12,k}(a, b, \delta_o, \delta_\mu)$. If there is no input into the optical cavity, $\tilde{a}_{in} = 0$, then there can still be a non-zero optical cavity field because of the atomic terms, $\sum_k g^*_{o,k}\sigma_{13,k}$. This intra cavity field will result in an optical output field which is our upconverted signal.

2.3.3 Process Using the Excited State Spin Transition

Thus far we have been considering the upconversion scheme which uses the ground state microwave transition. These results can be translated to the scheme which uses the microwave transition of the excited electronic state. In this system the optical pump will drive the $|1\rangle \rightarrow |2\rangle$ transition, and the microwaves will drive the $|2\rangle \rightarrow |3\rangle$ transition. In Equations 2.20 and 2.21 we just have to change the σ_{12} operators to σ_{23}. The transition which emits the optical output photons is still the $|3\rangle \rightarrow |1\rangle$ transition, so the σ_{13} operators aren't changed.

$$\tilde{a}(\delta_o) = \frac{-i\sum_k g^*_{o,k}\sigma_{13,k} + \sqrt{\gamma_{oc}}\tilde{a}_{in}}{(2\gamma_{oc} + \gamma_{oi})/2 - i\delta_o} \tag{2.22}$$

$$\tilde{b}(\delta_\mu) = \frac{-i\sum_k g^*_{\mu,k}\sigma_{23,k} + \sqrt{\gamma_{\mu c}}\tilde{b}_{in}}{(2\gamma_{\mu c} + \gamma_{\mu i})/2 - i\delta_\mu} \tag{2.23}$$

2.3.4 Empty Cavity Limit

If there is no atom–field interaction then the transmission through the cavities will be standard Lorentzians, regardless of the atomic scheme. Using the boundary conditions (Equation 2.13) the empty cavity transmission, as expected, is

$$\left|\frac{a_{out}}{a_{in}}\right|^2 = \frac{\gamma_{oc}^2}{(2\gamma_{oc}+\gamma_{oi})^2/4+\delta_o^2} \tag{2.24}$$

$$\left|\frac{b_{out}}{b_{in}}\right|^2 = \frac{\gamma_{\mu c}^2}{(2\gamma_{\mu c}+\gamma_{\mu i})^2/4+\delta_\mu^2} \tag{2.25}$$

When the atoms are far detuned from the fields their interaction will be small, and the cavity transmission will approach these empty cavity results.

We now have developed equations for the cavity fields for our upconversion device. This thesis will focus on solving these equations to model the device, and using them make the upconversion process more efficient. The upconversion process happens via interactions with the erbium ions in the crystal, these interactions appear in our cavity field equations via the atomic transition operator terms. We haven't yet developed a description for these interactions, and so the next chapter will focus on developing a model of our ensemble of atoms interacting with the light fields.

Chapter 3

Atoms and Driving Fields

The core of the upconversion process involves the interaction between atoms and various driving fields. In this chapter we aim to develop an accurate model to describe the state of the atoms in our system so that we can later model the upconversion process. We first develop a model for a single atom, which will include the effects of the light fields, as well as temperature and loss effects. This single atom model can then be used to develop a description for an ensemble of atoms, which will be used to describe the atom–field interaction in our input–output equations from Chapter 2.

3.1 Single Atom with Driving Fields

Initially we will consider a single atom used as a three level Λ system, where the lower levels are separated by a microwave transition, and the upper level is separated by an optical transition (Figure 3.1).

The microwave transition between the ground state $|1\rangle$ and the second level $|2\rangle$ has frequency ω_{12}, and the upper level $|3\rangle$ is separated from $|1\rangle$ and $|2\rangle$ by optical transitions with frequencies ω_{13} and ω_{23} respectively. All three transitions will be driven by light fields.

A microwave field will drive the $|1\rangle \rightarrow |2\rangle$ transition and an optical field from the upconverted photons will interact with the $|1\rangle \rightarrow |3\rangle$ transition. The microwave field is the input microwave field for the upconversion process, and the optical field is the upconverted output field. In this chapter these microwave and optical fields will be treated as classical fields. The microwave field has complex amplitude b and frequency ω_μ, likewise the optical field has complex amplitude a and frequency ω_o. The frequencies of these input fields may be detuned from the atomic transition frequencies.

Additionally, there will be a coherent field driving the $|2\rangle \rightarrow |3\rangle$, the Rabi

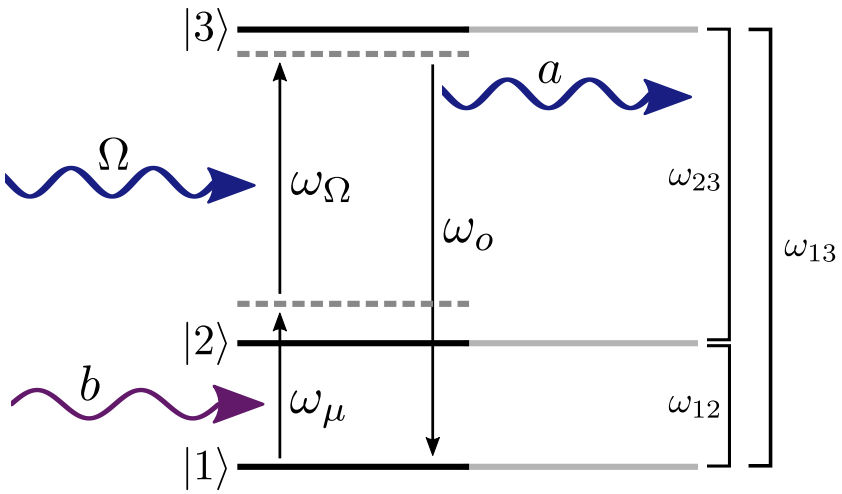

Figure 3.1: Energy level diagram for the scheme using the ground state microwave transition, showing frequencies of the atomic transitions and the light fields. The fields may be detuned from the atomic transitions. The microwave field is represented by b, the upconverted optical field is represented by a, and the Rabi frequency for the pump field is Ω.

frequency for this transition is Ω. For the upconversion process, a microwave photon and an optical pump photon will excite the atom into $|3\rangle$, where it will decay to the ground state and emit an optical photon with frequency

$$\omega_o = \omega_\mu + \omega_\Omega$$

3.2 Density Matrix

The atoms can be modelled using their density matrices, and this will also allow us to find values for their atomic transition operators.

The density matrix ρ is a matrix which describes the state of a quantum system. It allows us to represent mixed states, where there is statistical uncertainty about what state the system is in as well as quantum uncertainty. The general form of the density matrix is

$$\rho = \sum_j p_j \left|\psi_j\right\rangle \left\langle\psi_j\right| \tag{3.1}$$

This represents a system where there is p_j probability that the system is in state $|\psi_j\rangle$. The density matrix is often used in quantum optics because it allows us to rigorously deal with thermal and quantum noise effects [58].

The density matrix describing our three level atom is a 3×3 matrix. The diagonal elements are the population fraction in the corresponding state, for

example if $\rho_{11} = 0.5$ then there is a 50% chance that the atoms would be measured to be in the ground state. A measurement of the state of the atom will result in the atom being in either $|1\rangle$, $|2\rangle$ or $|3\rangle$ and so the diagonal terms are subject to the normalisation condition $\sum \rho_{nn} = \rho_{11} + \rho_{22} + \rho_{33} = 1$.

The off-diagonal elements of ρ correspond to the coherence between the two states, which we will now show are also the expectation values for the atomic transition operators. The atomic transition operator σ_{nm} takes the atom from state $|m\rangle$ to $|n\rangle$, and so can be written as an outer product of these states,

$$\sigma_{nm} = |n\rangle \langle m|$$

The n, m matrix element of ρ is,

$$\rho_{nm} = \langle m| \rho |n\rangle = \sum_j p_j \langle m|\psi_j\rangle \langle \psi_j|n\rangle$$

These inner products are simply complex numbers and so can be rearranged to give,

$$\rho_{nm} = \sum_j p_j \langle \psi_j|n\rangle \langle m|\psi_j\rangle = \sum_j p_j \langle \sigma_{nm}\rangle_j$$

$\langle \sigma_{nm}\rangle_j$ is the quantum expectation value of σ_{nm} for an atom in state $|\psi_j\rangle$. And so the sum over $\langle \sigma_{nm}\rangle_j$ with their corresponding statistical probability will yield the quantum and statistical expectation value of σ_{nm}. This allows us to use ρ to model the atoms in the upconversion process. Specifically, we will use the elements ρ_{12} and ρ_{13} as the values for the atomic transition operators σ_{12} and σ_{13} in the equations for the cavity fields, Equations 2.20 and 2.21.

3.3 Liouville Equation

We are wanting to be able to find the atomic density matrix, which will give us the expectation values of the atomic transition operators. In this section we will use the Master Equation to find the steady state atomic density matrix.

The dynamics of the density matrix are governed by the Master Equation,

$$\frac{\mathrm{d}\rho}{\mathrm{d}t} = \mathcal{L}\rho \tag{3.2}$$

where $\mathcal{L}$ is the Liouvillian superoperator acting on ρ, this means $\mathcal{L}$ is a linear operator that acts on ρ and returns another 3×3 matrix. We will solve for ρ in the steady state using,

$$\frac{\mathrm{d}\rho}{\mathrm{d}t} = \mathcal{L}\rho_{ss} = 0. \tag{3.3}$$

$\mathcal{L}$ takes into account for both the Hamiltonian dynamics of the system, as well as non-Hamiltonian processes due to thermal, damping, and dephasing effects.

3.3.1 Hamiltonian Dynamics

$\mathcal{L}$ can be split into the Hamiltonian dynamics, and the other processes,

$$\mathcal{L}\rho = -\frac{i}{\hbar}[\hat{H}, \rho] + \Gamma\rho \tag{3.4}$$

where $\hat{H}$ is the atomic Hamiltonian, and Γ is a superoperator describing the non-Hamiltonian processes. The Hamiltonian for the atom interacting with the optical and microwave fields is [51]

$$\hat{H} = \omega_o \hat{a}^\dagger \hat{a} + \omega_\mu \hat{b}^\dagger \hat{b} + \omega_{13}\sigma_{33} + \omega_{12}\sigma_{22} \tag{3.5a}$$

$$+ g_o \hat{a}\sigma_{31} + g_\mu \hat{b}\sigma_{21} + \Omega\sigma_{32} + h.c. \tag{3.5b}$$

Here $\omega_o \hat{a}^\dagger \hat{a}$ and $\omega_\mu \hat{b}^\dagger \hat{b}$ represent the energy in the optical and microwave cavities, $\omega_{12}\sigma_{22}$ and $\omega_{13}\sigma_{33}$ represent the energy of the atom being in the excited states $|2\rangle$ and $|3\rangle$. The second line represents the coupling between the three atomic transitions, and the three fields; the optical output field, the microwave field, and the pump laser field.

We are wanting to find the steady state density matrix, and so for this we need everything to be constant in time. As it stands, the microwave and optical fields are oscillating at GHz and THz frequencies and so are definitely not constant in time. However, moving into the frame rotating with these fields will remove the time dependence of these terms and allow us to find the steady state density matrix.

To do this we split the Hamiltonian into two commuting parts,

$$\hat{H} = \hat{H}_0 + \hat{V}, \tag{3.6}$$

where,

$$\hat{H}_0 = \omega_o \hat{a}^\dagger \hat{a} + \omega_\mu \hat{b}^\dagger \hat{b} + \omega_o \sigma_{33} + \omega_\mu \sigma_{22} \tag{3.7}$$

$$\hat{V} = (\omega_{13} - \omega_o)\sigma_{33} + (\omega_{12} - \omega_\mu)\sigma_{22} + g_o \hat{a}\sigma_{31} + g_\mu \hat{b}\sigma_{21} + \Omega\sigma_{32} + h.c. \tag{3.8}$$

where $\hat{H}_0$ has the terms rotating with the fields. Because these two parts commute we can use $\hat{V}$ as our interaction picture Hamiltonian which is rotating in the frame defined by $\hat{H}_0$.

From here we treat the optical and microwaves as classical fields,

$$\hat{a} \to a,\ \hat{a}^\dagger \to \overline{a} \tag{3.9}$$

$$\hat{b} \to b,\ \hat{b}^\dagger \to \overline{b} \tag{3.10}$$

Here a and b represent the classical field amplitudes, and $\bar{a}$ and $\bar{b}$ are their complex conjugates. We now express $\hat{V}$ in matrix form, in the basis of the three level system. The basis we are working in is

$$|1\rangle = \begin{bmatrix}1\\0\\0\end{bmatrix}, \quad |2\rangle = \begin{bmatrix}0\\1\\0\end{bmatrix}, \quad |3\rangle = \begin{bmatrix}0\\0\\1\end{bmatrix} \tag{3.11}$$

And so V is written as

$$V = \begin{bmatrix} 0 & \overline{g_\mu b} & \overline{g_o a} \\ g_\mu b & \omega_{12} - \omega_\mu & \overline{\Omega} \\ g_o a & \Omega & \omega_{13} - \omega_o \end{bmatrix} \tag{3.12}$$

This Hamiltonian will be used in the Liouvillian superoperator. This is currently in terms of input light and atomic transition frequencies, V can also be expressed in terms of detunings

$$V = \begin{bmatrix} 0 & \overline{g_\mu b} & \overline{g_o a} \\ g_\mu b & \delta_{a\mu} - \delta_\mu & \overline{\Omega} \\ g_o a & \Omega & \delta_{ao} - \delta_o \end{bmatrix} \tag{3.13}$$

where $\delta_{a\mu}$ and δ_{ao} are the detunings between the microwave transition and cavity, and the optical transition and cavity for the single atom,

$$\delta_{a\mu} = \omega_{12} - \omega_{c\mu} \tag{3.14}$$

$$\delta_{ao} = \omega_{13} - \omega_{co} \tag{3.15}$$

3.3.2 Damping Effects

As well as the Hamiltonian dynamics of the three level atom there will also be loss effects in the system. These loss effects will be both population damping effects and dephasing effects.

The loss effects are modelled by considering our system, a three level atom, coupled to a reservoir that represents the environment [56, 58]. The total system Hamiltonian can be written as,

$$\hat{H}_{\text{total}} = \hat{H}_{\text{atom}} + \hat{H}_{\text{res}} + \hat{H}_{\text{int}} \tag{3.16}$$

Where $\hat{H}_{\text{atom}}$, $\hat{H}_{\text{res}}$ and $\hat{H}_{\text{int}}$ are the Hamiltonians describing the atom, reservoir, and the interaction between the atom and reservoir respectively. The reservoir in some sense describes the entire universe except for the atom, and so it would be very convenient to be able to describe the atomic dynamics without having to worry about the rest of the entire universe. We will call w the density matrix describing the state of the total system (the entire universe). This can be reduced to the density matrix describing just the atom ρ by 'tracing out' the effect of the reservoir,

$$\rho = \text{Tr}_{res}\{w\} \tag{3.17}$$

where Tr_{res} denotes a partial trace over the reservoir variables.

For describing the time dynamics of our system (finding ρ as a function of time) we make two main assumptions. The first is assume that the system and the reservoir are always uncorrelated and that the state of the reservoir doesn't change with time. This is called the Born approximation, and can be applied when the system is small and the coupling is weak, so will have negligible effect on the reservoir. The second assumption is called the Markov approximation and makes the assumption that the interactions between the system and reservoir are only correlated for very small time scales, this can be thought of as the interactions being memoryless.

Treating the reservoir as a thermal bath of harmonic oscillators, we can find the equation of motion for ρ which includes Hamiltonian evolution, as well as the damping effects which arise from interactions with the reservoir. These interactions will result in population damping, which leads to the decay of population from one state to another. For the states $|n\rangle$ and $|m\rangle$ where $n < m$, the population damping is described by,

$$\begin{aligned}\Gamma_{nm}\rho = &\frac{\gamma_{nm}}{2}(N_{bath,nm}+1)(2\sigma_{nm}\rho\sigma_{mn} - \sigma_{mn}\sigma_{nm}\rho - \rho\sigma_{mn}\sigma_{nm}) \\ &+ \frac{\gamma_{nm}}{2}N_{bath,nm}(2\sigma_{mn}\rho\sigma_{nm} - \sigma_{nm}\sigma_{mn}\rho - \rho\sigma_{nm}\sigma_{mn})\end{aligned} \tag{3.18}$$

where γ_{nm} is the damping rate. The effect of temperature is included by treating the reservoir as a thermal bath at finite temperature, where the number of photons in the thermal bath for the transition is given by the Planck distribution [55]

$$N_{bath,nm} = \frac{1}{\exp(\hbar\omega_{nm}/k_B T) - 1} \tag{3.19}$$

For the optical transitions $|1\rangle \rightarrow |3\rangle$, $|2\rangle \rightarrow |3\rangle$ the transition frequencies are so high that even at noncryogenic temperatures the number of thermal

photons is negligible, and so we can say

$$N_{bath,13} \approx N_{bath,23} \approx 0 \tag{3.20}$$

For the microwave transition $N_{bath,12}$ is not negligible and will affect the damping. Because this is the only transition there the temperature effects the damping, we will refer to $N_{bath,12}$ as N_{bath}.

So our population terms are given by

$$\Gamma_{13}\rho = \frac{\gamma_{13}}{2}(2\sigma_{13}\rho\sigma_{31} - \sigma_{31}\sigma_{13}\rho - \rho\sigma_{31}\sigma_{13}) \tag{3.21}$$

$$\Gamma_{23}\rho = \frac{\gamma_{23}}{2}(2\sigma_{23}\rho\sigma_{32} - \sigma_{32}\sigma_{23}\rho - \rho\sigma_{32}\sigma_{23}) \tag{3.22}$$

$$\begin{aligned}\Gamma_{12}\rho = &\frac{\gamma_{12}}{2}(N_{bath}+1)(2\sigma_{12}\rho\sigma_{21} - \sigma_{21}\sigma_{12}\rho - \rho\sigma_{21}\sigma_{12}) \\ &+ \frac{\gamma_{12}}{2}N_{bath}(2\sigma_{21}\rho\sigma_{12} - \sigma_{12}\sigma_{21}\rho - \rho\sigma_{12}\sigma_{21})\end{aligned} \tag{3.23}$$

There will be additional dephasing effects are due to interactions between the ions and the host lattice, which typically have the effect of enhancing decay of the atomic coherences.For the two excited levels these are given by

$$\Gamma_{2d}\rho = \frac{\gamma_{2d}}{2}(2\sigma_{22}\rho\sigma_{22} - \sigma_{22}\rho - \rho\sigma_{22}) \tag{3.24}$$

$$\Gamma_{3d}\rho = \frac{\gamma_{3d}}{2}(2\sigma_{33}\rho\sigma_{33} - \sigma_{33}\rho - \rho\sigma_{33}) \tag{3.25}$$

The damping and dephasing effects can be combined into one superoperator acting on ρ

$$\Gamma\rho = \Gamma_{12}\rho + \Gamma_{23}\rho + \Gamma_{13}\rho + \Gamma_{2d}\rho + \Gamma_{3d}\rho \tag{3.26}$$

This superoperator Γ governs all the damping and dephasing dynamics of ρ.

3.4 Solving for Steady-State

We now are in a position to solve for the steady state density matrix,

$$\mathcal{L}\rho_{ss} = -i[\hat{V}, \rho_{ss}] + \Gamma\rho_{ss} = 0 \tag{3.27}$$

To solve this we will use a method modified from [46], using variable fields a and b rather than their Rabi frequencies. Because $\mathcal{L}$ acting on ρ is a linear operation we can solve Equation 3.27 by expressing ρ as 9×1 vector rather than a 3×3 matrix, and writing $\mathcal{L}$ as a 9×9 matrix. From here ρ_{ss} can be found by solving $\mathcal{L}\rho_{ss} = 0$ while accounting for normalisation. Using this method ρ is written as

$$\rho \doteq [\rho_{11},\ \rho_{21},\ \rho_{31},\ \rho_{12},\ \rho_{22},\ \rho_{32},\ \rho_{13},\ \rho_{23},\ \rho_{33}]^T \tag{3.28}$$

$\mathcal{L}$ in Equation 3.27 is composed of operators acting on ρ from both the left and right, for example $[\hat{V}, \rho] = \hat{V}\rho - \rho\hat{V}$. To deal with this we use a similar approach as the python package QuTip [59].

We can define 9×9 operators acting from the left on the 9×1 vector ρ, which have the equivalent effect as 3×3 operators acting on the matrix ρ from the left or the right. For a given 3×3 operator $\hat{m}$, these 9 operators are defined by

$$\mathbf{M}_{\rightarrow} = \mathbb{1} \otimes \hat{m} \tag{3.29}$$
$$\mathbf{M}_{\leftarrow} = \hat{m} \otimes \mathbb{1} \tag{3.30}$$

where $\otimes$ is the tensor product. These have the following equivalent effects,

$$\begin{aligned} \mathbf{M}_{\rightarrow}\rho &\quad \text{is equivalent to} \quad \hat{m}\rho \\ \mathbf{M}_{\leftarrow}\rho &\quad \text{is equivalent to} \quad \rho\hat{m} \end{aligned}$$

This allows us to define 9×9 operators for all the operators that make up our Liouvillian. These are then combined to express the Liouvillian superoperator as a 9×9 matrix,

$$\mathcal{L} \doteq$$

$$\begin{bmatrix}
-\gamma_{12}n_b & -ig_\mu\overline{b} & -ig_o\overline{a} & ibg_\mu & \gamma_{12}(n_b{+}1) & 0 & iag_o & 0 & \gamma_{13} \\
-ibg_\mu & \begin{matrix}-\frac{\gamma_{12}(2n_b+1)}{2}\\ -\frac{\gamma_{2d}}{2}\\ -i(\delta_{a\mu}-\delta_\mu)\end{matrix} & -i\Omega & 0 & ibg_\mu & 0 & 0 & iag_o & 0 \\
-iag_o & -i\Omega & \begin{matrix}-\frac{\gamma_{12}n_b+\gamma_{13}}{2}\\ -\frac{\gamma_{23}+\gamma_{3d}}{2}\\ -i(\delta_{ao}-\delta_o)\end{matrix} & 0 & 0 & ibg_\mu & 0 & 0 & iag_o \\
ig_\mu\overline{b} & 0 & 0 & \begin{matrix}-\frac{\gamma_{12}(2n_b+1)}{2}\\ -\frac{\gamma_{2d}}{2}\\ +i(\delta_{a\mu}-\delta_\mu)\end{matrix} & -ig_\mu\overline{b} & -ig_o\overline{a} & i\Omega & 0 & 0 \\
\gamma_{12}n_b & ig_\mu\overline{b} & 0 & -ibg_\mu & -\gamma_{12}(n_b{+}1) & -i\Omega & 0 & i\Omega & \gamma_{23} \\
0 & 0 & ig_\mu\overline{b} & -iag_o & -i\Omega & \begin{matrix}-\frac{\gamma_{12}(n_b+1)}{2}\\ -\frac{\gamma_{13}+\gamma_{23}}{2}\\ -\frac{\gamma_{2d}+\gamma_{3d}}{2}\\ +i(\delta_{a\mu}-\delta_\mu)\\ -i(\delta_{ao}-\delta_o)\end{matrix} & 0 & 0 & i\Omega \\
ig_o\overline{a} & 0 & 0 & i\Omega & 0 & 0 & \begin{matrix}-\frac{\gamma_{12}}{2}n_b\\ -\frac{\gamma_{13}+\gamma_{23}}{2}\\ -\frac{\gamma_{3d}}{2}\\ +i(\delta_{ao}-\delta_o)\end{matrix} & -ig_\mu\overline{b} & -ig_o\overline{a} \\
0 & ig_o\overline{a} & 0 & 0 & i\Omega & 0 & -ibg_\mu & \begin{matrix}-\frac{\gamma_{12}(n_b+1)}{2}\\ -\frac{\gamma_{13}+\gamma_{23}}{2}\\ -\frac{\gamma_{2d}+\gamma_{3d}}{2}\\ -i(\delta_{a\mu}-\delta_\mu)\\ +i(\delta_{ao}-\delta_o)\end{matrix} & -i\Omega \\
0 & 0 & ig_o\overline{a} & 0 & 0 & i\Omega & -iag_o & -i\Omega & -\gamma_{13}-\gamma_{23}
\end{bmatrix} \tag{3.31}$$

Practically this matrix was generated using SymPy, the Python library for symbolic mathematics [60]. The atomic Hamiltonian V, and the atomic transition operators were expressed symbolically as 3×3 matrices. For each of these operators we generated 9×9 symbolic matrices which were equivalent to Equations 3.29 and 3.30. These were then combined to make Equation 3.31.

We want to solve for the steady state density matrix ρ_{ss} by finding the kernel of $\mathcal{L}$, however this is not uniquely determined without an additional constraint. Including our normalisation condition on ρ allows us to find the unique solution. We need to insure $\rho_{11} + \rho_{22} + \rho_{33} = 1$, so we replace the first row of $\mathcal{L}$ with

$$[1, 0, 0, 0, 1, 0, 0, 0, 1]$$

and instead of solving for $\mathcal{L}\rho = 0$, we solve for

$$\mathcal{L}\rho = 0_{\mathbb{1}} \tag{3.32}$$

where

$$0_{\mathbb{1}} = [1, 0, 0,\ 0, 0, 0,\ 0, 0, 0]^T \tag{3.33}$$

Replacing this first row doesn't change anything about the dynamics. Previously, the first row of $\mathcal{L}$ described the dynamics of ρ_{11}, but with fifth and ninth row, which describe the dynamics of ρ_{22} and ρ_{33}, the dynamics of ρ_{11} are already determined from normalisation. The normalisation condition means we will get a unique and normalised solution for ρ.

3.5 Atomic Scheme Using the Excited State Microwave Transition

The model for the atomic system that we have developed can be modified for the system using the excited state microwave transition, which is a three level V system. In this system the $|1\rangle \rightarrow |2\rangle$ transition is an optical transition and is driven by the pump laser, and the $|2\rangle \rightarrow |3\rangle$ transition is a microwave transition driven by the microwave field (Figure 3.2). For this system the

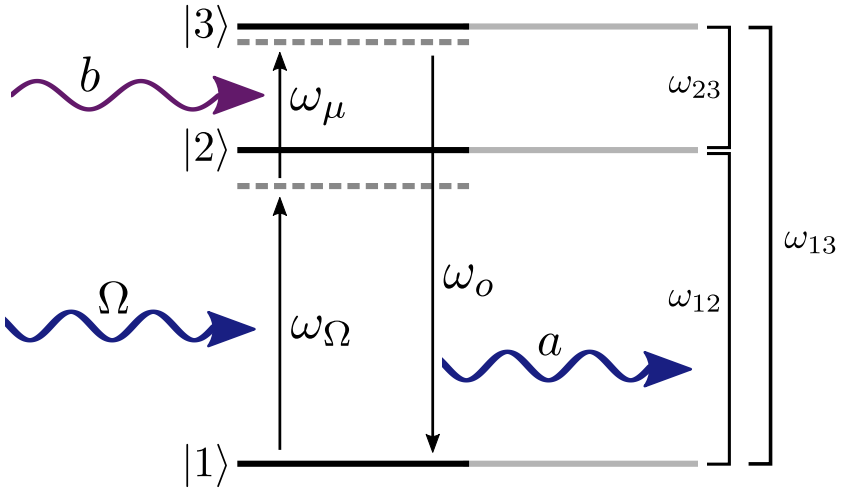

Figure 3.2: Energy level diagram for the system using the excited state microwave transition, showing frequencies of the atomic transitions and the light fields. The fields may be detuned from the atomic transitions. The microwave field is represented by b, the upconverted optical field is represented by a, and the Rabi frequency for the pump field is Ω.

equivalent atomic Hamiltonian to Equation 3.13 is

$$V = \begin{bmatrix} 0 & \overline{\Omega} & \overline{g_o a} \\ \Omega & \delta_{a\mu} - \delta_\mu & \overline{g_\mu b} \\ g_o a & g_\mu b & \delta_{ao} - \delta_o \end{bmatrix} \tag{3.34}$$

This atomic scheme is still subject to the damping and dephasing effects just like when using the ground state microwave transition. The only difference in the equations governing these effects is the effect of the thermal bath on the damping rates. When using the microwave transition of the excited state, the $|1\rangle \rightarrow |2\rangle$ transition is an optical transition, and so we can neglect the effect of the thermal bath on the population damping. The $|2\rangle \rightarrow |3\rangle$ transition is now a microwave transition and so there will be significant thermal effects on the damping, as there were for the microwave transition when using the ground state microwave transition. When using the scheme with the excited state microwave transition the damping terms are,

$$\Gamma_{12}\rho = \frac{\gamma_{12}}{2}(2\sigma_{12}\rho\sigma_{21} - \sigma_{21}\sigma_{12}\rho - \rho\sigma_{21}\sigma_{12}) \tag{3.35}$$

$$\begin{aligned}\Gamma_{23}\rho = &\frac{\gamma_{23}}{2}(N_{bath}+1)(2\sigma_{23}\rho\sigma_{32} - \sigma_{32}\sigma_{23}\rho - \rho\sigma_{32}\sigma_{23}) \\ &+ \frac{\gamma_{23}}{2}N_{bath}(2\sigma_{32}\rho\sigma_{23} - \sigma_{23}\sigma_{32}\rho - \rho\sigma_{23}\sigma_{32})\end{aligned} \tag{3.36}$$

The different atomic Hamiltonian and damping terms will mean that the Liouvillian is different when using the excited state microwave transition, which will lead to different atomic dynamics. The Liouvillian for this atomic scheme is,

$$\mathcal{L} \doteq$$

$$\begin{bmatrix}
0 & -i\Omega & -ig_o\overline{a} & i\Omega & \gamma_{12} & 0 & iag_o & 0 & \gamma_{13} \\
-i\Omega & \begin{matrix}-\frac{\gamma_{23}n_b+\gamma_{12}}{2}\\ -\frac{\gamma_{2d}}{2}\\ -i(\delta_{a\mu}-\delta_\mu)\end{matrix} & -ig_\mu\overline{b} & 0 & i\Omega & 0 & 0 & iag_o & 0 \\
-iag_o & -ibg_\mu & \begin{matrix}-\frac{\gamma_{23}(n_b+1)}{2}\\ -\frac{\gamma_{13}+\gamma_{3d}}{2}\\ -i(\delta_{ao}-\delta_o)\end{matrix} & 0 & 0 & i\Omega & 0 & 0 & iag_o \\
i\Omega & 0 & 0 & \begin{matrix}-\frac{\gamma_{23}n_b+\gamma_{12}}{2}\\ -\frac{\gamma_{2d}}{2}\\ +i(\delta_{a\mu}-\delta_\mu)\end{matrix} & -i\Omega & -ig_o\overline{a} & ibg_\mu & 0 & 0 \\
0 & i\Omega & 0 & -i\Omega & -\gamma_{12}-\gamma_{23}n_b & -ig_\mu\overline{b} & 0 & ibg_\mu & \gamma_{23}\left(n_b+1\right) \\
0 & 0 & i\Omega & -iag_o & -ibg_\mu & \begin{matrix}-\frac{\gamma_{23}(2n_b+1)}{2}\\ -\frac{\gamma_{12}+\gamma_{13}}{2}\\ -\frac{\gamma_{2d}+\gamma_{3d}}{2}\\ +i(\delta_{a\mu}-\delta_\mu)\\ -i(\delta_{ao}-\delta_o)\end{matrix} & 0 & 0 & ibg_\mu \\
ig_o\overline{a} & 0 & 0 & ig_\mu\overline{b} & 0 & 0 & \begin{matrix}-\frac{\gamma_{23}(n_b+1)}{2}\\ -\frac{\gamma_{13}+\gamma_{3d}}{2}\\ +i(\delta_{ao}-\delta_o)\end{matrix} & -i\Omega & -ig_o\overline{a} \\
0 & ig_o\overline{a} & 0 & 0 & ig_\mu\overline{b} & 0 & -i\Omega & \begin{matrix}-\frac{\gamma_{23}(2n_b+1)}{2}\\ -\frac{\gamma_{12}+\gamma_{13}}{2}\\ -\frac{\gamma_{2d}+\gamma_{3d}}{2}\\ -i(\delta_{a\mu}-\delta_\mu)\\ +i(\delta_{ao}-\delta_o)\end{matrix} & -ig_\mu\overline{b} \\
0 & 0 & ig_o\overline{a} & 0 & \gamma_{23}n_b & ig_\mu\overline{b} & -iag_o & -ibg_\mu & \begin{matrix}-\gamma_{23}(n_b+1)\\ -\gamma_{13}\end{matrix}
\end{bmatrix} \tag{3.37}$$

The steady state density matrix for this atomic scheme will be solved for using the same methods as in Section 3.4.

3.6 Ensemble of Atoms

Thus far we have a method for finding the steady state density matrix, and hence the expectation values for the atomic transition operators, for a single atom. However each of the atoms will have different transition frequencies due to inhomogeneous broadening. The equations for the cavity field (Equations 2.20 and 2.21) require a sum over the σ_{13} and σ_{12} for all the atoms. Due to the large number of atoms in the sample ($\sim 10^{16}$ atoms) we are unable to just perform the sums directly. However, because the number of atoms is so large we are able to approximate these sums as integrals. This means that rather than summing over the all individual atoms each with different detunings, we assume that the detunings are normally distributed and perform an integral with respect to the detunings which is weighted by the distributions. Making

the assumption that the coupling constants $g_o,\ g_\mu$ are real and the same for each atom, the sums are approximated as

$$\sum_k g^*_{o,k}\sigma_{13,k}(\delta_{ao,k},\delta_{a\mu,k}) \approx Ng_o \int \mathrm{d}\delta_{ao} \int \mathrm{d}\delta_{a\mu} G_o(\delta_{ao}) G_\mu(\delta_{a\mu}) \rho_{13}(\delta_{ao},\delta_{a\mu}) \tag{3.38}$$

$$\sum_k g^*_{\mu,k}\sigma_{12,k}(\delta_{ao,k},\delta_{a\mu,k}) \approx Ng_\mu \int \mathrm{d}\delta_{ao} \int \mathrm{d}\delta_{a\mu} G_o(\delta_{ao}) G_\mu(\delta_{a\mu}) \rho_{12}(\delta_{ao},\delta_{a\mu}) \tag{3.39}$$

Here we are integrating over the optical and microwave detunings $\delta_{ao},\ \delta_{a\mu}$ instead of performing the sums over individual atoms with these detunings. The functions $G_o(\delta_{ao})$ and $G_\mu(\delta_{a\mu})$ are normalised functions that describe the distributions of atoms with optical detuning δ_{ao} and microwave detuning $\delta_{a\mu}$. These distribution functions are assumed to be Gaussian functions

$$G_o(\delta_{ao}) = \frac{1}{\sqrt{2\pi}\sigma_o} \exp\left(-\frac{(\delta_{ao}-\mu_o)^2}{2\sigma_o^2}\right) \tag{3.40}$$

$$G_\mu(\delta_{a\mu}) = \frac{1}{\sqrt{2\pi}\sigma_\mu} \exp\left(-\frac{(\delta_{a\mu}-\mu_\mu)^2}{2\sigma_\mu^2}\right) \tag{3.41}$$

Where μ_o is the centre of the optical inhomogeneous line with reference to the optical cavity frequency, likewise μ_μ is the centre of the microwave inhomogeneous line with reference to the microwave cavity frequency. σ_o and σ_μ are the standard deviations of the optical and microwave inhomogeneous distributions.

In this chapter we have described the atomic system we are using, with a three-level atom interacting with various light fields. We have developed a model for finding the steady state density matrix, and then used this to describe the ensemble of inhomogeneously broadened atoms. This gives us a way to calculate the terms which describe the interaction between the ensemble of atoms and the light fields, which will be used for our cavity field equations. The next chapter will be about how to actually solve the cavity field equations numerically, with a lot of thought given to solving the integrals in Equations 3.39 and 3.38.

Chapter 4

Numerical Methods

This chapter will discuss and develop the numerical methods used for simulating the upconversion system. This involves numerically solving the cavity field equations as coupled simultaneous equations. We show how the Master Equation from Chapter 4 can be expressed in an entirely real form, which allows us to use a fast computational method to find the single atom density matrix. From here we develop fast and accurate methods for integrating the single atom density matrix to represent the atomic ensemble. These integrated terms will be later used in the cavity field equations.

4.1 Solving for Cavity Fields

In Chapter 2 we derived the equations for the optical cavity field a and the microwave cavity field b,

$$a = \frac{-iS_{13}(a, b, \delta_o, \delta_\mu)}{(2\gamma_{oc} + \gamma_{oi})/2 - i\delta_o} + \frac{\sqrt{\gamma_{oc}}a_{in}}{(2\gamma_{oc} + \gamma_{oi})/2 - i\delta_o} \tag{4.1}$$

$$b = \frac{-iS_{12}(a, b, \delta_o, \delta_\mu)}{(2\gamma_{\mu c} + \gamma_{\mu i})/2 - i\delta_\mu} + \frac{\sqrt{\gamma_{\mu c}}b_{in}}{(2\gamma_{\mu c} + \gamma_{\mu i})/2 - i\delta_\mu} \tag{4.2}$$

Here for simplicity S_{13} and S_{12} are the sums over the single atom atomic transition operators,

$$S_{13}(a, b, \delta_o, \delta_\mu) = \sum_k g^*_{o,k}\sigma_{13,k}(a, b, \delta_o, \delta_\mu) \tag{4.3}$$

$$S_{12}(a, b, \delta_o, \delta_\mu) = \sum_k g^*_{\mu,k}\sigma_{12,k}(a, b, \delta_o, \delta_\mu) \tag{4.4}$$

The cavity field equations (Equations 4.1 and 4.2) are coupled via the atomic terms. Physically, this means that the optical and microwave fields are

coupled via their interaction with the atoms. We have expressions for a and b in Equations 4.1 and 4.2, but these also depend implicitly on both a and b making them difficult to evaluate. These two coupled complex equations can also be thought of as four coupled real equations for the real and imaginary parts of a and b,

$$a_r = \mathrm{Re}\left(\frac{-iS_{13}(a_r, a_i, b_r, b_i)}{(2\gamma_{oc} + \gamma_{oi})/2 - i\delta_o} + \frac{\sqrt{\gamma_{oc}}a_{in}}{(2\gamma_{oc} + \gamma_{oi})/2 - i\delta_o}\right) \tag{4.5a}$$

$$a_i = \mathrm{Im}\left(\frac{-iS_{13}(a_r, a_i, b_r, b_i)}{(2\gamma_{oc} + \gamma_{oi})/2 - i\delta_o} + \frac{\sqrt{\gamma_{oc}}a_{in}}{(2\gamma_{oc} + \gamma_{oi})/2 - i\delta_o}\right) \tag{4.5b}$$

$$b_r = \mathrm{Re}\left(\frac{-iS_{12}(a_r, a_i, b_r, b_i)}{(2\gamma_{\mu c} + \gamma_{\mu i})/2 - i\delta_\mu} + \frac{\sqrt{\gamma_{\mu c}}b_{in}}{(2\gamma_{\mu c} + \gamma_{\mu i})/2 - i\delta_\mu}\right) \tag{4.5c}$$

$$b_i = \mathrm{Im}\left(\frac{-iS_{12}(a_r, a_i, b_r, b_i)}{(2\gamma_{\mu c} + \gamma_{\mu i})/2 - i\delta_\mu} + \frac{\sqrt{\gamma_{\mu c}}b_{in}}{(2\gamma_{\mu c} + \gamma_{\mu i})/2 - i\delta_\mu}\right) \tag{4.5d}$$

Solutions for a and b can be found numerically with a root finding algorithm with both vector valued inputs and outputs [61]. If we define

$$\mathbf{X} = [a_r,\ a_i,\ b_r,\ b_i]^T$$

we can think of the right hand side of Equations 4.5 as a function of this vector $\mathbf{X}$, $F(\mathbf{X})$. We then solve for a_r, a_i, b_r, b_i by numerically solving,

$$F(\mathbf{X}) - \mathbf{X} = 0 \tag{4.6}$$

Solving for $\mathbf{X}$ will give us our intra cavity field amplitudes, from which it is simple to calculate the output fields and conversion efficiency.

4.2 Single Atom Coherences

To be able to solve for a and b we need to be able to evaluate S_{13} and S_{12} as functions of both the complex cavity field amplitudes a and b, and the optical and microwave detunings δ_o and δ_μ. To find S_{13} and S_{12} we must first find the single atom coherence terms. This is done by solving for the steady state density matrix using

$$\mathcal{L}\rho = 0_{\mathbb{1}} \tag{4.7}$$

where $0_{\mathbb{1}} = [1, 0, 0, 0, 0, 0, 0, 0, 0]^T$ (Equation 3.33), as described in Section 3.4.

The density matrix is complex and Hermitian, this means we can transform it into a real, non-symmetric matrix which contains all the same information. This allows us to use a very fast solver for real matrices, which is important

because for the calculations we will need to evaluate ρ many times. Although there exist fast solvers for complex matrices we transform ρ to be real to take advantage of the property that it is Hermitian. If we kept it as a complex matrix, the solver would have to solve for the real and imaginary parts of each component, which would be 18 terms in total. However because ρ is Hermitian there are only really 9 independent real parameters to solve for. So by transforming ρ to be real, we find 9 terms which fully define ρ rather than solving for 18.

The transformation matrix is

$$C = \frac{1}{2}\begin{bmatrix} 2 & 0 & 0 & 0 & 0 & 0 & 0 & 0 & 0 \\ 0 & 0 & 0 & 0 & 2 & 0 & 0 & 0 & 0 \\ 0 & 0 & 0 & 0 & 0 & 0 & 0 & 0 & 2 \\ 0 & 1 & 0 & 1 & 0 & 0 & 0 & 0 & 0 \\ 0 & i & 0 & -i & 0 & 0 & 0 & 0 & 0 \\ 0 & 0 & 1 & 0 & 0 & 0 & 1 & 0 & 0 \\ 0 & 0 & i & 0 & 0 & 0 & -i & 0 & 0 \\ 0 & 0 & 0 & 0 & 0 & 1 & 0 & 1 & 0 \\ 0 & 0 & 0 & 0 & 0 & i & 0 & -i & 0 \end{bmatrix} \tag{4.8}$$

This transforms ρ, in vector form, into a real vector

$$\rho_{real} = C\rho \tag{4.9}$$

$$= \left[\rho_{11}, \rho_{22}, \rho_{33}, \tfrac{\rho_{12}+\rho_{21}}{2}, i\tfrac{\rho_{21}-\rho_{12}}{2}, \tfrac{\rho_{13}+\rho_{31}}{2}, i\tfrac{\rho_{31}-\rho_{13}}{2}, \tfrac{\rho_{23}+\rho_{32}}{2}, i\tfrac{\rho_{32}-\rho_{23}}{2}\right]^T \tag{4.10}$$

$\mathcal{L}$ is transformed into a real matrix using

$$\mathcal{L}_{real} = C\mathcal{L}C^{-1} \tag{4.11}$$

$0_{\mathbb{1}}$ is not changed by this transformation, $C0_{\mathbb{1}} = 0_{\mathbb{1}}$. We now solve for ρ_{real} by using the LAPACK routine dgesv, designed for solving a system of real linear equations [62], to solve the equation

$$\mathcal{L}_{real}\rho_{real} = 0_{\mathbb{1}} \tag{4.12}$$

And then at any stage we can find ρ by transforming back, $\rho = C^{-1}\rho_{real}$.

4.3 Atomic ensemble terms

Now that we can solve for the steady state single atom density matrix we can use this to find the atomic ensemble terms S_{13} and S_{12} (Equations 4.13 and

4.14). Like the single atom coherences, these ensemble terms will depend on the cavity fields a and b, as well as the atomic detunings. S_{13} and S_{12} are found by integrating the single atom coherences over the atomic detunings, with Gaussian functions representing the inhomogeneous broadening distributions as described in Section 3.6,

$$S_{13} = Ng_o \int \mathrm{d}\delta_{ao} \int \mathrm{d}\delta_{a\mu} G_o(\delta_{ao}) G_\mu(\delta_{a\mu}) \rho_{13}(a, b, \delta_{ao}, \delta_{a\mu}) \tag{4.13}$$

$$S_{12} = Ng_\mu \int \mathrm{d}\delta_{ao} \int \mathrm{d}\delta_{a\mu} G_o(\delta_{ao}) G_\mu(\delta_{a\mu}) \rho_{12}(a, b, \delta_{ao}, \delta_{a\mu}) \tag{4.14}$$

Plotting Coherences

We have to be careful when numerically evaluating the integrals in Equations 4.13 and 4.14. The functions ρ_{13} and ρ_{12} will have sharp peaks, as can be seen in Figures 4.1 and 4.2, the width of these peaks is determined by the homogeneous linewidths. Because of the large ratio between the inhomogeneous and homogeneous linewidths, when we numerically integrate over the inhomogeneous distribution we must be careful that there are enough integration points close to the peaks, so that the peaks aren't missed. In Figures 4.1 and 4.2 the different elements of ρ were calculated as functions of the optical and microwave detunings, for realistic physical parameters (described later in Section 5.2). Figure 4.1 shows the elements of ρ when the input microwave field is very small, this will be close to the single photon regime used in quantum information. Figure 4.2 shows the elements of ρ for a much larger microwave field, such as is used in some of the experiments in [46].

For low microwave power, we can see that most of the atoms are still in the ground state, although in the peaked regions they have around a 20% chance of being in one of the excited states. When the transitions between the energy levels are driven this generates coherence between the states, and so the coherence between the states is peaked in the same areas as the population fraction. When there is a large microwave field driving the $|1\rangle \rightarrow |2\rangle$ transition, the atoms have about the same probability of being in one of these states. This is because the microwave field is strong enough such that half the atoms have been driven into the $|2\rangle$ state and so any additional driving will simply drive them back to $|1\rangle$, and so an equilibrium is reached. There is a similar process for the case with low microwave field, where the atoms have a similar probability of being in the $|2\rangle$ or $|3\rangle$ state, because of the strong pump laser. In the case with the strong microwave field, we see an interesting effect in the coherence terms ρ_{13} and ρ_{23} where these have minima in the middle of the peaked regions. This may be due to the Autler-Townes effect, where for

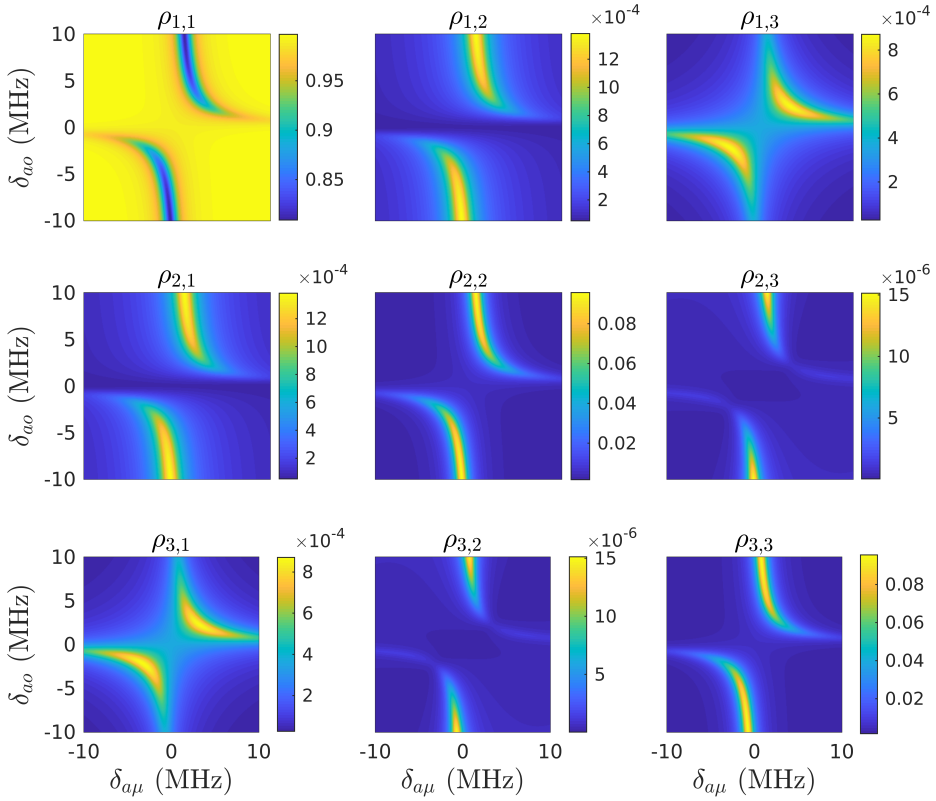

Figure 4.1: The absolute value of the different elements of ρ for very low microwave field as a function of the microwave and optical atomic detunings, such as used in the single photon regimes. ρ_{11} is larger than all the other terms because the field is weak and so atoms have a low probability of being driven into one of the higher energy levels.

certain microwave and optical frequencies close to a resonance, the material becomes transparent to the pump laser [63]. If the material was transparent to the pump laser for these frequencies then it would not generate coherence between the states.

4.3.1 Finding Atomic Degenerate Dressed States

The peaked and rapidly changing regions for our coherences (Figures 4.1 and 4.2) correspond to the detunings which cause the atomic Hamiltonian to have degenerate eigenstates. When there are no input fields, the eigenstates of the atomic Hamiltonian are just the atomic energy levels. However, when there are light fields driving transitions between these levels, the eigenstates become

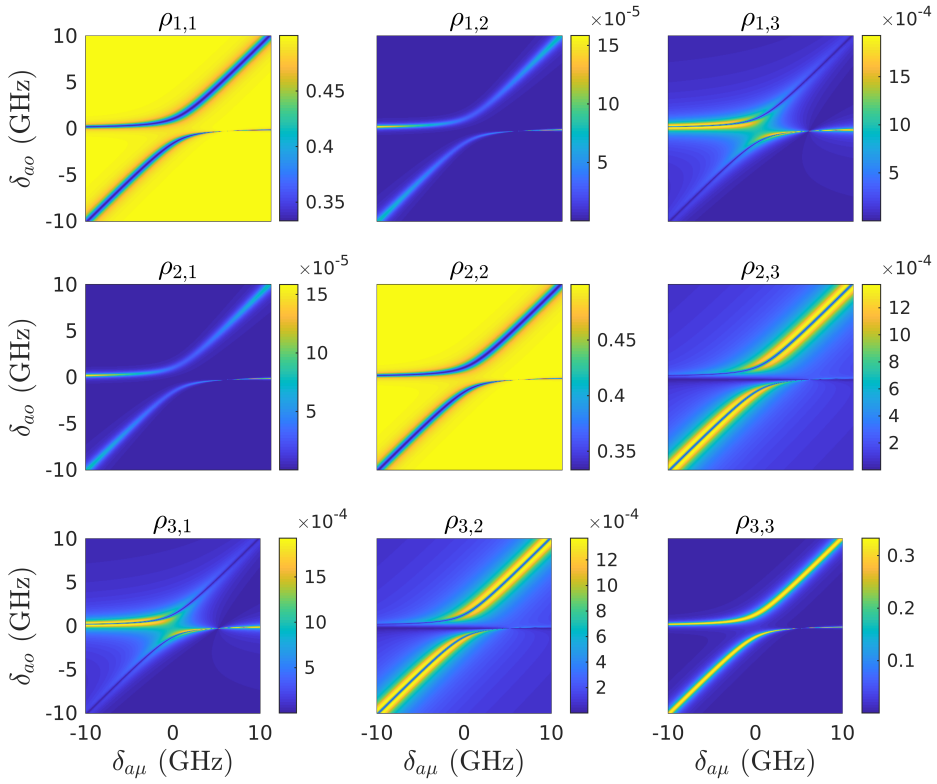

Figure 4.2: The absolute value of the different elements of ρ as a function of the microwave and optical detunings for a large microwave field, such as is used in experiments. There is significant population of the second level, given by ρ_{22}, because of the large microwave field, which pumps the photons from the ground state into this level. Note the dip in $\rho_{1,3}$ and $\rho_{2,3}$ close to the resonance, possibly due to the Autler-Townes effect.

the dressed states of the combined atom and fields. In the frame rotating with the fields which we are working in, when two levels are degenerate it means they have the same detuning from the input fields. This means the degenerate dressed states have the same detuning from the input fields, and so will have an absolute frequency difference resonant with the input field. With these detunings, the input fields will directly drive transitions between the dressed states, rather than the atomic transitions. This causes the peaks in our density matrix because it corresponds to directly driving transitions between eigenstates of the system. For a given optical detuning δ_{ao} there will be a microwave detuning $\delta_{a\mu}$ such that the atomic Hamiltonian has degenerate eigenvalues, we will refer to these detunings as the degenerate dressed state detunings.

The degenerate dressed state detunings will show us the regions where the coherences are sharply peaked, we can use this information to make sure our numerical integration is accurate around these regions.

The eigenvalues of the Hamiltonian are given by

$$\det(\hat{H}_{\text{atom}} - \mathbb{1}\lambda) = 0 \tag{4.15}$$

where λ takes the place of an eigenvalue. Because $\hat{H}_{\text{atom}}$ is a 3×3 matrix, this determinant will be a third order polynomial in λ. For a third order polynomial, if the discriminant is zero, then the polynomial has at least 2 repeated roots. These repeated roots will correspond to degenerate eigenvalues of the atomic Hamiltonian, which correspond to our degenerate dressed states. So we want to find detunings for which,

$$\text{Disc}_\lambda(\det(\hat{H}_{\text{atom}}(\delta_{ao}, \delta_{a\mu}) - \mathbb{1}\lambda)) = 0 \tag{4.16}$$

where Disc_λ calculates the discriminant of the polynomial function of λ. $\hat{H}_{\text{atom}}$ is Hermitian, like all observables, and so the eigenvalues λ are all real, however they may be zero-valued. This means that the roots of Equation 4.15 are all real, and so its discriminant in Equation 4.16 is always non-negative. Numerically it is difficult to quickly find the zeros for Equation 4.16 directly. However, because it is non-negative, all the zeros lie at minima, where the derivative with respect to both δ_{ao} and $\delta_{a\mu}$ is zero.

So for a given optical detuning we can use a root finding algorithm find the value of $\delta_{a\mu}$ that solves

$$\frac{\mathrm{d}}{\mathrm{d}\delta_{ao}}\left[\text{Disc}_\lambda(\det(\hat{H}_{\text{atom}}(\delta_{ao}, \delta_{a\mu}) - \mathbb{1}\lambda))\right] = 0 \tag{4.17}$$

This gives us the detunings of the degenerate dressed states.

For root finding it is useful to have an initial guess for the detunings which correspond to the degenerate dressed states, for these we assume a is negligible, and then work either the regime where we can ignore the pump laser compared to the microwaves or when we can ignore the microwaves compared to the pump. In the case where the pump is small compared to the microwaves, $\Omega \to 0$, and so we have

$$\hat{H}_{\text{atom}} = \begin{bmatrix} 0 & \overline{g_\mu b} & 0 \\ g_\mu b & \delta_{a\mu} - \delta_\mu & 0 \\ 0 & 0 & \delta_{ao} - \delta_o \end{bmatrix} \tag{4.18}$$

Here the degenerate dressed state detunings are found by

$$\delta_{a\mu} = -\frac{|g_\mu b|^2}{\delta_{ao} - \delta_o} + \delta_{ao} - \delta_o + \delta_\mu \tag{4.19}$$

So for a given optical detuning δ_{ao}, Equation 4.19 gives the value of $\delta_{a\mu}$ such that the dressed states of the atomic Hamiltonian are degenerate.

In the case where the microwaves are negligible compared to the pump laser we have

$$\hat{H}_{\text{atom}} = \begin{bmatrix} 0 & 0 & 0 \\ 0 & \delta_{a\mu} - \delta_\mu & \overline{\Omega} \\ 0 & \Omega & \delta_{ao} - \delta_o \end{bmatrix} \tag{4.20}$$

And the degenerate dressed states are found with

$$\delta_{a\mu} = \frac{|\Omega|^2}{\delta_{ao} - \delta_o} + \delta_\mu \tag{4.21}$$

The found degenerate dressed state detunings are plotted over ρ_{12} and ρ_{13} in Figure 4.3 for small microwave field, and Figure 4.4 for large microwave field, showing that they fit very well to the peaked regions of the density matrix.

4.3.2 Dressed States when using the Excited State Microwave Transition

We can use the same methods to find the detunings which correspond to the degenerate dressed states for the atomic scheme which uses the excited state microwave transition. The atomic Hamiltonian used in Equation 4.17 will be the Hamiltonian for the atomic scheme using the excited state microwave transition (Section 3.5), and the initial guesses for finding the degenerate dressed states will need to be changed. The initial guesses for the detunings of the degenerate dressed states for this atomic scheme can be found by

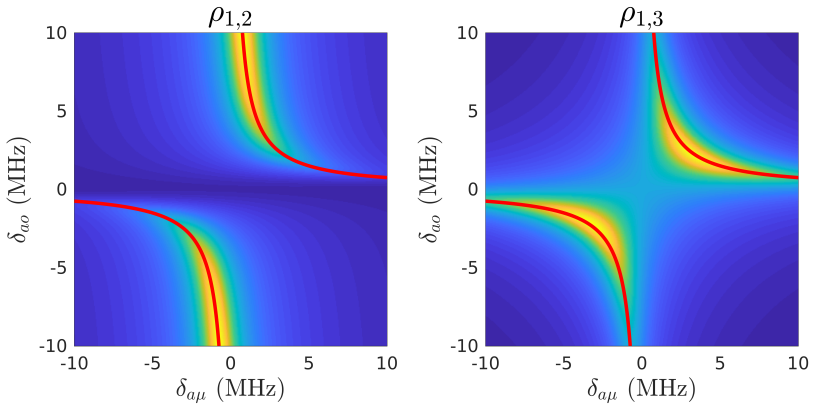

Figure 4.3: The absolute value for ρ_{12} and ρ_{13} for small microwave field. The red line represents the detunings of the degenerate dressed states of the Hamiltonian, and was found using an initial guess assuming no microwave field and large laser pump.

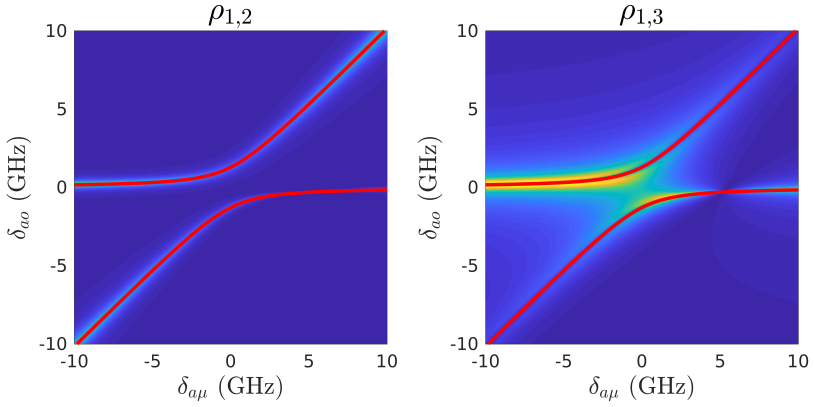

Figure 4.4: The absolute value for ρ_{12} and ρ_{13} for large microwave field. The red line represents the detunings of degenerate dressed states of the Hamiltonian, and was found using an initial guess assuming large microwave field and negligible laser pump.

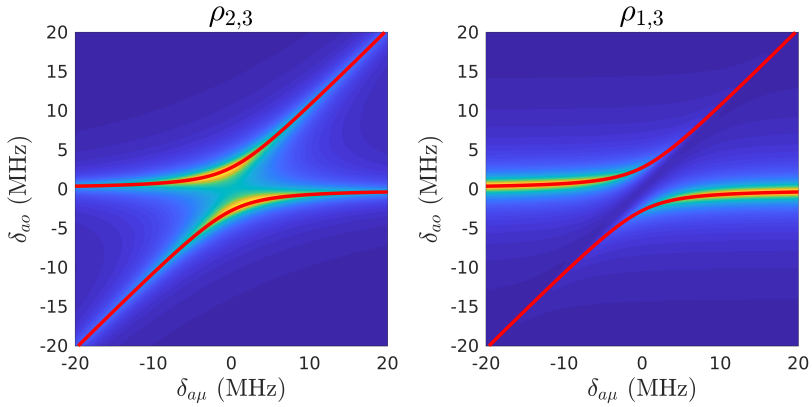

Figure 4.5: The absolute value for ρ_{23} and ρ_{13}, using the excited state microwave transition, for small microwave field. The red line represents the detunings of the degenerate dressed states of the Hamiltonian, and was found using an initial guess assuming no microwave field and large laser pump.

simply swapping Ω and $g_\mu b$ in the equations for the scheme which uses the ground state microwave transition. So when using the excited state microwave transition, for very low microwave field the degenerate dressed states will be close to

$$\delta_{a\mu} = -\frac{|\Omega|^2}{\delta_{ao} - \delta_o} + \delta_{ao} - \delta_o + \delta_\mu \tag{4.22}$$

and when the microwave field is very large,

$$\delta_{a\mu} = \frac{|g_\mu b|^2}{\delta_{ao} - \delta_o} + \delta_\mu \tag{4.23}$$

The degenerate dressed state detunings found using these initial guesses are plotted over ρ_{23} and ρ_{13} in Figure 4.5 for small microwave field, and Figure 4.6 for large microwave field.

4.4 Numerical Integration

Evaluating the atomic coherence terms S_{13} and S_{12} requires us to perform a 2 dimensional integral over the optical and microwave detunings. We will integrate each of the density matrix terms together because as well as calculating the coherences this will give us interesting information about the population of the levels. The function we are integrating is the density matrix, multiplied by the inhomogeneous broadening distributions. We choose the

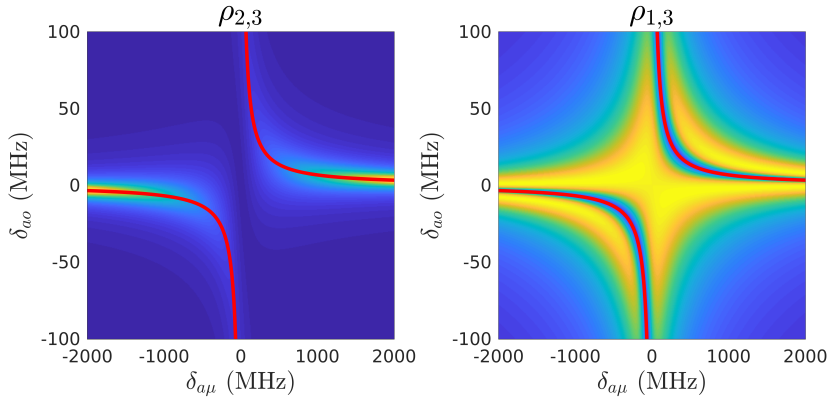

Figure 4.6: The absolute value for ρ_{23} and ρ_{13}, using the excited state microwave transition, for large microwave field. The red line represents detunings of the degenerate the dressed states of the Hamiltonian, and was found using an initial guess assuming large microwave field and negligible laser pump.

integral over δ_{ao} as the outer integral, and $\delta_{a\mu}$ as the inner integral,

$$\int G_o(\delta_{ao}) \left[\int G_\mu(\delta_{a\mu}) \rho(\delta_{ao}, \delta_{a\mu}) \mathrm{d}\delta_{a\mu} \right] \mathrm{d}\delta_{ao} \tag{4.24}$$

We can split these integrals into different regions, this allows us to take the more difficult regions into account,

$$\sum_i \int_{\delta_{ao,i}}^{\delta_{ao,i+1}} G_o(\delta_{ao}) \left[\sum_j \int_{\delta_{a\mu,j}(\delta_{ao})}^{\delta_{a\mu,j+1}(\delta_{ao})} G_\mu(\delta_{a\mu}) \rho(\delta_{ao}, \delta_{a\mu}) \mathrm{d}\delta_{a\mu} \right] \mathrm{d}\delta_{ao} \tag{4.25}$$

The bounds for the inner $\delta_{a\mu}$ integral can depend on the value of δ_{ao}. This is why we have developed the method for finding $\delta_{a\mu}$ corresponding to δ_{ao} for the degenerate dressed states. To avoid double counting a region we sort the bounds such that,

$$\delta_{ao,i} < \delta_{ao,i+1}, \;\; \delta_{a\mu,j} < \delta_{a\mu,j+1} \tag{4.26}$$

Each of these bounded integrals will be evaluated using Gauss-Lobatto quadrature, for arbitrary bounds this is,

$$\int_a^b f(x)dx \approx \frac{b-a}{2} \sum_l^n w_l \; f\left(\frac{b-a}{2}(x_l + 1) + a \right) \tag{4.27}$$

where n is the number of points, w_l are the Gauss-Lobatto weights, and x_l are the Gauss-Lobatto points for the interval $[-1, 1]$ [64]. This integral

approximation is exact if $f(x)$ is a polynomial of degree $2n-3$ or less [65], our functions are not exactly polynomials but for high enough n this will still give a very accurate approximation. This method is much more accurate than Simpson's rule or the trapezoidal rule for numerical integration for the same number of points. Gauss-Lobatto quadrature is used rather than more common quadrature methods, such as Gauss-Legendre quadrature, because Gauss-Lobatto quadrature uses the end points of the region for the integration points. This means the numerical integration can take into account if the function changes rapidly near the end points.

For the integral over the optical detuning δ_{ao} we will split the integral in several regions over the inhomogeneous broadening ($\mu_o, \mu_o \pm \sigma_o,\ \mu_o \pm 3\sigma_o,\ \mu_o \pm 10\sigma_o$), as well as around the input detuning and the broadening due to the optical homogeneous broadening ($\delta_o,\ \delta_o \pm \gamma_{3d},\ \delta_o \pm 5\gamma_{3d}$) as shown in Figure 4.7. For the integral over the microwave detuning $\delta_{a\mu}$ this is also split over inhomogeneous broadening ($\mu_\mu,\ \mu_\mu \pm \sigma_\mu,\ \mu_\mu \pm 3\sigma_\mu,\ \mu_\mu \pm 10\sigma_\mu$) and the homogeneous broadening ($\delta_\mu,\ \delta_\mu \pm \gamma_{2d},\ \delta_\mu \pm 5\gamma_{2d}$), as well as around the degenerate dressed state detuning which will depend on the value of δ_{ao} (Figure 4.8).

As indicated in Equation 4.24, the integral over δ_{ao} will be evaluated as the outer integral. This means that the integrals will be split up as indicated in Figure 4.7, and then for each numerical integration point, we will evaluate the integral over $\delta_{a\mu}$. The integral over $\delta_{a\mu}$ will be similarly split up, as shown in Figure 4.8. This integral will be split around the degenerate dressed state detunings, which will depend on the specific value of the outer integral δ_{ao} integration point we are evaluating the inner $\delta_{a\mu}$ integral for.

Using this method of integration we are able to quickly and accurately integrate over the optical and microwave inhomogeneous distributions. The values of the degenerate dressed state detunings, which split the integrals, will depend on the input fields. This allows us to perform the integrals for a range of different powers of the input microwaves; from the single photon regime to the regime where microwaves are so powerful they saturate the transition, as we will see in later chapters.

Integrating over the inhomogeneous distribution using a simpler method such as Simpson's rule will be much slower, because to achieve the same accuracy as a quadrature rule many more points must be evaluated. Simpler methods may be able to give accurate results when the fields are far detuned from the atoms, because the peaked regions are far from the centre of the inhomogeneous line and so won't have much influence. But when close to resonance, the peaked regions will be close to the centre of the inhomogeneous distribution and so will have a large effect. Therefore, when close to resonance it is necessary to take these peaked regions into account, otherwise the points

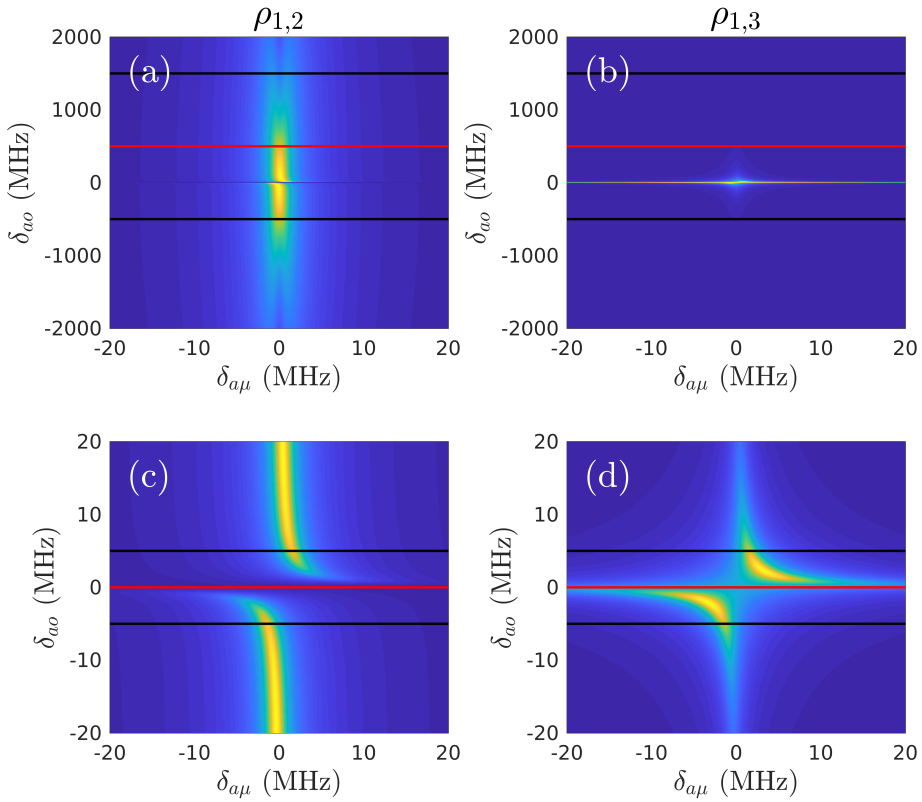

Figure 4.7: Demonstration of how the integrals over the optical detuning δ_{ao} are split into regions. (a) and (c) show ρ_{12}, (b) and (d) show ρ_{13} as a function of optical and microwave detunings. The horizontal lines indicate where the integrals over δ_{ao} will be split. (a) and (b) show how the inhomogeneous linewidth is integrated over; the red line indicates the centre of the inhomogeneous line μ_o and the black lines indicate one standard deviation to either side of this, $\mu_o \pm \sigma_o$. (c) and (d) show how the integral is split up because of the homogeneous linewidth, with the red line at δ_o, and the black lines at $\delta_o \pm 5\gamma_{3d}$. The difference in the range of δ_{ao} in the top and bottom rows is because the inhomogeneous linewidth is so much larger than the homogeneous linewidth.

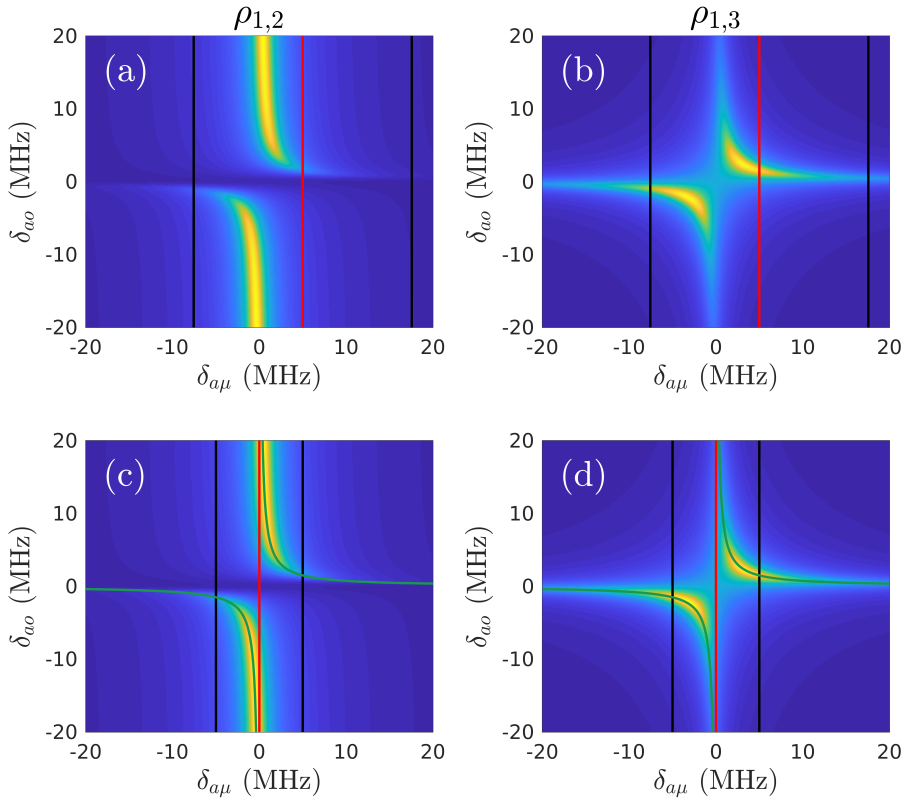

Figure 4.8: Demonstration of how the integrals over the microwave detuning $\delta_{a\mu}$ are split into regions, similar to Figure 4.7. The two columns show the absolute values of ρ_{12} and ρ_{13} as a function of optical and microwave detunings, and the lines indicate where the integrals will be split. (a) and (b) show how the integral is split up over the inhomogeneous linewidth, the red line is at the centre of the inhomogeneous line μ_μ, and the black lines are at $\mu_\mu \pm \sigma_\mu$. In (c) and (d) the red line is at δ_μ and the black lines indicate $\delta_\mu \pm 5\gamma_{2d}$. The green line shows the degenerate dressed state detunings which we will split the microwave integral over.

used for numerical integration could miss them, and give an incorrect result.

In this chapter we have outlined the various numerical methods we will use to simulate our double cavity upconversion process. We showed how the equations for the cavity fields can be solved numerically as a set of simultaneous equations. The single atom coherence terms can be solved for by making a transformation such that the density matrix is entirely real, which allows us to use a fast LAPACK routine to find the steady state. We also developed methods to deal with our inhomogeneously broadened distribution of atoms. The density matrix elements as functions of the atomic detunings have sharp peaks related to the homogeneous broadening, and so these must be accounted for when integrating over the inhomogeneous distribution. These peaked regions correspond to the atomic detunings where the dressed states of the atomic Hamiltonian are degenerate. We developed a way to find these detunings, and the integrals will be split around them. This allows us to integrate over the inhomogeneous distribution accurately without missing the peaks.

These methods allow us to simulate our upconversion process as we will see in the following chapters.

Chapter 5

Comparison with Single Pass Experiments

To make sure that our model is accurate, this chapter will compare simulations with experimental data. We will begin with a description of the experimental set up, which is similar to the system outlined in Chapter 2 but with no cavity to enhance the optical field. We will discuss the experimental parameters used for these simulations, and then compare the simulations for the optical and microwave fields to the experiment.

5.1 Single Pass Simulations

The experiments which we will compare our simulations to, were performed at low temperature using a single pass optical set up, meaning there is no optical cavity for either the pump laser or the optical output field. These experiments will be a useful test of the accuracy of the simulations. The experimental set up involved a crystal of Er:YSO inside a microwave resonator, driven by an optical pump laser as shown in Figure 5.1. All experiments were performed by Gavin King.

The set up for these experiments involved a crystal of Er:YSO in a microwave cavity was cooled to cryogenic temperatures using a dilution fridge. A magnetic field was applied to split the two level system with a single optical transition into a four level system. Depending on whether the ground state or excited state spin transition is being used, the magnetic field will be adjusted such that the relevant transition is close to resonant with the microwave cavity. One of the optical transitions is driven close to resonance with the optical pump laser. Both the frequency of the input microwaves and the pump laser can be varied, as well as the magnetic field.

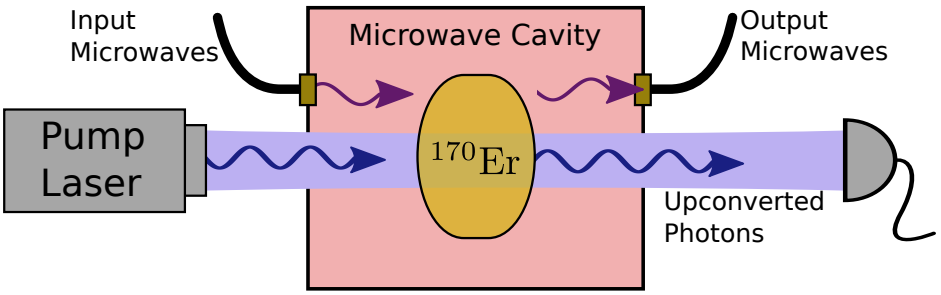

Figure 5.1: Diagram showing the set up for the single pass experiments. The Er doped crystal is inside a microwave cavity with input and output ports. The crystal is in the beam path of an optical pump laser, and the signal from the pump laser and upconverted photons is measured on an optical detector.

Measurements of the microwave and optical field are made using two different methods. The output microwave field is measured by simply recording the transmission through the microwave cavity. For measuring the output optical field, which is the field of the upconverted photons, a heterodyne measurement is taken by measuring the beat signal between the upconverted signal and the optical pump. For the heterodyne measurement, the experiment was not fully calibrated, so we only have the relative magnitude of the optical signal, and so do not know the experimental conversion efficiency.

The theoretical model and numerical methods have been developed for a set up of both a microwave and optical cavity, however it is easily modified for the case where there is only a microwave cavity. Because there is no optical cavity, when an optical signal photon is generated it will immediately leave the crystal, and so we can assume the optical field in the crystal is negligible,

$$\tilde{a} \approx 0 \tag{5.1}$$

However the optical pump field will still be significant. So for the ground state system we can solve for $\tilde{b}$,

$$\tilde{b} = \frac{-i \sum_k g^*_{\mu,k} \sigma_{12,k}(a=0, b, \delta_o, \delta_\mu) + \sqrt{\gamma_{\mu c}} \tilde{b}_{in}}{(2\gamma_{\mu c} + \gamma_{\mu i})/2 - i\delta_\mu} \tag{5.2}$$

using the numerical root finding method discussed in Section 4.1.

The optical output field amplitude will be proportional to the sum over the atomic transition operators for the $|3\rangle \rightarrow |1\rangle$ transition, for the microwave cavity field amplitude b

$$a_{out}(b, \delta_o, \delta_\mu) \propto \sum_k g^*_{o,k} \sigma_{13,k}(a=0, b, \delta_o, \delta_\mu) = S_{13}(b, \delta_o, \delta_\mu) \tag{5.3}$$

In this experiment, the entire crystal will be in the microwave field, due to the resonator and mode geometry, however only a fraction of the atoms will be in the optical pump beam path as shown in Figure 5.1. This must be taken into account for the simulations to show the same phenomena as the experiments. This means the atoms which are not in the optical beam path will not have the $|2\rangle \rightarrow |3\rangle$ transition driven by the electric field, and hence $\Omega = 0$. Hence the atomic interaction term in Equation 5.2 will be expressed as two terms to include the atoms which are driven and not driven by the optical pump,

$$\begin{aligned}\sum_k^N g^*_{\mu,k}\sigma_{12,k} &= \sum_k^{N_o} g^*_{\mu,k}\sigma_{12,k}\Big|_{\Omega=\Omega} + \sum_k^{N-N_o} g^*_{\mu,k}\sigma_{12,k}\Big|_{\Omega=0} \\ &\approx N_o g_\mu \int \mathrm{d}\delta_{ao}\ \mathrm{d}\delta_{a\mu} G_o(\delta_{ao}) G_\mu(\delta_{a\mu}) \rho_{12}(\delta_{ao},\delta_{a\mu})\Big|_{\Omega=\Omega} \\ &\quad + (N-N_o) g_\mu \int \mathrm{d}\delta_{ao}\ \mathrm{d}\delta_{a\mu} G_o(\delta_{ao}) G_\mu(\delta_{a\mu}) \rho_{12}(\delta_{ao},\delta_{a\mu})\Big|_{\Omega=0} \\ &= S_{12} + S_{12,\Omega=0}\end{aligned}$$

where N is the total number of atoms which are all in the microwave cavity, and N_o is the number of atoms in the optical beam path. Taking into account the atoms not in the pump beam path, Equation 5.2 becomes

$$\tilde{b}(\delta_o,\delta_\mu) = -i\frac{S_{12}(b,\delta_o,\delta_\mu) + S_{12,\Omega=0}(b,\delta_o,\delta_\mu)}{(2\gamma_{\mu c}+\gamma_{\mu i})/2 - i\delta_\mu} + \frac{\sqrt{\gamma_{\mu c}}\tilde{b}_{in}}{(2\gamma_{\mu c}+\gamma_{\mu i})/2 - i\delta_\mu} \quad (5.4)$$

For the microwaves we will measure transmission through the cavity, which refers to the ratio of power into the cavity against power out of the cavity. Because the output and input photons have the same frequency we can express this as

$$\text{Transmission} = \frac{P_{out}}{P_{in}} = \frac{|b_{out}|^2}{|b_{in}|^2} \quad (5.5)$$

For the optical signal we mainly care about the conversion number efficiency, the ratio of optical output photons to microwave input photons

$$\text{Conversion Efficiency} = \frac{n_{o,out}}{n_{\mu,in}} = \frac{|a_{out}|^2}{|b_{in}|^2} \propto \frac{|S_{13}|^2}{|b_{in}|^2} \quad (5.6)$$

It isn't very useful to compare power conversion efficiency because the optical photons have several orders of magnitude more energy than the microwave photons. For quantum computing applications we care about the number of photons converted, not the power.

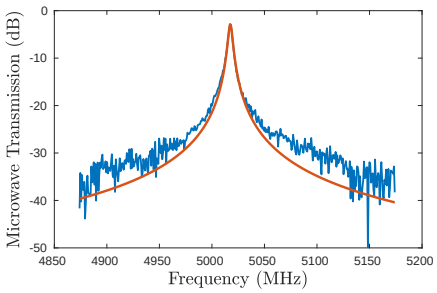

Figure 5.2: The experimental microwave cavity transmission spectrum (dB) far detuned from the atomic transition frequency, and the Lorentzian fit used to find $\omega_{c\mu}$, $\gamma_{\mu c}$ and $\gamma_{\mu i}$.

5.2 Experimental Parameters

To be able to simulate the experiments we now need to know the physical parameters which characterise each of the parts of the system. These include parameters describing the microwave cavity, the cavity fields and the atoms.

5.2.1 Microwave Cavity

Both the microwave and optical cavities are characterised by three parameters in our model, these are the central frequency, the coupling loss rate, and the intrinsic loss rate. For the experiment there is no optical cavity, so we only need to know the parameters for the microwave cavity.

For the microwave cavity these parameters are found from the Lorentzian cavity spectrum (Figure 5.2). When the cavity is empty or very far detuned from the atomic microwave transition frequency then the spectrum of transmission through the cavity is Lorentzian, and given by

$$\left|\frac{b_{out}}{b_{in}}\right|^2 = \frac{\gamma_{\mu c}^2}{\frac{(2\gamma_{\mu c}+\gamma_{\mu i})^2}{4} + (\omega_\mu - \omega_{c\mu})^2} \tag{5.7}$$

The spectrum of the far detuned cavity can be fit to this Lorentzian to find the cavity central frequency $\omega_{c\mu}$, the coupling loss $\gamma_{\mu c}$, and the cavity intrinsic loss $\gamma_{\mu i}$. When the atoms are far detuned from the microwave cavity, the cavity is strongly overcoupled.

From the fit we have the following parameters

$$\omega_{c\mu} = 2\pi \cdot 5017 \text{ MHz} \tag{5.8}$$
$$\gamma_{\mu c} = 2\pi \cdot 1.495\,\text{MHz} \tag{5.9}$$
$$\gamma_{\mu i} = 2\pi \cdot 1.149\,\text{MHz} \tag{5.10}$$

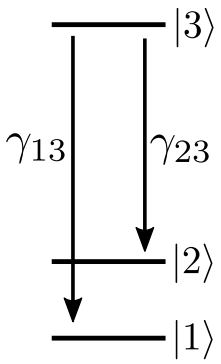

Figure 5.3: Population decay from the optical excited level, $|3\rangle$, to $|1\rangle$ and $|2\rangle$, and the associated decay constants.

5.2.2 Atomic Loss Parameters

The population lifetime of the optical excited state $|3\rangle$ has been measured to be around 11 ms [66, 28]. From this excited state the atom can decay into either of the Zeeman split lower levels $|1\rangle$ or $|2\rangle$ (Figure 5.11). The ratio of decay into each state is determined by the dipole moment of the transitions [54]

$$\gamma_{13} = \frac{d_{13}^2}{d_{13}^2 + d_{23}^2} \frac{1}{11\,\text{ms}} \tag{5.11}$$

$$\gamma_{23} = \frac{d_{23}^2}{d_{13}^2 + d_{23}^2} \frac{1}{11\,\text{ms}} \tag{5.12}$$

Where d_{13} and d_{23} are the dipole moments for the $|1\rangle \rightarrow |3\rangle$ and $|2\rangle \rightarrow |3\rangle$ transitions,

$$d_{13} = 1.63 \times 10^{-32}\,\text{C m} \tag{5.13}$$

$$d_{23} = 1.15 \times 10^{-32}\,\text{C m} \tag{5.14}$$

The population lifetime of the excited state of the microwave transition $|2\rangle$ is around 11 s [67],

$$\gamma_{12} = \frac{1}{11}\,\text{Hz} \tag{5.15}$$

The external dephasing rates for levels $|2\rangle$ and $|3\rangle$ are from [46],

$$\gamma_{2d} = 1 \times 10^6\,\text{Hz} \tag{5.16}$$

$$\gamma_{3d} = 1 \times 10^6\,\text{Hz} \tag{5.17}$$

The atomic decay and loss dynamics will also be affected by the temperature of the system, due to the presence of thermal photons exciting the

microwave transition. The Master equation method models this by coupling the atoms to a thermal bath with photon occupation n_{bath}, which is described by the Planck distribution,

$$n_{bath} = \frac{1}{\exp\left(\hbar\omega/k_B T\right) - 1} \tag{5.18}$$

Here ω is the microwave transition frequency.

5.2.3 Atomic Frequencies

At zero magnetic field we will simply have a two level system separated by an optical transition with frequency f_0, the two levels are just the ground and excited electronic states $|g\rangle$ and $|e\rangle$ which are the $^4\mathrm{I}_{15/2}(\mathrm{Z}_1)$ and $^4\mathrm{I}_{13/2}(\mathrm{Y}_1)$ levels of erbium respectively. When the magnetic field is applied both the ground and excited levels of the optical transition will split, this results in a four level system. The four levels are the Zeeman split levels for the two electronic states $|g,-\rangle$, $|g,+\rangle$, $|e,-\rangle$, $|e,+\rangle$. The magnitude of the splitting of the ground and excited states will depend on the g-factors for each of those transitions,

$$\omega_g = g_g \mu_B B \tag{5.19}$$

$$\omega_e = g_e \mu_B B \tag{5.20}$$

where ω_g and ω_e are the Zeeman splittings of the electronic ground and excited levels, and g_g and g_e are the respective g-factors, B is the applied magnetic field, and μ_B is the Bohr magneton. Experimentally the frequency rather than the angular frequency is measured and it is simpler to use a single proportionality constant between the splitting and the magnetic field, so we define

$$G = \frac{g\mu_B}{2\pi} \tag{5.21}$$

The four level system will have four distinct optical transitions, from one of the optical ground state levels to one of the optical excited state levels (Figure 5.4). The frequencies for each of these transitions are given by

$$f_1 = f_0 + \frac{-G_g - G_e}{2} B \tag{5.22a}$$

$$f_2 = f_0 + \frac{-G_g + G_e}{2} B \tag{5.22b}$$

$$f_3 = f_0 + \frac{-G_g + G_e}{2} B \tag{5.22c}$$

$$f_4 = f_0 + \frac{+G_g + G_e}{2} B \tag{5.22d}$$

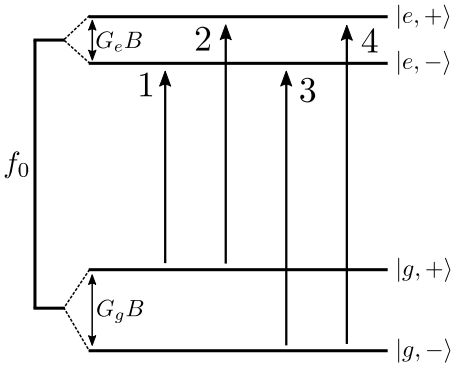

(a) Energy level diagram with optical transitions.

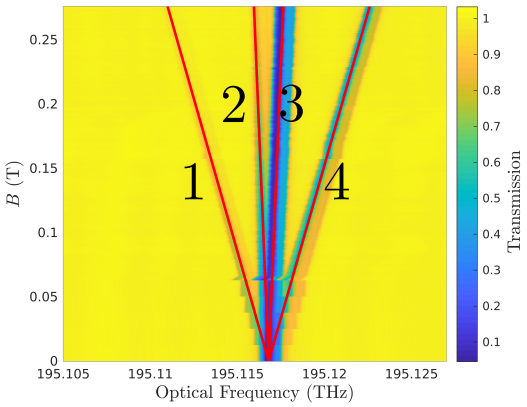

(b) Optical transmission spectrum with applied magnetic field.

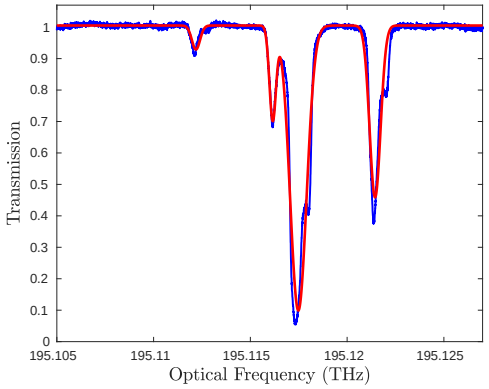

(c) Optical transmission spectrum at $B = 0.22\,\mathrm{T}$ (blue), with the fit to the four Gaussians (Equation 5.23) (red).

Figure 5.4: (a) Diagram showing the four energy levels, with the zero field optical frequency f_0, and the ground and excited state microwave Zeeman splitting G_gB and G_eB. The four optical transitions are labelled 1-4 in order of increasing frequency. (b) The experimentally measured optical transmission spectrum of Er:YSO as a function of the applied magnetic field. The absorption peaks labelled 1-4 correspond to the transitions labelled in (a). The red lines are the central frequencies for each of these transitions, given by Equations 5.22. (c) The optical transmission spectrum for $B = 0.22\,\mathrm{T}$, with fit to the Gaussian profile. The Gaussian fit is well matched to the general structure but doesn't entirely describe the finer details of the optical spectrum.

We can see in Figure 5.4 that as the magnetic field is increased the four transitions separate. For each value of the magnetic field the optical transmission spectrum was fitted a function of four Gaussians each with their centre given by Equations 5.22,

$$T = C_0 - \sum_{i=1}^{4} C_i \exp\left(-\frac{(f - f_i)^2}{2\sigma_i^2}\right) \tag{5.23}$$

This fit will also give us information about the inhomogeneous broadening of the optical transitions. From this fit we are able to find values for G_g, G_e and the zero-field optical frequency f_0,

$$f_0 = 195.1168\,\text{THz} \tag{5.24}$$
$$G_g = 24.085\,\text{GHz/T} \tag{5.25}$$
$$G_e = 17.976\,\text{GHz/T} \tag{5.26}$$

When using the ground state microwave transition we can use G_g to find how the microwave transition frequency changes as a function of the magnetic field. This microwave transition is inhomogeneously broadened, and so this frequency will correspond to the centre of the inhomogeneous distribution. The detuning between the microwave cavity and the centre of the microwave inhomogeneous line is given by

$$\mu_\mu = 2\pi G_g B - \omega_{c\mu} \tag{5.27}$$

Likewise, when using the excited state microwave transition G_e will be used to model how the microwave transition splits with magnetic field.

For the atomic scheme using the ground state microwave transition, the pump laser will be driving a transition starting from the upper level of the electronic ground state into one of the excited electronic levels. Depending on which transition we drive, the detuning of the centre of the optical inhomogeneous line from the optical cavity is given by

$$\mu_o = 2\pi f_i - \omega_o \tag{5.28}$$
$$= 2\pi f_i - \omega_\mu - \omega_\Omega \tag{5.29}$$

where f_i is the frequency of the optical transition from the excited electronic state, to the lower electronic ground state which will emit our upconverted photon. Due to conservation of energy the frequency of the upconverted photon is determined by the frequency of the input microwaves and the pump laser.

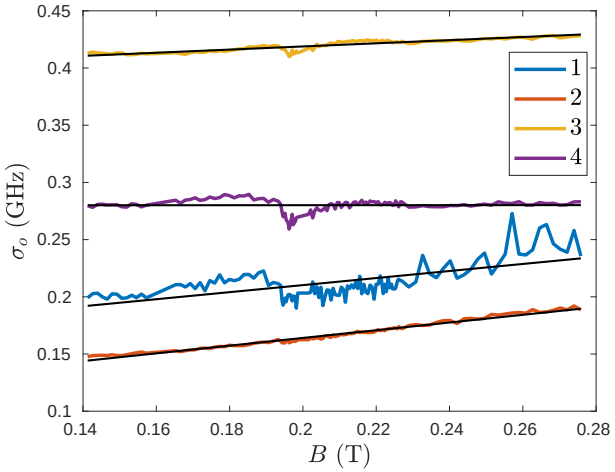

Figure 5.5: The standard deviation of the inhomogeneous broadening distributions for the four optical transitions shown in Figure 5.4a as a function of the applied magnetic field B. The black lines are linear fits.

5.2.4 Inhomogeneous Broadening

The inhomogeneous broadening for both the optical and microwave transitions will depend on the specific crystal of Er:YSO. Generally the inhomogeneous distribution is Gaussian, however in the crystal we are using this is not strictly true. Each of the main four absorption peaks corresponding to the four optical transitions have additional structure making them not exactly Gaussian, as can been seen in Figure 5.4c. This may be due to a small inclusion in the crystal, which could affect the transition frequencies for some of the atoms on top of the standard inhomogeneous distribution. However for this work we will make the approximation that the inhomogeneous broadening is Gaussian. The fit of Equation 5.23 to the optical spectrum (Figure 5.4b) allows us to see how the inhomogeneous broadening of the optical transitions change with magnetic field. This fit will give us the standard deviation of each of the absorption peaks, which describes the width of the inhomogeneous distribution.

The standard deviations for each transition show some magnetic field dependence as shown in Figure 5.5. This is because there is some inhomogeneity in the g-factors of the individual atoms. As the magnetic field is increased, the difference between the transition frequencies will also increase, which will lead to a larger inhomogeneous linewidth.

The standard deviations for each transition for a given magnetic field B

are,

$$\sigma_1 = 0.1486\,\mathrm{GHz} + B \cdot 0.3082\,\mathrm{GHz/T} \tag{5.30a}$$
$$\sigma_2 = 0.0966\,\mathrm{GHz} + B \cdot 0.3368\,\mathrm{GHz/T} \tag{5.30b}$$
$$\sigma_3 = 0.3914\,\mathrm{GHz} + B \cdot 0.1374\,\mathrm{GHz/T} \tag{5.30c}$$
$$\sigma_4 = 0.2799\,\mathrm{GHz} + B \cdot 0.0009\,\mathrm{GHz/T} \tag{5.30d}$$

The inhomogeneous broadening for the microwave transition was found by fitting a Gaussian to the microwave spectrum for when the atoms were far detuned from the cavity. The width of the inhomogeneous line was found to be

$$\sigma_\mu \approx 2\pi \cdot 3\,\mathrm{MHz} \tag{5.31}$$

5.2.5 Coupling Constants

The coupling constants g_o and g_μ describe how strong the coupling is between the optical and microwave fields to the transitions. For the simulations the coupling constants are [46]

$$g_\mu = 1.04\,\mathrm{Hz} \tag{5.32}$$
$$g_o = 51.9\,\mathrm{Hz} \tag{5.33}$$

5.2.6 Number of Atoms

In the experiment it is estimated that there are 6×10^{16} Er atoms in the doped crystal and about 0.8 of these are in the microwave mode of the resonator so the total number of atoms in the microwave mode is

$$N = 4.8 \times 10^{16}$$

A much smaller fraction of these are in the optical beam path,

$$N_o = 2.2 \times 10^{15}$$

5.2.7 Light Fields

Input Microwave Field

We want to find the input microwave field, b_{in}, as a function of the input power, P_μ. P_μ is the rate of energy going into the cavity from the microwave source. The energy for a single microwave photon is $\hbar\omega_\mu$, and the rate of incoming photons to the cavity is $|b_{in}|^2$, so the microwave input power is

$$P_\mu = |b_{in}|^2 \hbar\omega_\mu \tag{5.34}$$

and so we can define b_{in}, up to an arbitrary phase factor, as

$$b_{in} = \sqrt{\frac{P_\mu}{\hbar\omega_\mu}} \tag{5.35}$$

If there was an input optical field driving the $|1\rangle \rightarrow |3\rangle$ transition it would be calculated in the same way,

$$a_{in} = \sqrt{\frac{P_o}{\hbar\omega_o}} \tag{5.36}$$

Optical Pump Rabi Frequency

The Rabi Frequency for the transition $|2\rangle \rightarrow |3\rangle$ driven by an electric field is given by

$$\Omega = \frac{\mathbf{d}_{23} \cdot \mathbf{E}}{\hbar} \tag{5.37}$$

where $\mathbf{d}_{23}$ is the electric dipole moment for the transition, and $\mathbf{E}$ is the electric field. We assume the light is parallel with the dipole transition being driven, so $\mathbf{d}_{23} \cdot \mathbf{E} = d_{23} \cdot E$. We want to now find the electric field of the pump laser as a function of the pump laser power, P_Ω. The intensity of light is the power per unit area and can also be found from the electric field [68],

$$I = \frac{P}{A} = \frac{|E|^2}{2\mu_0 c} \tag{5.38}$$

So the electric field magnitude is

$$E = \sqrt{2\mu_0 c P_\Omega / A} \tag{5.39}$$

Where A is the area of the pump laser beam, and can be expressed in terms of the beam diameter D, $A = \pi D^2/4$.

5.2.8 Optical Pump Frequency

The frequency of the optical pump laser can be tuned by adjusting the temperature of the laser, which will change the length of the laser cavity and thus the laser's wavelength. For these experiments the pump frequency is set to,

$$\omega_\Omega / 2\pi = 195.117\,\mathrm{THz} \tag{5.40}$$

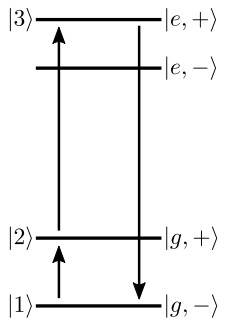

Figure 5.6: Diagram showing the energy levels used for the ground state experiments.

5.3 Results when Using the Ground State Spin Transition

We will begin with the scheme using the ground state spin transition, which is characterised by the parameters above. In this system the input microwave field will drive the lower microwave transition, $|g,-\rangle \rightarrow |g,+\rangle$, the optical pump will drive the transition from $|g,+\rangle$ to $|e,+\rangle$, and the atom decaying from the upper spin excited state to the ground state of the atom will emit our optical upconverted photon (Figure 5.6). The $|1\rangle$ level for the conversion process corresponds to $|g,-\rangle$, $|2\rangle$ corresponds to $|g,+\rangle$, and $|3\rangle$ is $|e,+\rangle$.

5.3.1 Microwave Spectrum

We can solve Equation 5.4 numerically as described in Section 4.1, as a function of both the detuning of the input microwave field from the cavity, δ_μ, and also the applied magnetic field, B. The applied magnetic field affects several properties of the atoms, but the main effect is how it changes the frequencies of the microwave (Equations 5.19) and optical (Equations 5.22) transitions. The change of the microwave transition frequency will modify how temperature effects the dissipation; from Equation 5.18, a larger microwave splitting will mean there are fewer photons in the thermal bath that can excite the transition.

The experimental and simulated microwave cavity transmission spectra are compared in Figure 5.7, and show good agreement. The transmission peaks follow a distinct avoided crossing due to interactions between the atoms and the cavity. There is a dark line of close to zero transmission running through the avoided crossing.

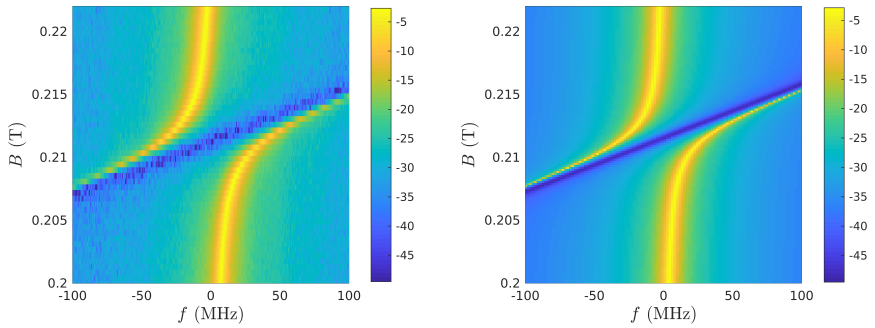

Figure 5.7: Comparison of the simulated microwave cavity transmission spectrum with the experimental data in dB. The avoided crossing is clearly seen. When cavity resonance is far from the atomic transition frequency there is little interaction between the atoms and cavity and so the spectrum is similar to an empty cavity. When the atoms are tuned close to the cavity resonance, the transmission peak is split due to the coupling between the atoms and the cavity field. There is a line of no transmission (below the thermal noise background) which corresponds to driving the atoms directly, these atoms will absorb the light and then some of this energy will be lost to incoherent processes which will cause a drop in transmission.

Avoided Crossing

We can understand the avoided crossing that we see in the microwave transmission spectrum in terms of dressed states of atoms and cavity. Using a highly simplified model, we can consider a system with many identical two level atoms in a microwave cavity. The Hamiltonian for this system can be written as the standard Tavis-Cummings Hamiltonian[1] [69, 70]

$$\hat{H} = \omega_{c\mu}\hat{b}^\dagger\hat{b} + g\hat{b}\sigma_{21} + g^*\hat{b}^\dagger\sigma_{12} + \omega_{12}\sigma_{22} \tag{5.41}$$

Where g is the effective coupling between all the atoms and the cavity field. This is an extension of the Jaynes-Cummings Hamiltonian which considers a single atom interacting with a cavity field [71].

This can be expressed in matrix form, using the basis of an excitation in the cavity and the atom in the ground state, and the ground state of the cavity and the atom in the excited state,

$$\begin{bmatrix} |\text{Excited Cavity}\rangle \\ |\text{Excited Atom}\rangle \end{bmatrix} \tag{5.42}$$

In this basis our Hamiltonian is

$$\hat{H} = \begin{bmatrix} \omega_{c\mu} & g^* \\ g & \omega_{12} \end{bmatrix} \tag{5.43}$$

[1] This is also known as the Dicke model.

The dressed states of the atom-cavity system will correspond to the eigenstates of this Hamiltonian, the eigenvalues corresponding to these eigenstates are

$$\omega_{\pm} = \frac{\omega_{c\mu} + \omega_{12}}{2} \pm \sqrt{\frac{(\omega_{c\mu} - \omega_{12})^2}{4} + |g|^2} \tag{5.44}$$

The transmission peaks in Figure 5.7 correspond to driving the system with input microwave frequencies given by Equation 5.44. The effective coupling strength g can be found from the individual atom coupling strength g_μ and the number of atoms N,

$$g = \sqrt{N} g_\mu \tag{5.45}$$

This is one of the reasons why it is necessary to consider the atoms both in and out of the optical beam path, because if we only considered the atoms in the beam path then the effective coupling g would be far smaller.

Dark State

The diagonal dark line in the microwave spectrum means that along this line there is effectively no transmission through the cavity. This is seen in both the experimental and simulated data, and is below the level of transmission for when the fields are detuned from both the atoms and the cavity. This dark line corresponds to exciting the ω_+ and ω_- dressed states equally (Equation 5.44). These dressed states can be thought of as partially exciting the atomic mode, and partially exciting the cavity mode. For this dark line when we are exciting the two dresses states, the cavity fraction of these two states are π out of phase and so will cancel out leading to no transmission through the cavity. The dark line occurs when there is an input microwave frequency of

$$\omega_\mu = \omega_{12}(B) = 2\pi G_g B \tag{5.46}$$

Where G_g is the constant of proportionality between the Zeeman splitting frequency and the magnetic field (Equation 5.25)

5.4 Upconverted Optical Signal

Experimentally the upconverted optical photons are detected using Raman-Heterodyne. The optical output photons and the pump laser photons will have a frequency difference of the microwave input frequency, $\omega_o - \omega_\Omega = \omega_\mu$. This allows one to detect the unconverted signal by combining it with the pump laser and measuring the beat frequency using an optical detector [72].

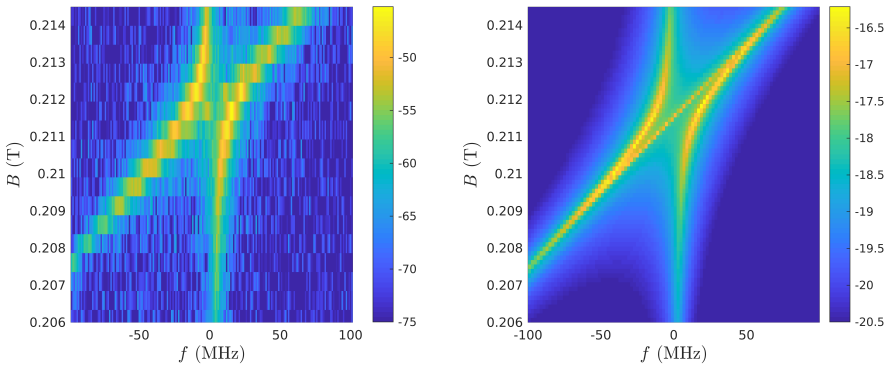

Figure 5.8: The experimental and simulated Raman-Heterodyne signal for low microwave power (−47.9 dBm) into the cavity, the temperature was determined from the size of the splitting to be 670 mK.

The upconverted optical signal for low microwave power is shown in Figure 5.8

For this experiment the crystal was being warmed by pump laser as well as microwave noise, and the temperature sensor was not directly measuring the temperature of the crystal. This meant that the experimental temperature recording was not accurate. The recorded temperature was around 160 mK, while from the simulations we can see that 670 mK is more accurate.

The experimental data is not very high resolution, and so it was difficult to tell if the bright line through the middle of the crossing in the Raman-Heterodyne signal was real or just noise. This line appears in the simulations and so we can be more confident that it is a real phenomenon.

One of the factors influencing the number of optical output photons is the magnitude of the intra cavity microwave field; if there are less microwave photons in the cavity then less can be converted into optical photons. For this reason the optical output field will generally be greatest where the microwave transmission is greatest, because this corresponds to a greater intra cavity microwave field. So when measuring the optical output field as a function of the input microwave detuning and the magnetic field, the conversion efficiency peaks will follow the same avoided crossing as the microwave transmission. As well as following the avoided crossing, upconversion is greater when the atoms are closer to resonance with the microwave fields. So although in Figure 5.7 the microwave field is large when the atoms are detuned from the cavity (for example at magnetic field strength of 0.2 T), not many photons are exciting the atoms to the $|2\rangle$ level, so the upconversion process is not very efficient. This is why in Figure 5.8 the conversion efficiency is greatest around 0.212 T because this is closer to resonance with the atoms.

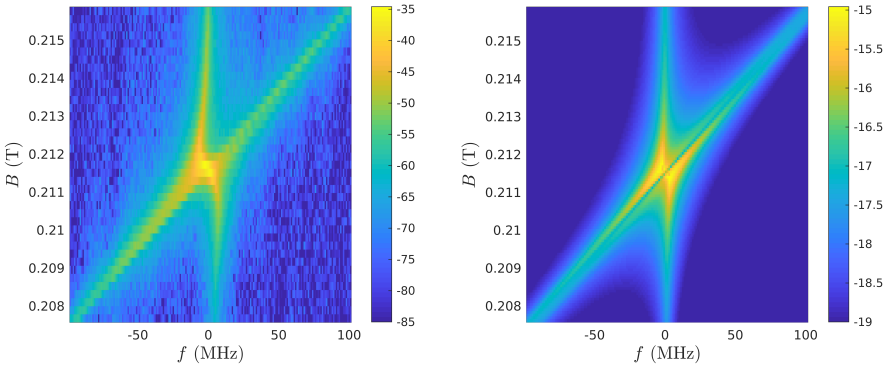

Figure 5.9: Experimental and theoretical Raman Heterodyne spectra for higher microwave power (−35.9 dBm) and temperature (1670 mK). The temperature was not recorded accurately from the experiment and so was estimated from the size of the splitting.

The effective size of the coupling between the atoms and the cavity can be approximated by Equation 5.45, however the effective number of atoms will change depending on the population of the atomic energy levels,

$$N = N_{total} \times (\rho_{11} - \rho_{22}) \tag{5.47}$$

where ρ_{11} and ρ_{22} represent the average occupation of the $|1\rangle$ and $|2\rangle$ states for the atoms in the ensemble. This is because the dressed states, which lead to the avoided crossing, depend on driving the $|1\rangle \rightarrow |2\rangle$ transition. When all the atoms are in the ground state they will all contribute to the total coupling and so $N = N_{total}$. However when some of the atoms are in an excited state this decreases the population in the ground state, which will reduce the coupling. Additionally, if atoms are in the $|2\rangle$ state, microwaves can also drive them into the ground state $|2\rangle \rightarrow |1\rangle$, which is the reverse process to absorbing photons, so atoms in the $|2\rangle$ state will further reduce the effective number of atoms.

Both temperature and the microwave field can drive atoms into the $|2\rangle$ state. So for high temperature and microwave field, the effective number of atoms in the ground state will be reduced which will reduce the total coupling and thus reduce the size of the cavity splitting. This can be seen in Figure 5.9 where the temperature and the microwave power are much higher and the size of the cavity splitting is so reduced that the two lobes of the avoided crossing touch and are no longer 'avoided'. The effect of temperature and microwave power will be further investigated in Section 7.3.

For Figure 5.9 we can't have too much certainty about the temperature that we estimate from the simulations. The transition is entirely saturated

by a combination of the microwave field and the temperature so it is hard to estimate the size of the splitting. Additionally, there could be error in the value for the microwave power that was recorded or the physical damping rates may be different from what we used for the simulation. Using these alternative parameters for simulations would lead us to choose a different temperature to fit the experiment.

The model that we have developed shows excellent agreement with the experimental spectra. Our simulations are based on the parameters described in Section 5.2. We are adjusting the temperature in the simulations such that they fit the experiments because the temperature was not accurately recorded. This will give us a much better idea of the actual temperature for the experiments.

5.5 Excited State Spin Transition Results

When using the excited state microwave transition, the optical pump laser was used to drive the atoms from one of the Zeeman levels of the electonic ground state, to the lower Zeeman level of the excited state $|e,-\rangle$. The input microwave photons can then further excite the atom into the upper Zeeman level $|e,+\rangle$; the atom then decays back to the original ground state, emitting an upconverted optical photon (Figure 5.10).

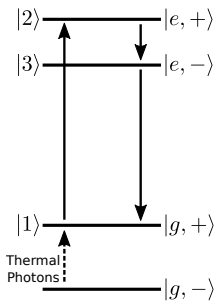

Figure 5.10: Diagram showing the energy levels used for the excited state experiments. Thermal photons excite the ground state Zeeman transition, the atom is then pumped to $|e,+\rangle$, the input microwaves will then drive the atom to $|e,-\rangle$, which will then emit an optical output photon and return to $|g,+\rangle$.

For the excited state experiments the pump laser drives the transition from $|g,+\rangle$ to $|e,+\rangle$. For this to take place, the atoms must already be excited by thermal photons into this state. From the Boltzmann distribution, the fraction of atoms in upper Zeeman level of the electronic ground state $n_{|g,+\rangle}$ will depend on the temperature of the atoms, and also the splitting of the

electronic ground state,

$$n_{|g,+\rangle} = \frac{1}{\exp\left(\hbar\omega_g/k_BT\right)+1} \tag{5.48}$$

Because the transition is driven by thermal photons, there is no coherence between the $|g,-\rangle$ and $|g,+\rangle$ states, this allows us to treat the atoms as three level systems, and the effective number of atoms becomes the number of atoms in the $|g,+\rangle$ state,

$$N_{\text{effective}} = n_{|g,+\rangle} N_{\text{total}} \tag{5.49}$$

Once the atoms have been driven by the pump laser to $|e,+\rangle$, the input microwave photons will drive this transition *down*, to $|e,-\rangle$ via stimulated emission. In the atomic rotating frame, the frequencies of the fields and the atomic energy levels don't matter directly; rather the phenomena depend on the *detunings* between the fields and the energy levels. For this reason the three level model and simulations will still apply to this system, but level $|2\rangle$ will correspond to $|e,+\rangle$, which is at a higher energy than $|e,-\rangle$ which is our $|3\rangle$. Additionally, the optical output photon will have frequency equal to the difference between the two inputs rather than the sum,

$$\omega_o = \omega_\Omega - \omega_\mu \tag{5.50}$$

For the experiments probing the system using the excited state microwave transition, the cavity was different to the cavity used for the ground state microwave transition experiments. The magnetic field was also aligned differently relative to the crystal so the Zeeman splitting will be different. The coupling between the microwave transition and the input microwaves is also different because the magnetic dipole moment for the microwave transition is different in the excited state. The different parameters for the excited state experiments are

Parameter	Value
G_g	20.917 GHz/T
G_e	20.287 GHz/T
$\omega_{c\mu}$	4733 MHz
$\gamma_{\mu c}$	1.24 MHz
$\gamma_{\mu i}$	0.94 MHz
g_μ	0.29 Hz [2]

[2] g_μ is different because the coupling proportional to the transition's magnetic dipole moment [73], which is smaller for the excited state transition.

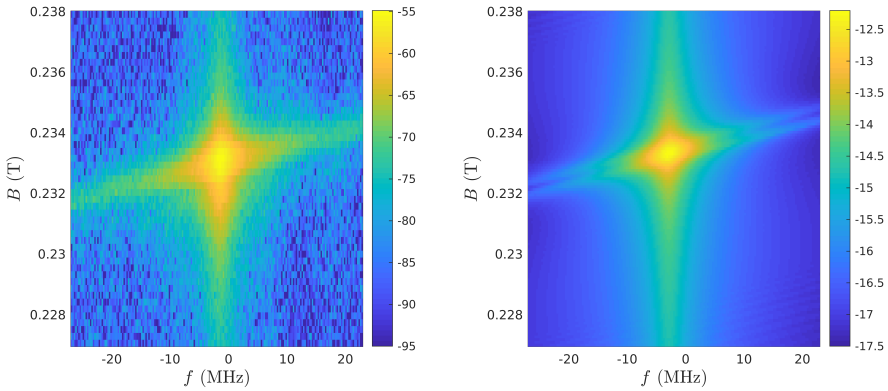

Figure 5.11: Experimental and simulated Raman Heterodyne spectra for the atomic scheme using the excited state microwave transition, with −31 dBm of microwave power into the cavity, at 150 mK.

For this system we will not observe an avoided crossing, this is because the microwaves will only interact with the atoms which have been pumped into the excited state. This means that the effective coupling between the microwave photons and the $|2\rangle \rightarrow |3\rangle$ transition will be too small to cause the cavity resonance to split. The conversion efficiency is largest where the intra cavity microwave field is large, near the cavity resonance, and where the input microwave photons are close to resonance with the microwave $|2\rangle \rightarrow |3\rangle$ transition, as shown in Figure 5.11. Both the experimental and simulated spectra show a crossing, with a vertical line corresponding to the cavity resonance and hence larger microwave field, and a diagonal line corresponding to the input light close to resonant with the microwave transition. The conversion efficiency is largest when the microwaves are resonant with both the cavity and the atomic transition, which corresponds to the centre of the crossing. From the simulations (Figure 5.12) we can see that the microwave cavity transmission spectrum appears identical to the spectrum when there is no interaction with the atoms.

In this chapter we have compared simulations with experiments for an single pass optical set up. These simulations were based on few fitted parameters showed good agreement with the experimental data. This allows us to be reasonably confident for our model to accurately simulate other experiments, such as the double cavity experiments. We will later use this model to show interesting phenomena in these experiments, and it will be helpful for finding ways to maximise conversion efficiency.

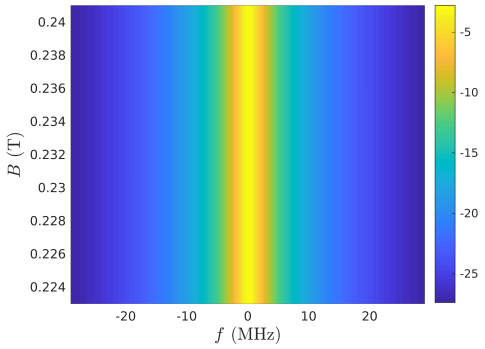

Figure 5.12: Microwave cavity transmission spectrum for the atomic scheme using the excited state microwave transition, for the same simulation as Figure 5.11. This looks identical to the transmission through the cavity when there is no interaction with the atoms.

Chapter 6

Linear Approximation

Currently we have not been making any assumptions about our cavity amplitudes, this has the advantage of being able to see non-linear effects for large field amplitudes. However the large field amplitudes make the integrals over the atomic coherences harder to solve. These atomic terms will depend non-linearly on the field amplitudes which means we have to solve our input-output equations numerically, and we can't derive a general formula for our conversion efficiencies and cavity transmission.

However, if our cavity fields are small, we can assume that effects due to the product of field amplitudes are negligible. This will make our input-output equations linear in the cavity fields, and so can be solved algebraically rather than numerically. The field amplitudes used in quantum computing applications are very small, and so this linear approximation is expected to be very accurate for this regime.

This can be thought of as a middle ground between the original work for the double cavity upconversion device [51], which relied on the adiabatic approximation and the full model we developed in previous chapters. The adiabatic model assumes that there was never any excited state population in the atoms and required the fields were always far detuned from the atoms, while the full field model doesn't make any assumptions about the fields or atoms. This model doesn't make assumptions about the detunings, but does require the fields to be very small.

6.1 Density Matrix Perturbation

To make the linear approximation we will use a perturbation method to solve for the steady state density matrix. For this method we are linearising with respect to the cavity fields and their complex conjugates: $a, \overline{a}, b, \overline{b}$. These are

treated purely as classical fields, and are all independent variables. For this approximation it is *not* assumed that the pump laser power is small.

Without approximation $\mathcal{L}$ can be separated into terms which separately depend linearly on these variables, $\mathcal{L}$ has no higher order dependence on the cavity fields,

$$\mathcal{L} = \mathcal{L}_0 + a\mathcal{L}_a + \overline{a}\mathcal{L}_{\overline{a}} + b\mathcal{L}_b + \overline{b}\mathcal{L}_{\overline{b}} \tag{6.1}$$

Here $\mathcal{L}_0$ is the Liouvillian in the undriven case, with both $a = 0,\ b = 0$, but still with the optical pump laser driving the atoms, $\Omega \neq 0$. Now we make the approximation that ρ only depends linearly on the cavity fields

$$\rho \approx \rho_0 + a\rho_a + \overline{a}\rho_{\overline{a}} + b\rho_b + \overline{b}\rho_b \tag{6.2}$$

Likewise, ρ_0 corresponds to the undriven case, this won't simply have all population in the ground state because of the effects of temperature and the pump laser. Thermal photons can drive the atoms into the $|2\rangle$ state, and the pump laser can further excite them into $|3\rangle$ while also generating coherence between the $|2\rangle$ and $|3\rangle$ states (when using the excited state spin transition coherence is generated between $|1\rangle$ and $|2\rangle$). This means that we must treat ρ_0 as a full 3×3 matrix rather than a scalar or diagonal matrix. We now want to find the steady state density matrix using $\dot{\rho} = \mathcal{L}\rho = 0$,

$$\mathcal{L}\rho = (\mathcal{L}_0 + a\mathcal{L}_a + \overline{a}\mathcal{L}_{\overline{a}} + b\mathcal{L}_b + \overline{b}\mathcal{L}_{\overline{b}})(\rho_0 + a\rho_a + \overline{a}\rho_{\overline{a}} + b\rho_b + \overline{b}\rho_b) \tag{6.3}$$

$$= \mathcal{L}_0\rho_0 + \mathcal{L}_0(a\rho_a + \overline{a}\rho_{\overline{a}} + b\rho_b + \overline{b}\rho_b) + (a\mathcal{L}_a + \overline{a}\mathcal{L}_{\overline{a}} + b\mathcal{L}_b + \overline{b}\mathcal{L}_{\overline{b}})\rho_0 \tag{6.4}$$

$$+ (a\mathcal{L}_a + \overline{a}\mathcal{L}_{\overline{a}} + b\mathcal{L}_b + \overline{b}\mathcal{L}_{\overline{b}})(a\rho_a + \overline{a}\rho_{\overline{a}} + b\rho_b + \overline{b}\rho_b) \tag{6.5}$$

We know that $\mathcal{L}_0\rho_0 = 0$ because this simply is the Master Equation for the undriven case at steady state. Because we are looking for a linear equation we assume terms that are the product of two fields are negligible, and so can ignore the final line (Equation 6.5). With this, our steady state linearised Master equation becomes

$$\mathcal{L}\rho = \mathcal{L}_0(a\rho_a + \overline{a}\rho_{\overline{a}} + b\rho_b + \overline{b}\rho_b) + (a\mathcal{L}_a + \overline{a}\mathcal{L}_{\overline{a}} + b\mathcal{L}_b + \overline{b}\mathcal{L}_{\overline{b}})\rho_0 \tag{6.6}$$

$$\begin{aligned} &= a(\mathcal{L}_0\rho_a + \mathcal{L}_a\rho_0) + \overline{a}(\mathcal{L}_0\rho_{\overline{a}} + \mathcal{L}_{\overline{a}}\rho_0) \\ &\quad + b(\mathcal{L}_0\rho_b + \mathcal{L}_b\rho_0) + \overline{b}(\mathcal{L}_0\rho_{\overline{b}} + \mathcal{L}_{\overline{b}}\rho_0) \\ &= 0 \end{aligned} \tag{6.7}$$

Because each of $a, \overline{a}, b, \overline{b}$ are treated as independent variables we can say that each of the terms proportional to these must individually be zero, $\mathcal{L}_0\rho_x + \mathcal{L}_x\rho_0 = 0$, for $x = a, \overline{a}, b, \overline{b}$, and so we can solve for each ρ_x:

$$\rho_x = -\mathcal{L}_0^{-1}\mathcal{L}_x\rho_0 \tag{6.8}$$

where

$$\rho_0 = \mathcal{L}_0^{-1}0_{\mathbb{1}} \tag{6.9}$$

6.2 Numerical Calculations

For finding these first order terms numerically we use a very similar method to the full simulations. We will transform $\mathcal{L}$ and ρ to be purely real, a and b are complex variables so rather than work with these and their complex conjugates, a and b will be split into their real and imaginary parts, $a = a_r + ia_i$, $b = b_r + ib_i$. To do this we use the transformation matrix C (Equation 4.8) from Section 4.2, which was used for the full Liouvillian matrix. C transforms a complex Hermitian matrix into a real, non-symmetric matrix without losing any information. We use C to transform our Liouvillian matrix and the density matrix (in vector form) to be entirely real.

$$\begin{aligned}
\mathcal{L}_{real} &= C\mathcal{L}C^{-1} && \text{(6.10a)}\\
&= C(\mathcal{L}_0 + a_r\mathcal{L}_{ar} + a_i\mathcal{L}_{ai} + b_r\mathcal{L}_{br} + b_i\mathcal{L}_{bi})C^{-1} && \text{(6.10b)}\\
&= C\mathcal{L}_0C^{-1} + a_rC\mathcal{L}_{ar}C^{-1} + a_iC\mathcal{L}_{ai}C^{-1} + b_rC\mathcal{L}_{br}C^{-1} + b_iC\mathcal{L}_{bi}C^{-1} && \text{(6.10c)}\\
&= \mathcal{L}_{0,real} + a_r\mathcal{L}_{ar,real} + a_i\mathcal{L}_{ai,real} + b_r\mathcal{L}_{br,real} + b_i\mathcal{L}_{bi,real} && \text{(6.10d)}
\end{aligned}$$

$$\begin{aligned}
\rho_{real} &= C\rho && \text{(6.11a)}\\
&\approx C\rho_0 + a_rC\rho_{ar} + a_iC\rho_{ai} + b_rC\rho_{br} + b_iC\rho_{bi} && \text{(6.11b)}\\
&= \rho_{0,real} + a_r\rho_{ar,real} + a_i\rho_{ai,real} + b_r\rho_{br,real} + b_i\rho_{bi,real} && \text{(6.11c)}
\end{aligned}$$

The equivalent equations to Equations 6.8 and 6.9 still hold,

$$\begin{aligned}
\rho_{x,real} &= -C\mathcal{L}_0^{-1}\mathcal{L}_x\rho_0\\
&= -C\mathcal{L}_0^{-1}C^{-1}C\mathcal{L}_xC^{-1}C\rho_0 && \text{(6.12)}\\
&= -\mathcal{L}_{0,real}^{-1}\mathcal{L}_{x,real}\rho_{0,real}\\
\rho_{0,real} &= -C\mathcal{L}_0^{-1}0_{\mathbb{1}}\\
&= -C\mathcal{L}_0^{-1}C^{-1}C0_{\mathbb{1}} && \text{(6.13)}\\
&= -\mathcal{L}_{0,real}^{-1}0_{\mathbb{1}}
\end{aligned}$$

So to find each of the density matrix terms, we first calculate $\rho_{0,real}$ with Equation 6.13 which can then be used to find all of the linear terms. Then we solve for the real linear terms, $\rho_{x,real}$ for $x = a_r, a_i, b_r, b_i$, using Equation 6.12 and transform back to find the complex density matrix terms, ρ_x. Finally we need to convert from using the real and imaginary parts a_r, a_i, b_r, b_i to the

fields and their complex conjugates $a, \overline{a}, b, \overline{b}$,

$$\begin{aligned}\rho &\approx \rho_0 + a_r\rho_{ar} + a_i\rho_{ai} + b_r\rho_{br} + b_r\rho_{bi} \\ &= \rho_0 + \frac{1}{2}(a+\overline{a})\rho_{ar} + \frac{i}{2}(-a+\overline{a})\rho_{ai} + \frac{1}{2}(b+\overline{b})\rho_{br} + \frac{i}{2}(-b+\overline{b})\rho_{bi} \\ &= \rho_0 + a\frac{\rho_{ar} - i\rho_{ai}}{2} + \overline{a}\frac{\rho_{ar} + i\rho_{ai}}{2} + b\frac{\rho_{br} - i\rho_{bi}}{2} + \overline{b}\frac{\rho_{br} + i\rho_{bi}}{2}\end{aligned} \tag{6.14}$$

and so we have

$$\rho_a = \frac{\rho_{ar} - i\rho_{ai}}{2} \tag{6.15a}$$

$$\rho_{\overline{a}} = \frac{\rho_{ar} + i\rho_{ai}}{2} \tag{6.15b}$$

$$\rho_b = \frac{\rho_{br} - i\rho_{bi}}{2} \tag{6.15c}$$

$$\rho_{\overline{b}} = \frac{\rho_{br} + i\rho_{bi}}{2} \tag{6.15d}$$

These linear terms, Equations 6.15, do not depend on the input fields, but they will vary based on things such as the temperature, the pump laser power, and the atomic detunings.

6.2.1 Density Matrix Elements

The elements of the density matrices are visualised in Figure 6.1 for the scheme using the ground state microwave transition, and Figure 6.2 for the scheme using the excited state microwave transition. ρ_0 is the only term with non-zero diagonal elements, this means that the other terms cannot affect the population of the energy levels and hence the linear model will not account for the effect of saturation by the fields. The linear model will however still show the effect of thermal photons exciting the spin transition. The other non-zero elements of ρ_0 correspond to the transition being driven by the pump laser, in the ground state these are the $(2,3)$ and $(3,2)$ elements, and the $(1,2)$ and $(2,1)$ elements for the excited state. This gives a very helpful check, because for ρ_0 the $(1,3)$ element is always zero, and so there will be no optical output photons generated when there is just the optical pump; all of the optical output photons arise from microwave input photons.

For each of the first order terms (not ρ_0), there are only two non-zero elements. When using the ground state microwave transition ρ_a and ρ_b have non-zero elements corresponding to the atomic transition operators for the $|1\rangle \rightarrow |2\rangle$ and $|1\rangle \rightarrow |3\rangle$ transitions. The density matrices for $\overline{a}$ and $\overline{b}$ are the Hermitian conjugates of the density matrices for a and b respectively,

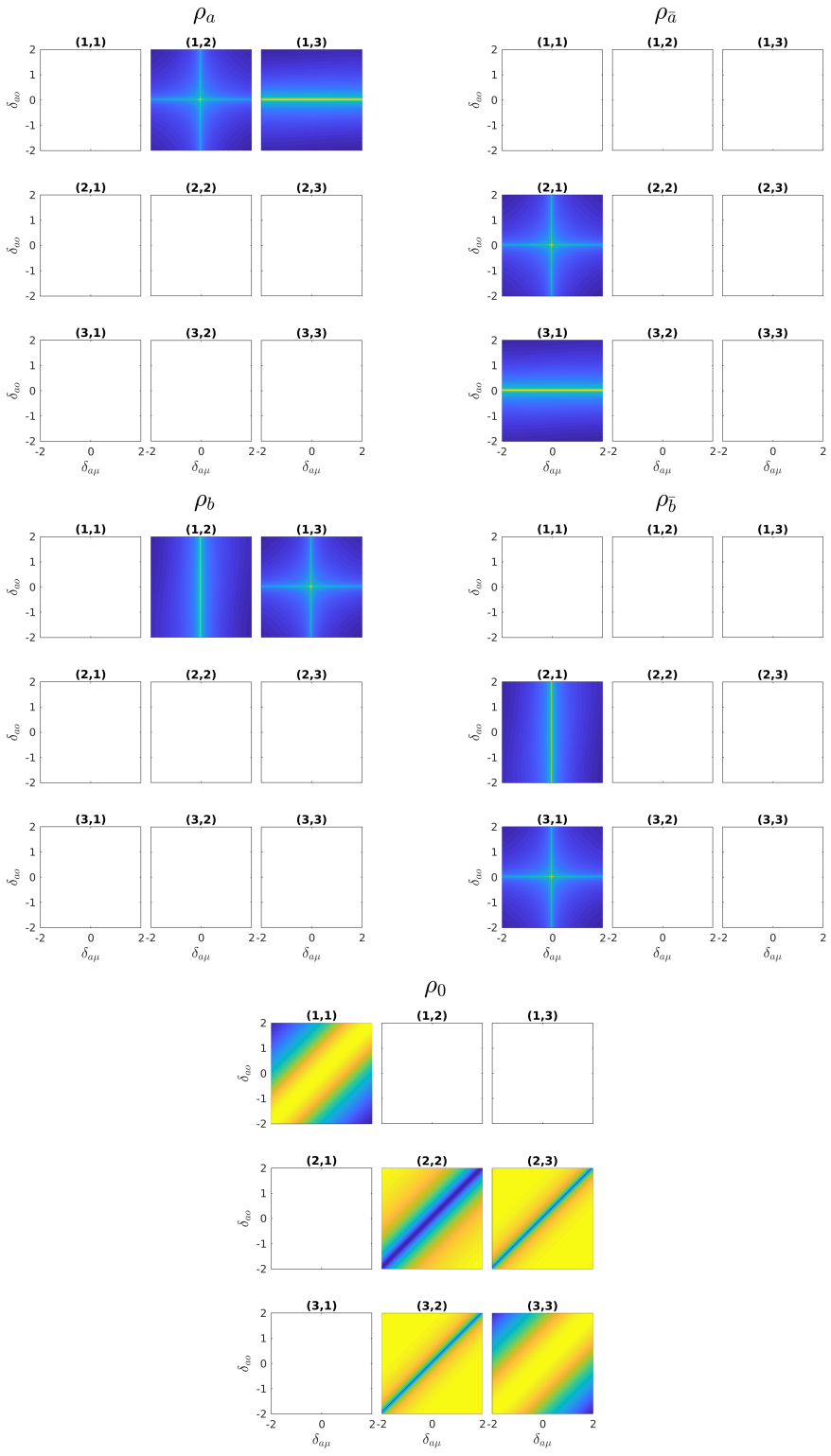

Figure 6.1: The elements of the ρ_a, ρ_b, $\rho_{\overline{a}}$, $\rho_{\overline{b}}$ and ρ_0 as a function of the atomic detunings in MHz when using the ground state microwave transition. The blank plots indicate that the element is always zero.

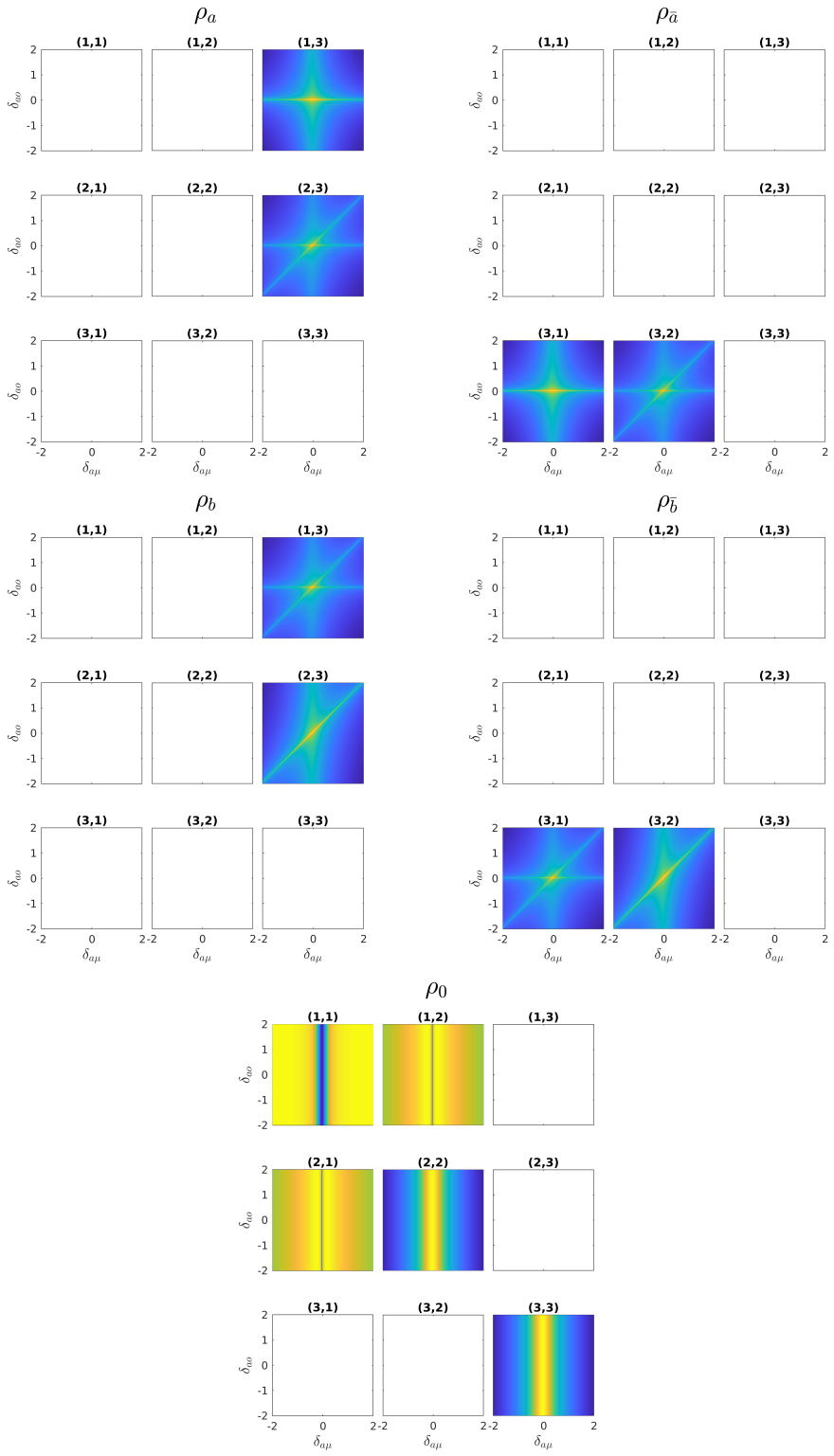

Figure 6.2: The elements of the ρ_a, ρ_b, $\rho_{\overline{a}}$, $\rho_{\overline{b}}$ and ρ_0 as a function of the atomic detunings in MHz when using the excited state microwave transition. The blank plots indicate that the element is always zero.

and have non-zero elements corresponding to the $|2\rangle \rightarrow |1\rangle$ and $|3\rangle \rightarrow |1\rangle$ transitions. Equivalently, when using the excited state microwave transition ρ_a and ρ_b only have non-zero elements corresponding to the $|2\rangle \rightarrow |3\rangle$ and $|1\rangle \rightarrow |3\rangle$ transitions.

Because of this, when calculating the linearised forms of S_{13} and S_{12} (S_{23} for the excited state), they will only contain terms from ρ_a and ρ_b. S_{13} is expressed as

$$\begin{aligned} S_{13} &= g_o \sum_k \sigma_{13,k} \\ &\approx g_o \sum_k a\rho_{a,13,k} + b\rho_{b,13,k} \\ &= a g_o \sum_k \rho_{a,13,k} + b g_o \sum_k \rho_{b,13,k} \\ &= a S_{a,13} + b S_{b,13} \end{aligned} \tag{6.16}$$

and likewise for S_{12} and S_{23},

$$S_{12} \approx a S_{a,12} + b S_{b,12} \tag{6.17}$$

$$S_{23} \approx a S_{a,23} + b S_{b,23} \tag{6.18}$$

For these equations the sum terms are approximated as integrals and evaluated using the same methods as the full field case (Section 4.4).

6.3 Conversion Efficiency and Cavity Transmission

We can now write our input-output equations in terms that only depend linearly on the cavity fields, and do not depend on the complex conjugates of the fields.

$$-i\delta_o a = -i(a S_{a,13} + b S_{b,13}) - \frac{2\gamma_{oc} + \gamma_{oi}}{2} a + \sqrt{\gamma_{oc}} a_{in} \tag{6.19}$$

$$-i\delta_\mu b = -i(a S_{a,12} + b S_{b,12}) - \frac{2\gamma_{\mu c} + \gamma_{\mu i}}{2} b + \sqrt{\gamma_{\mu c}} b_{in} \tag{6.20}$$

Because these equations are linear they can be solved without the need for numerical methods like iterative root finding as used for the full field case. The equations can be expressed in matrix form,

$$\begin{bmatrix} \sqrt{\gamma_{oc}} a_{in} \\ \sqrt{\gamma_{\mu c}} b_{in} \end{bmatrix} = \begin{bmatrix} i S_{a,13} - i\delta_o + \frac{2\gamma_{oc}+\gamma_{oi}}{2} & i S_{b,13} \\ i S_{a,12} & i S_{b,12} - i\delta_\mu + \frac{2\gamma_{\mu c}+\gamma_{\mu i}}{2} \end{bmatrix} \begin{bmatrix} a \\ b \end{bmatrix} \tag{6.21}$$

By inverting the 2×2 matrix, and using the field boundary conditions (Equations 2.13)) we can linearly express our output fields in terms of the input fields,

$$a_{out} = C_{aa} a_{in} + C_{ab} b_{in} \tag{6.22}$$

$$b_{out} = C_{ba} a_{in} + C_{bb} b_{in} \tag{6.23}$$

Where

$$C_{aa} = \frac{\gamma_{oc}\left(iS_{b,12} - i\delta_\mu + \frac{2\gamma_{\mu c}+\gamma_{\mu i}}{2}\right)}{S_{a,12}S_{b,13} + \left(iS_{a,13} - i\delta_o + \frac{2\gamma_{oc}+\gamma_{oi}}{2}\right)\left(iS_{b,12} - i\delta_\mu + \frac{2\gamma_{\mu c}+\gamma_{\mu i}}{2}\right)} \tag{6.24}$$

$$C_{ab} = -\frac{iS_{b,13}\sqrt{\gamma_{\mu c}\gamma_{oc}}}{S_{a,12}S_{b,13} + \left(iS_{a,13} - i\delta_o + \frac{2\gamma_{oc}+\gamma_{oi}}{2}\right)\left(iS_{b,12} - i\delta_\mu + \frac{2\gamma_{\mu c}+\gamma_{\mu i}}{2}\right)} \tag{6.25}$$

$$C_{ba} = -\frac{iS_{a,12}\sqrt{\gamma_{\mu c}\gamma_{oc}}}{S_{a,12}S_{b,13} + \left(iS_{a,13} - i\delta_o + \frac{2\gamma_{oc}+\gamma_{oi}}{2}\right)\left(iS_{b,12} - i\delta_\mu + \frac{2\gamma_{\mu c}+\gamma_{\mu i}}{2}\right)} \tag{6.26}$$

$$C_{bb} = \frac{\gamma_{\mu c}\left(iS_{a,13} - i\delta_o + \frac{2\gamma_{oc}+\gamma_{oi}}{2}\right)}{S_{a,12}S_{b,13} + \left(iS_{a,13} - i\delta_o + \frac{2\gamma_{oc}+\gamma_{oi}}{2}\right)\left(iS_{b,12} - i\delta_\mu + \frac{2\gamma_{\mu c}+\gamma_{\mu i}}{2}\right)} \tag{6.27}$$

Here C_{aa} and C_{bb} represent transmission through the optical and microwave cavities; the number of output photons per input photon for each cavity is given by

$$\left|\frac{a_{out}}{a_{in}}\right|^2 = |C_{aa}|^2 \tag{6.28}$$

$$\left|\frac{b_{out}}{b_{in}}\right|^2 = |C_{bb}|^2 \tag{6.29}$$

C_{ab} and C_{ba} represent the conversion of microwave photons to optical photons and the reverse process of optical photons to microwave photons. The conversion efficiencies are given by

$$\left|\frac{a_{out}}{b_{in}}\right|^2 = |C_{ab}|^2 \tag{6.30}$$

$$\left|\frac{b_{out}}{a_{in}}\right|^2 = |C_{ba}|^2 \tag{6.31}$$

As a check, we can see that when there are no atoms, and we set all the atomic terms to zero, that there is no conversion, and the transmission terms are simply the results for empty cavities.

Using Equation 6.25, the conversion efficiency from microwave photons into optical photons is given by

$$|C_{ab}|^2 = \left| \frac{S_{b,13}\sqrt{\gamma_{\mu c}\gamma_{oc}}}{S_{a,12}S_{b,13} + \left(iS_{a,13} - i\delta_o + \frac{2\gamma_{oc}+\gamma_{oi}}{2}\right)\left(iS_{b,12} - i\delta_\mu + \frac{2\gamma_{\mu c}+\gamma_{\mu i}}{2}\right)} \right|^2 \tag{6.32}$$

So to find the conversion efficiency using our linear model we do not need to use an iterative solver, the process for finding the conversion efficiency is shown in Figure 6.3. To solve Equation 6.32 we will solve for the atomic ensemble terms using numerical integration without using an iterative method. The results from these calculations can simply be substituted into Equation 6.32 to give us our conversion efficiency.

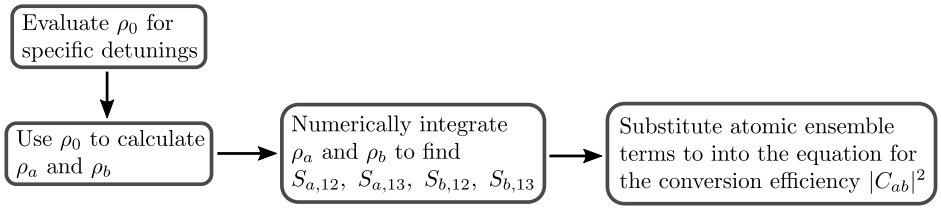

Figure 6.3: Diagram showing the process of calculating the conversion efficiency with the linear approximation without using an iterative method.

6.4 Higher order terms

We can find the higher order terms for ρ that depend on the products of the classical fields by extending our perturbation method. For the second order terms, which will depend on the product of two field amplitudes,

$$\rho = \rho_0 + \sum_{x=a,\bar{a},b,\bar{b}} x\rho_x + \sum_{x=a,\bar{a},b,\bar{b}} \sum_{y=a,\bar{a},b,\bar{b}} xy\rho_{xy}\left(\frac{\delta_{x,y}+1}{2}\right) \tag{6.33}$$

The factor of $\frac{\delta_{x,y}+1}{2}$ is to avoid double counting any terms, because we are treating the fields classically $xy = yx$. $\mathcal{L}$ still only depends linearly on the fields,

$$\mathcal{L} = \mathcal{L}_0 + \sum_{x=a,\bar{a},b,\bar{b}} x\mathcal{L}_x \tag{6.34}$$

Like before we are solving the Master Equation for steady state, we can expand the Master Equation as,

$$\mathcal{L}\rho = \mathcal{L}_0\rho_0 + \sum_{x=a,\overline{a},b,\overline{b}} x(\mathcal{L}_x\rho_0 + \mathcal{L}_0\rho_x) + \sum_{x=a,\overline{a},b,\overline{b}}\sum_{y=a,\overline{a},b,\overline{b}} xy\left(\mathcal{L}_x\rho_y + \mathcal{L}_y\rho_x + \mathcal{L}_0\rho_{xy}\left(\frac{\delta_{x,y}+1}{2}\right)\right) + \text{Third Order Terms} \tag{6.35}$$

The first line has the undriven and linear terms, the second line has the second order terms, and we neglect the third order terms. In steady state each of these terms will be zeros, so for the second order terms we can write,

$$\mathcal{L}_x\rho_y + \mathcal{L}_y\rho_x + \mathcal{L}_0\rho_{xy} = 0, \tag{6.36}$$

We have already found forms for the first order terms, ρ_x, and so we can use these to solve for ρ_{xy},

$$\begin{aligned}\mathcal{L}_0\rho_{xy} &= -\mathcal{L}_x\rho_y - \mathcal{L}_y\rho_x \\ &= \mathcal{L}_x\mathcal{L}_0^{-1}\mathcal{L}_y\rho_0 + \mathcal{L}_y\mathcal{L}_0^{-1}\mathcal{L}_x\rho_0 \qquad (6.37)\\ \rho_{xy} &= (\mathcal{L}_0^{-1}\mathcal{L}_x\mathcal{L}_0^{-1}\mathcal{L}_y + \mathcal{L}_0^{-1}\mathcal{L}_y\mathcal{L}_0^{-1}\mathcal{L}_x)\rho_0 \qquad (6.38)\end{aligned}$$

Higher order terms will also be given by a superoperator acting on ρ_0. The superoperator will be the sum of all permutations of $\mathcal{L}_0^{-1}\mathcal{L}_x$ multiplied together, and will have a negative sign for the odd order terms.

Previously we developed the unsimplified model of our upconversion process which doesn't make assumptions about the fields. This allows for nonlinear interactions between the fields and the atoms, which are important when the fields are large. However these nonlinear effects mean the cavity equations must be solved numerically, and we don't have a nice analytic form for the conversion efficiency. In this chapter we have developed a model which assumes there are only linear effects between the fields and atoms. Using this linear model we evaluate the integrals for our atomic ensemble terms numerically, and then use these terms to analytically solve for the cavity fields, and transmission and conversion efficiency.

In the next chapter we will explore phenomena that arises when using the full unsimplified model, and then compare this unsimplified model with the linear model we have developed in this chapter.

Chapter 7

Simulating the Double Cavity Upconversion Process

We have developed a numerical model in Chapter 4 for the experiments where there is an ensemble of inhomogeneously broadened atoms, interacting with the cavity fields of both a microwave and an optical cavity, and also driven by an optical pump laser (Figure 7.1). The results presented in Chapter 5 modelled a modification of this experiment where there was no optical cavity. This section covers the results for the system with both cavities, and also looks at the effects of various parameters. At the end of this chapter we will compare this model which doesn't make assumptions about the size of the cavity fields with simplified model from the original work in [51] and the linear model from Chapter 6.

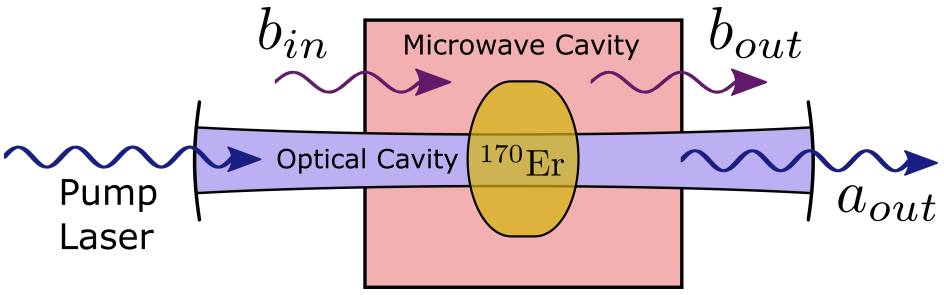

Figure 7.1: Diagram showing the double cavity experimental setup. b_{in} and b_{out} are the microwave input and output fields for the microwave cavity, and a_{out} is the upconverted optical output field from the optical cavity.

7.1 Double Cavity Simulations

7.1.1 Optical Cavity Parameters

For these simulations we will be using the same parameters as described in Section 5.2 unless specified otherwise. We also need the parameters that characterise the optical cavity, and to take into account how this effects the pump laser Rabi frequency. The parameters for the optical cavity are taken from previous experiments using the double cavity set up [46]. In these experiments the values for the optical coupling loss γ_{oc}, and intrinsic loss γ_{oi} were

$$\gamma_{oc} = 2\pi \times 1.7\,\mathrm{MHz} \tag{7.1}$$

$$\gamma_{oi} = 2\pi \times 8.0\,\mathrm{MHz} \tag{7.2}$$

Experimentally, cavities can be designed to have different coupling losses. For example, in a Fabry–Pérot cavity the coupling loss depends on the reflectivity of the partially reflective mirrors, for a whispering-gallery mode cavity the coupling loss can be adjusted by changing the distance between the resonator and the coupling prism. Intrinsic loss decreases the conversion efficiency and so experimentally we want to design cavities with very small intrinsic loss. The intrinsic loss can be related to the intrinsic cavity quality factor Q_i by,

$$\gamma_{oi} = \frac{\omega_o}{Q_i} \tag{7.3}$$

Optical Pump Rabi Frequency

In this the double cavity system we are assuming that both the pump laser and optical signal photons are close to resonant with different modes of the optical Fabry–Pérot cavity. This means that the pump laser field and the optical signal field will be enhanced by the optical cavity. The Rabi frequency for the transition which the pump laser drives will be increased because the field from the pump laser will be greater.

The energy in an optical cavity can be written either in terms of the number of photons in the cavity, n_{cav}, or in terms of the cavity electric field

$$\text{Energy} = n_{cav}\hbar\omega \tag{7.4}$$

$$= \frac{\epsilon_0}{2}\int E^2 d^3x \tag{7.5}$$

Inside a cavity, the cavity field α is related to the input field α_{in} by [57],

$$\alpha = \frac{\sqrt{\gamma}_{oc}\alpha_{in}}{(2\gamma_{oc} + \gamma_{oi})/4 - i\delta} \tag{7.6}$$

where δ is the detuning between the field and the cavity. So on resonance, the number of photons inside the cavity n_{cav} is given by

$$n_{cav} = n_{in} \frac{\gamma_{oc}}{\left(\frac{2\gamma_{oc}+\gamma_{oi}}{2}\right)^2} \tag{7.7}$$

where $n_{cav} = |\alpha|^2$ and the flux of photons into the cavity is $n_{in} = |\alpha_{in}|^2$. The flux of photons into the cavity depends on the pump laser power P_Ω and the laser frequency,

$$n_{in} = \frac{P_\Omega}{\hbar\omega} \tag{7.8}$$

We can use Equations 7.4, 7.7 and 7.8 to express the energy in the cavity in terms of the input pump power,

$$\text{Energy} = P_\Omega \frac{\gamma_{oc}}{\left(\frac{2\gamma_{oc}+\gamma_{oi}}{2}\right)^2} \tag{7.9}$$

Making the assumption that the electric field magnitude is the same throughout the cavity, from Equation 7.5 we can express the energy in the cavity as $\frac{\epsilon_0}{2}E^2V$, where V is the volume of the optical cavity mode. This can be combined with Equation 7.9 for an expression for the electric field in terms of the laser power

$$E = \sqrt{\frac{2P_\Omega}{\epsilon_0 V}} \frac{\sqrt{\gamma_{oc}}}{(2\gamma_{oc} + \gamma_{oi})/2} \tag{7.10}$$

The Rabi frequency for a transition is related to the electric field by

$$\Omega = \frac{d \cdot E}{\hbar} \tag{7.11}$$

where d is the electric dipole moment for the transition. This allows us to express the Rabi frequency in terms of the input laser power,

$$\Omega = \frac{d}{\hbar}\sqrt{\frac{2P_\Omega}{\epsilon_0 V}} \frac{\sqrt{\gamma_{oc}}}{(2\gamma_{oc} + \gamma_{oi})/2} \tag{7.12}$$

7.1.2 Spectra using the Ground State Spin Transition

We will now simulate the double cavity experiments, in general these look quite similar to the single pass simulations we have already run, but we are able to calculate values for the conversion efficiency. The upconversion process was simulated using the ground state spin transition, as a function of the detuning between microwave field and the cavity, and the applied magnetic field (Figure 7.2). This simulation used the same parameters as the single

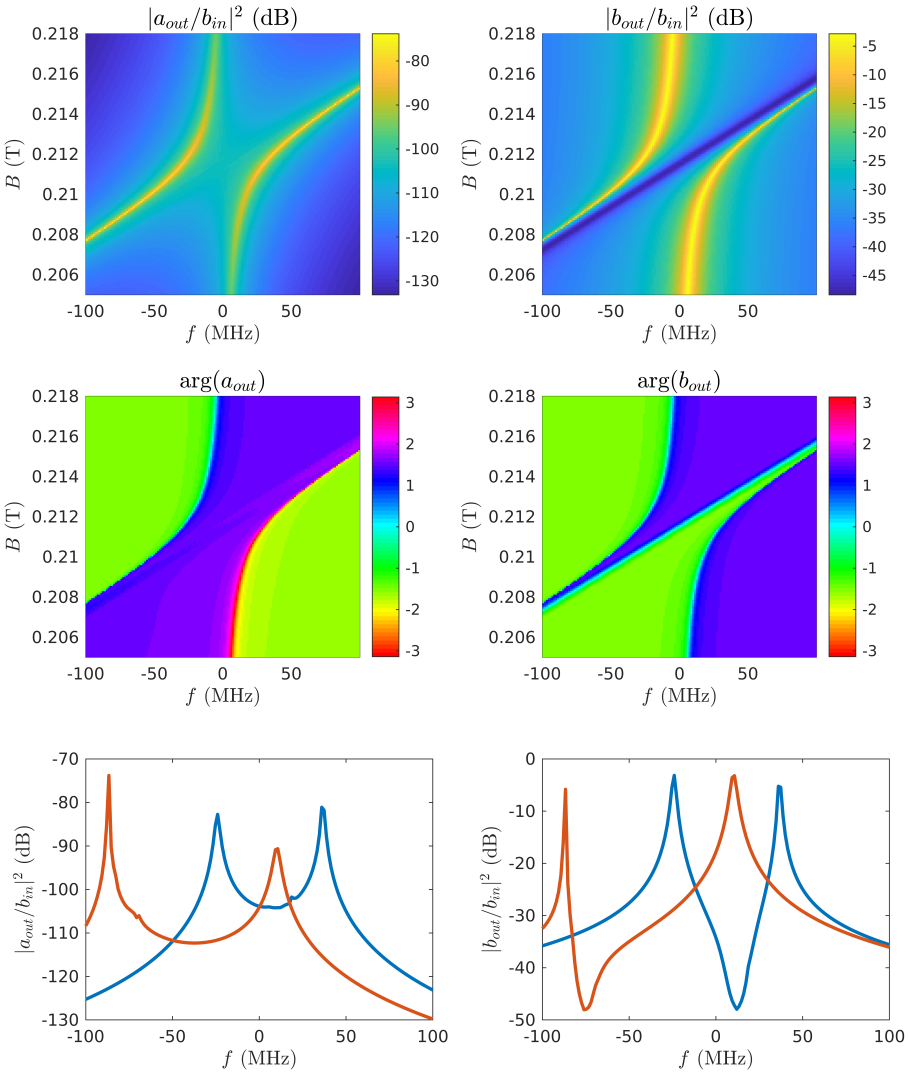

Figure 7.2: Results from simulations of the upconversion process using the ground state spin transition. The top row shows the conversion efficiency and microwave cavity transmission, as a function of the magnetic field B and the detuning between the input microwave field and the cavity f. The middle row shows the relative phase of the output microwave and optical fields, on the same axes as the top row. The bottom row shows the conversion efficiency and microwave transmission as functions of the detuning between the microwave field. The blue lines for the magnetic field of $B = 0.212\,\mathrm{T}$ which is where atoms are closest to resonant with the microwave cavity. The orange line is at $B = 0.208\,\mathrm{T}$, which corresponds to the maximum conversion efficiency of 4×10^{-8}.

pass simulations of the upconversion process using the ground state spin transition, as well as the additional optical cavity parameters.

For this simulation, the transition corresponding to the optical output is $|e,+\rangle \rightarrow |g,-\rangle$, the same as in the single pass experiments. The optical output field is resonant with the optical cavity, which has a frequency of $f = 195.122\,\mathrm{THz}$. The magnetic field affects the atomic optical transition frequency because it changes the Zeeman splitting of the ground and excited spin transitions,

$$\omega_{13} = 2\pi \left(f_0 + B\frac{G_g + G_e}{2} \right) \tag{7.13}$$

The frequency of the output optical photons is determined by the sum of the input microwave and optical pump frequencies,

$$\omega_o = \omega_\mu + \omega_\Omega \tag{7.14}$$

So therefore the detuning of the atomic transition from the optical cavity and input field is

$$\delta_{ao} = \omega_{13} - \omega_{co} \tag{7.15}$$

$$= 2\pi(f_0 + B\frac{G_g + G_e}{2}) - \omega_\mu - \omega_\Omega \tag{7.16}$$

The simulation was performed for a temperature of $T = 150\,\mathrm{mK}$ and input microwave power of $P_\mu = -60\,\mathrm{dBm}$, and optical pump power of $P_\Omega = 1.74\,\mathrm{mW}$.

For this simulation the maximum conversion efficiency is very low at around $\eta = 4 \times 10^{-8}$, this is because the detunings have not been modified to optimise for the conversion efficiency and the laser pump power is very low. The maximum conversion efficiency doesn't occur when the atoms are closest to resonance with the microwave cavity. This is because the largest intra cavity microwave field follows the dressed states of the atoms and the cavity, which leads to the avoided crossing. When the atoms are closest to resonance with the cavity (around $B = 0.212\,\mathrm{T}$ in Figure 7.2), the microwave field is largest when it is driving both the atoms and the cavity. The conversion efficiency is greater when the atoms are detuned from the cavity, so that when the microwave field is large it is driving the atoms much more than the cavity. However, being detuned from the cavity means that the intra cavity field becomes smaller. Consequentially, maximum conversion efficiency is found when the microwave frequency is close enough to resonance with the cavity such that the intra cavity field is large, but far enough detuned such that the field will drive the atoms more than the cavity.

This simulation is analogous to the experiment performed in [46], which has achieved the highest conversion efficiency using rare earth ion doped crystals to date. In this experiment, a crystal of YSO doped with erbium ions with natural isotropic ratios (as opposed to the pure ^{170}Er we are considering), was held in overlapping microwave and optical cavities and driven with an optical pump laser. This experiment was using the ground state spin transition for the upconversion process, the temperature was around 4 K and the pump laser power was 6.48 mW. The maximum conversion efficiency achieved was 1.26×10^{-5}, which is much higher than in Figure 7.2. This can be explained because in [46] the maximum conversion efficiency was achieved by scanning the microwave and optical pump frequencies to find the detunings which gave the highest conversion efficiency. For the simulation for Figure 7.2 we have fixed the optical pump frequency and so are not scanning it to find the maximum conversion efficiency. Additionally, the experiment in [46] used 3.7 times higher optical pump power to achieve the maximum conversion efficiency. The maximum conversion efficiency in Figure 7.2 is consistent with other values of conversion efficiency found in [46] for lower pump power and suboptimal detunings. In Chapter 8 we will discuss optimising the detunings for our simulations, and investigate the role of greater pump power.

7.1.3 Spectra using the Excited State Spin Transition

As with the simulations of the process using the ground state spin transition, we also simulated the process using the excited state spin transition (Figure 7.3). These used the same parameters as were used for the simulations of the single pass experiments for the upconversion process using the excited state spin transition (Section 5.5). For this simulation, the optical field is resonant with the optical cavity and the output photon corresponds to the $|e,+\rangle \rightarrow |g,-\rangle$ transition, which is the same as in the simulation using the ground state spin transition. So Equation 7.16 which defined the optical detuning when using the ground state spin transition will also apply when using the excited state spin transition. The simulation was performed for a temperature of $T = 150\,\text{mK}$, input microwave power of $P_\mu = -30\,\text{dBm}$ and optical pump power of $P_\Omega = 1.74\,\text{mW}$.

As expected, this looks very similar to the single pass results, with no avoided crossing and a maximum conversion efficiency where the atoms and microwave field are resonant with the microwave cavity. The conversion efficiency is similarly low to the ground state simulations at around 1.8×10^{-7}, again this is because the detunings haven't been modified to maximise the conversion efficiency and the optical pump power is small.

When using either the spin transition from either the ground or excited

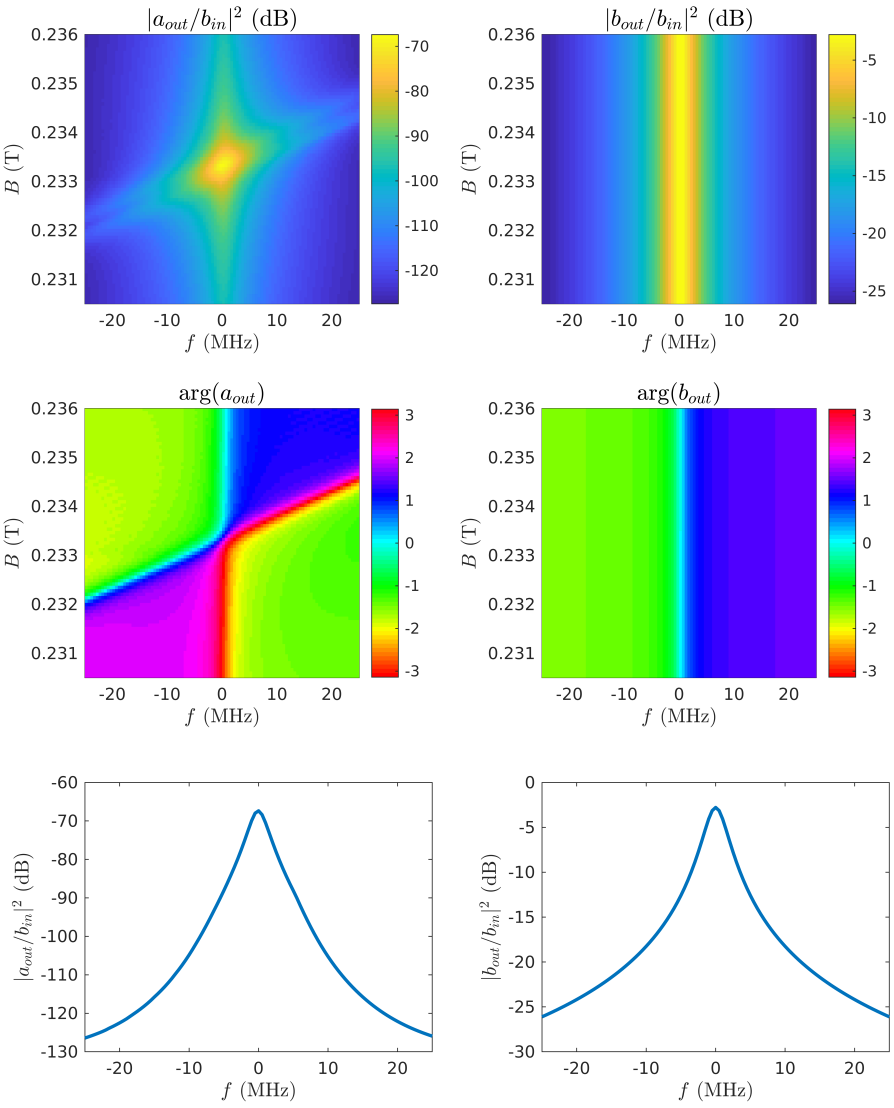

Figure 7.3: Results from simulations of the upconversion process using the excited state spin transition. The top row shows the conversion efficiency and microwave cavity transmission, as a function of the magnetic field B and the detuning between the input microwave field and the cavity f. The middle row shows the relative phase of the output microwave and optical fields, on the same axes as the top row. The bottom row shows the conversion efficiency and microwave transmission as functions of the detuning between the microwave field and the cavity close to where the atoms are close to resonant with the microwave cavity at $B = 0.233\,\mathrm{T}$. This corresponds to the maximum conversion efficiency of 1.8×10^{-7}.

electronic state, the upconverted output photons have a well defined relative phase, as we can see in Figures 7.2 and 7.3. This means that the phase information of our input photons is not destroyed, which is what we require for coherent upconversion.

7.2 Effect of Non-Optically Driven Atoms

In the single pass experiments and the double cavity simulations only a fraction of the atoms were in the optical pump beam path, while all the atoms were driven by the microwave field. This means that only a fraction of the atoms will contribute to the upconversion process. Only the atoms which are in the pump beam path will interact with the field of the optical output photons. The size of the splitting for the avoided crossing that we see when using the ground state spin transition will come from the total number of atoms in the sample because this arises from the interaction between the atoms and the intra cavity microwave field. So for a smaller total number of atoms the splitting will decrease. However, the atoms which are driven by the microwave field but not the optical fields, will reduce the conversion efficiency via *parasitic absorption*. This is an unwanted process where atoms absorb a photon and are driven to an excited state, but then this excitation is lost to a decoherence process and the atom decays back to a lower state. Because of dephasing and decoherence, the atom in the excited state may not coherently re-emit a photon, which means that the input photon cannot contribute to the upconversion process.

The effect of parasitic absorption is present both inside and outside of the optical pump beam. Inside the beam path both the input microwave photons and the upconverted optical photons may be absorbed by the atoms and then lost to decoherence. In the region with only microwave fields, some of the input microwave photons will be lost to parasitic absorption. For the double cavity system, we can reduce the effects of parasitic absorption inside the beam path by having the input fields off resonant with the atoms. This reduces the population in the excited states, which means there will be less unwanted loss from damping processes. In the current experiments and simulations there are ~ 20 times as many non-optically driven atoms as there are optically driven atoms, so the effect of parasitic absorption of microwave photons is likely to be much larger outside of the optical beam path. The effect of the parasitic absorption of microwave photons by atoms outside of the optical beam path can be minimised by using a crystal which only has small amount not optically driven (Figure 7.5).

When a smaller crystal is used, such that all the atoms are in the optical

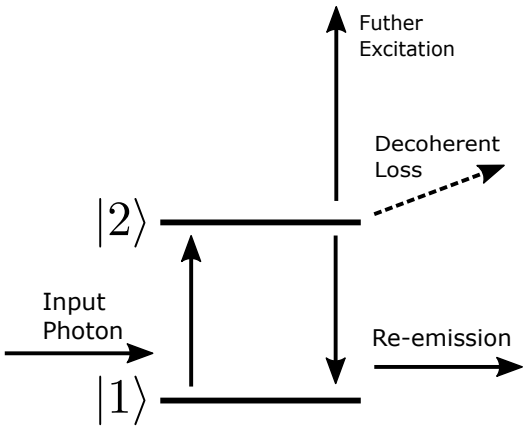

Figure 7.4: Diagram showing the different processes that may occur when an atom is excited by an input photon. The atom may be further excited into higher energy state, as happens in the upconversion process. It may decay back to the original state and re-emit the photon. The atom may also lose the excitation via decoherent loss which will decrease the conversion efficiency.

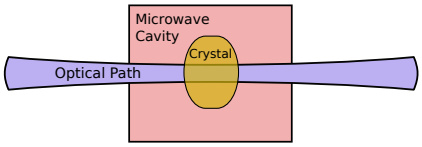

(a) Setup with a large amount of the crystal not optically driven.

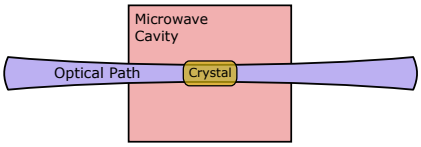

(b) Setup with the most of the crystal in the optical beam path.

Figure 7.5: The two set ups with and without a large fraction of the Er doped crystal not in the optical beam path. In the set up where the entire crystal is in the optical beam path there will be less parasitic absorption of the input microwaves and also the splitting of the microwave cavity mode will be smaller.

beam path, the splitting of the avoided crossing decreases, and the upconversion efficiency is increased, as shown in Figure 7.6. For these simulations there was a microwave power of $P_\mu = -60\,\mathrm{dBm}$, temperature of $T = 50\,\mathrm{mK}$ and the same detunings as 7.2. Both the simulations have 2.2×10^{15} atoms inside the optical beam path, and in the case where there is a large fraction of atoms outside of the optical beam path, the total number of atoms was 4.8×10^{16}. In this comparison, when there was a large fraction outside of the optical beam path the maximum conversion efficiency was $\eta = 2 \times 10^{-8}$, compared with a maximum conversion efficiency of $\eta = 3 \times 10^{-7}$ with no atoms outside of the optical beam path.

Theoretically, increasing the number of atoms inside the optical beam path would lead to higher conversion efficiency. However, practically, as the number of dopant ions in the crystal is increased, the inhomogeneous broadening will also increase, leading to a decrease in conversion efficiency.

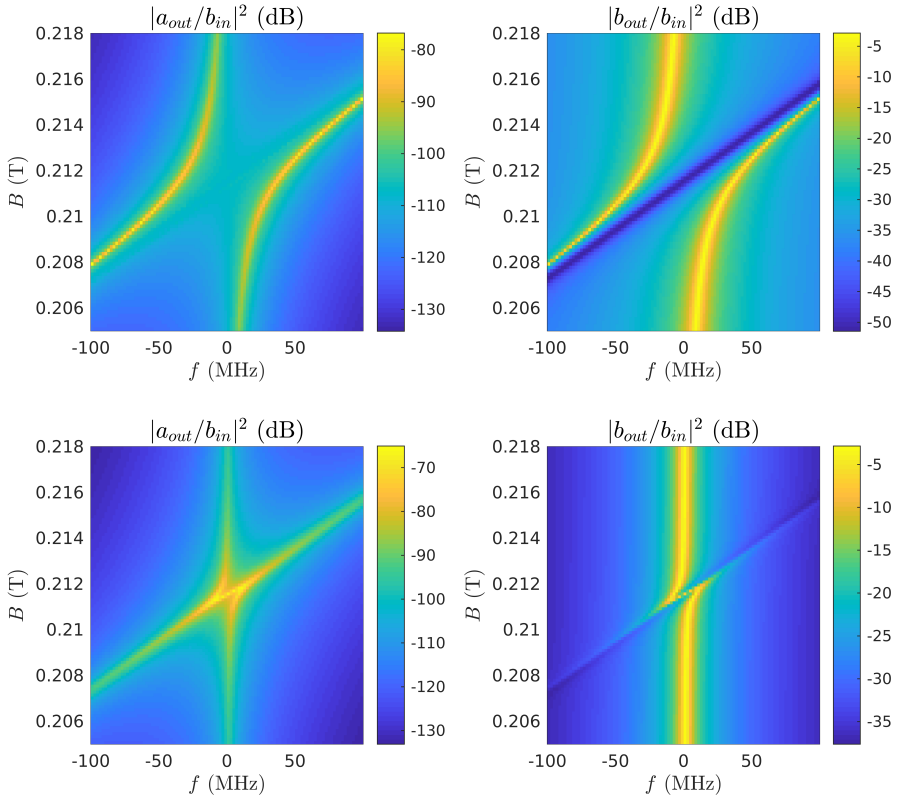

Figure 7.6: The conversion efficiency and microwave cavity transmission for the upconversion process using the ground state spin transition, demonstrating the effect of atoms outside of the optical beam path. The top row shows results for a simulation with a large fraction of the atoms outside the optical beam path, as there were in the single pass experiments. The bottom row shows results for the simulation with a smaller crystal such that all atoms were inside the optical beam path. For both cases, the same number of atoms are interacting with the optical fields.

7.3 Microwave Transition Saturation

When using the ground state spin transition the effects of higher temperature and input microwave power lead to saturation of the microwave transition. At zero temperature or microwave power all the atoms will be in the ground state $|1\rangle$, however as temperature increases the population of $|2\rangle$ will also increase, in accordance with the Boltzmann distribution. When an atom absorbs an input microwave photon, this will excite the atom from the ground state to $|2\rangle$, so as microwave power is increased this will excite more atoms into the microwave excited state. Microwave photons can also cause the decay from $|2\rangle$ to $|1\rangle$ via stimulated emission. For this reason the number of atoms is modified by a factor of the average population difference between the two levels, $\rho_{11} - \rho_{22}$.

We can explain these effects using a simplified system of a two level atom driven by a microwave field, and coupled to a thermal bath at finite temperature (Appendix A). At steady-state the population difference is,

$$\rho_{11} - \rho_{22} = \frac{\frac{\gamma^2}{2}(2n_{bath}+1)}{4|g_\mu b|^2 + \frac{\gamma^2}{2}(2n_{bath}+1)^2} \tag{7.17}$$

where $g_\mu b$ is the Rabi frequency for the transition driven by the microwaves, and n_{bath} is the number of photons in the thermal bath, given by the Planck distribution. If the microwave field is small enough that we can approximate $b = 0$ then the population difference will be due purely to the thermal effects and we retrieve the result expected from the Boltzmann distribution,

$$\rho_{11} - \rho_{22} = \frac{\exp\left(\hbar\omega/k_B T\right) - 1}{\exp\left(\hbar\omega/k_B T\right) + 1} \tag{7.18}$$

If b is large then more atoms will be driven into the $|2\rangle$ state and the population difference will decrease.

We can investigate the state of the atoms from the integrated density matrix,

$$\bar{\rho} = \int d\delta_{ao} d\delta_{a\mu} G_o(\delta_{ao}) G_\mu(\delta_{a\mu}) \rho(\delta_{ao}, \delta_{a\mu}) \tag{7.19}$$

We developed a method to find $\bar{\rho}$ in Section 4.4, because the (1,2) and (1,3) elements are used to calculate the atomic terms for our cavity field equations (Equations 4.1 and 4.2). The off diagonal elements of $\bar{\rho}$ tell us about the average coherence between energy levels of atoms in the ensemble. While the diagonal terms are the average occupation of the different atomic energy levels. Due to the inhomogeneous broadening, the single atom density matrix will be different for each atom. $\bar{\rho}$ gives information about the ensemble which

is more useful for looking at the effects on the cavity fields. As the microwave transition is saturated, either by thermal photons or input microwave photons, $\bar{\rho}_{11}$ will decrease and $\bar{\rho}_{22}$ will increase, as more atoms are excited from the $|1\rangle$ state to $|2\rangle$.

7.3.1 Thermal Saturation

From Figure 7.7 we can see that as the temperature is increased, the splitting decreases. This is because the effective number of atoms is reduced, which reduces the magnitude of the coupling between the ensemble of atoms and the cavity fields. These simulations were performed using the same optical detunings and number of atoms as Figure 7.2, input microwave power of -60 dBm, and 1.74 mW of laser pump power. The deceasing population difference can be seen directly in Figure 7.8, as the temperature is increased, $\bar{\rho}_{11}$ and $\bar{\rho}_{22}$ converge, and the effective number of atoms for the conversion process decreases.

7.3.2 Microwave Field Saturation

The effect of saturation by the input microwave field on the cavity spectrum is significantly different compared with the effect of temperature. For the temperature effects, all the atoms will experience the same temperature regardless of the input frequency. This is different for the saturation by the microwave field, because the intra cavity field amplitude depends on the input frequency. When the input frequency is far detuned from the cavity resonance there won't be significant saturation effects because the cavity amplitude will be small, even for large input amplitudes. When the input field is close to resonance with the cavity, the intra cavity field will be greatest, and when the fields are also close to resonance with the atoms, this is where we will see the saturation effects. Furthermore, the cavity fields are effected by the presence and states of the atoms; the atoms cause the cavity resonance to split, but then for large cavity amplitudes this will reduce the effective number of atoms and thus reduce the size of the cavity splitting. These effects are easiest to see for small numbers of atoms, in Figure 7.9 we are assuming there are no atoms outside of the optical beam path ($N_{total} = N_o = 2.2 \times 10^{15}$). As the microwave input power is increased, the splitting does decrease, but also a line of higher transmission and conversion appears in the middle of the splitting. In Figure 7.10 we can see the line in the middle of the splitting comes from saturating the microwave transition. For low microwave power we have the familiar dark line running down the middle of the avoided crossing in the microwave spectrum. The population difference for low power shows a

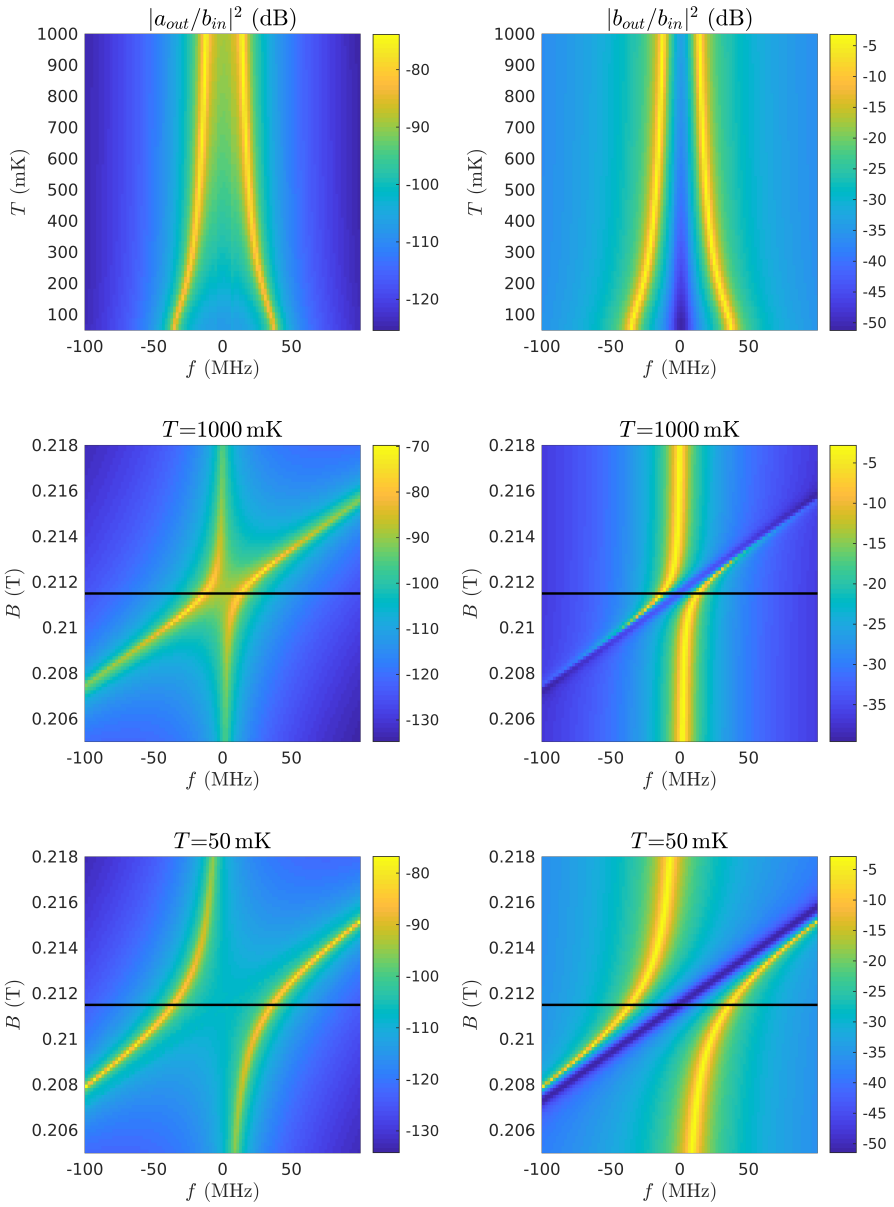

Figure 7.7: The photon number conversion efficiency and microwave cavity transmission (each in dB), demonstrating how the splitting reduces as the temperature increases. The top row has the conversion efficiency and microwave cavity transmission at a fixed magnetic field at different temperatures. The second row shows the full crossing at 1000 mK and the third row shows the crossings at 50 mK. The black lines indicate the value of the magnetic field for the temperature sweep, this magnetic field was chosen because it is where the atoms are resonant with the cavity and where we can most easily see the size of the splitting change.

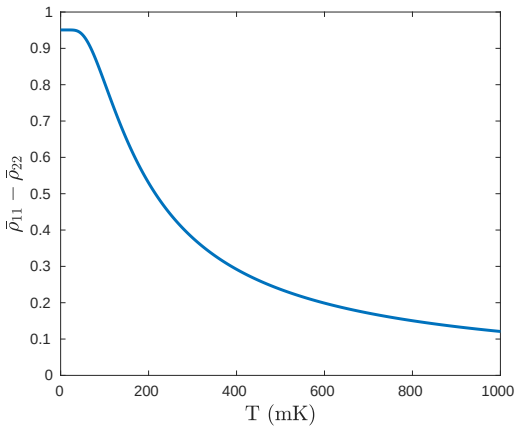

Figure 7.8: The population difference given by $\bar{\rho}_{11} - \bar{\rho}_{22}$, as a function of temperature. At zero temperature almost all the atoms are in the ground state and so the population difference is close to 1, this decreases with increasing temperature as more atoms are thermally excited into $|2\rangle$. At zero temperature, some atoms are in state $|2\rangle$ because of the driving microwave field.

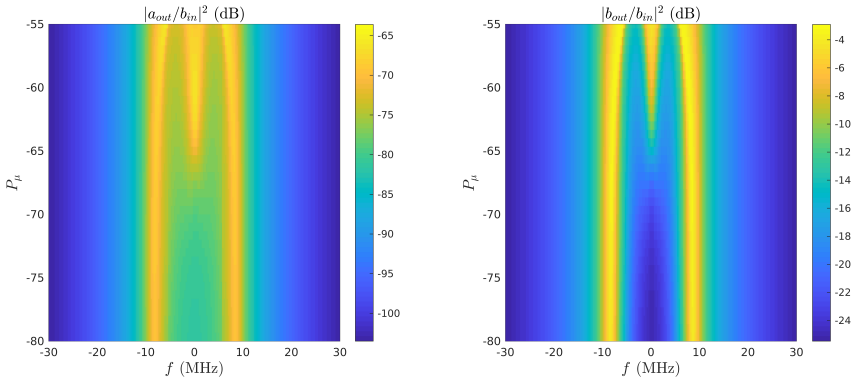

Figure 7.9: Photon number conversion efficiency and cavity transmission for increasing microwave power, showing the effect of saturation. As the power is turned up, the splitting slightly decreases, and a peak of transmission and conversion appears in the middle. These simulations were performed using the magnetic field of 0.2115 T, indicated by the black lines on Figure 7.10. These simulations were performed using a low temperature of $T = 50$ mK so we could easily see the effect of the microwave power, and the same laser pump power and detunings as Figure 7.2.

negligible fraction of atoms not in the ground state. When the power is turned up though, we can see that the atoms close to resonance become saturated, and the difference in population between the $|1\rangle$ and $|2\rangle$ states decreases. When the atoms are saturated they can no longer absorb microwave photons, and so this means that the light can pass right through the cavity causing a

peak in transmission. The conversion efficiency is also peaked here because there are lots of atoms in the $|2\rangle$ state so the pump laser can easily drive them into $|3\rangle$, which can then emit an upconverted optical photon.

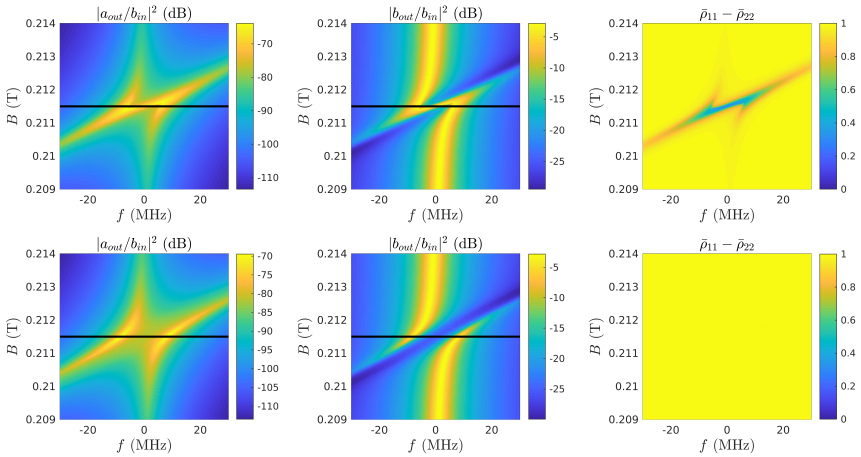

Figure 7.10: Conversion efficiency $|a_{out}/b_{in}|^2$, microwave cavity transmission $|a_{out}/b_{in}|^2$ and population difference $(\bar{\rho}_{11} - \bar{\rho}_{22})$. The top row is for high microwave power $P_\mu = -55\,\text{dBm}$, and the bottom row is for low microwave power $P_\mu = -80\,\text{dBm}$. The black horizontal lines are at $B = 0.2115\,\text{T}$, which is what was used for Figure 7.9.

7.4 Comparison of different models

7.4.1 Adiabatic Approximation Model

So far we have developed a model for the full system, as well as a simplified model assuming that the atoms were only linearly effected by the cavity fields. The original work for this three level upconversion system was done with the adiabatic approximation model [51]. The adiabatic approximation model assumes that the fields are far detuned from the atomic transitions, such that the population of either of the excited states can be neglected. Using the model, the conversion process happened via an off-resonant Raman process.

This was done by adiabatically eliminating the dynamics of the atoms in the cavity, and treating the atom-field interactions with a single constant parameter. The photon number conversion efficiency for this adiabatic approximation model is given by

$$\eta_{\text{adia}}(\delta_o, \delta_\mu) = \left| \frac{S\sqrt{\gamma_{oc}\gamma_{\mu c}}}{|S|^2 + (\frac{2\gamma_{oc}+\gamma_{oi}}{2} - i\delta_o)(\frac{2\gamma_{\mu c}+\gamma_{\mu i}}{2} - \delta_\mu)} \right|^2 \tag{7.20}$$

Here the atomic interactions are characterised by the parameter S,

$$S = \sum_k \frac{\Omega_k g_{\mu,k} g^*_{o,k}}{(\delta_{ao,k} - \delta_{o,k})(\delta_{a\mu,k} - \delta_{\mu,k})} \tag{7.21}$$

More discussion of S including how to calculate it numerically can be found in Appendix B. This model is only valid when the fields are far detuned from the inhomogeneous line of the transitions

$$|\omega_{12} - \omega_\mu| \gg \sigma_\mu \tag{7.22a}$$
$$|\omega_{13} - \omega_o| \gg \sigma_o \tag{7.22b}$$

Where ω_{12} and ω_{13} are the microwave and optical transition frequencies, and ω_μ and ω_o are the frequencies of the microwave and optical fields.

The adiabatic approximation model is expected to give significant disagreement with the full model when the fields are not sufficiently detuned, and the Equations 7.22 are not satisfied. When the fields are close to resonance with the atomic transitions the atoms will have a non-negligible population in the excited states, which violates the assumptions of the adiabatic approximation model.

7.4.2 Comparing Cavity Spectra

In Figure 7.11 the conversion efficiency is compared for the three different models. In this comparison the parameters were chosen such that the adiabatic approximation model was still mostly valid, the optical field is 300 GHz detuned from the atomic transition and 1 GHz detuned from the optical cavity, the microwave power is very low ($P_\mu = -200\,\text{dBm}$) and the temperature was low ($T = 50\,\text{mK}$). The simulations used 1×10^{16} atoms, with no atoms outside of the optical beam path. In this figure the conversion efficiency is shown as a function of the detuning between the input fields and the cavity δ_μ, and the detuning between the atoms and the cavity $\delta_{a\mu}$. The detuning between the atoms and the cavity really refers to the frequency difference between the centre of the inhomogeneous line and the cavity, and changing this detuning is equivalent to changing the applied magnetic field.

The three models are in good qualitative agreement for when fields are far detuned from the atoms, and when the cavity fields are small, there is also good quantitative agreement which we will later investigate with Figure 7.12. In Figure 7.11, the linear approximation model and the full system model look almost identical and show the expected avoided crossing shape for the conversion efficiency, however this is not seen in the adiabatic approximation

model. Using the adiabatic approximation model we would not expect to see an avoided crossing because the avoided crossing structure arises from the eigenstates of the combined atom–cavity system. For the eigenstates of the atom–cavity system atoms have some probability of being in the $|2\rangle$ state, which violates the assumptions of the adiabatic approximation model.

The adiabatic approximation model becomes badly behaved or unsolvable when the microwave fields are close to resonance with the atoms. From looking at the conversion efficiency from the full model and the linear model we can see that the highest conversion efficiency appears when the atoms are close to resonance with the input fields. This is where the adiabatic approximation breaks down, which means that it is not a very useful model for determining the maximum conversion efficiency. This shows that the work in this thesis is essential for improving the conversion efficiency, because the previous work using the adiabatic approximation is unable to predict the conversion efficiency in the region where it is highest.

For a more quantitative description of the differences between the models, the logarithm of the ratio of conversion efficiencies calculated using the different models was plotted in Figure 7.12. Using this comparison method, when there is no difference the result is zero which corresponds to white. It is also easy to compare how much larger or smaller the conversion efficiency calculated from the adiabatic approximation or linear models are compared to the full model.

For the adiabatic approximation model the biggest difference from the full model is when the fields are not far detuned from the atoms. In the full model there is an avoided crossing in this region, and the adiabatic model breaks down here. When fields are far detuned from the atoms the agreement is much better, but in the adiabatic approximation the conversion efficiency is larger than the full model. This is because the adiabatic model doesn't take into account any of the atomic decoherence and dephasing effects which reduce the conversion efficiency in the full model.

For the linear model we mainly see the differences in conversion efficiency with the full model when the cavity fields are large and close to resonance with the atoms. When the fields are detuned from the atoms then there is no visible difference from the full model. There is some disagreement between the linear model and the full model around the resonance peaks. This is likely due to the effects of saturation of the atoms which is not taken into account when using the linear model. The saturation effects reduce the effective number of atoms, which will reduce the conversion efficiency. A reduced effective number of atoms will also mean that the total coupling is smaller in the full model, which means that the size of the avoided crossing will be slightly smaller. This leads to the small differences in conversion efficiency around the avoided

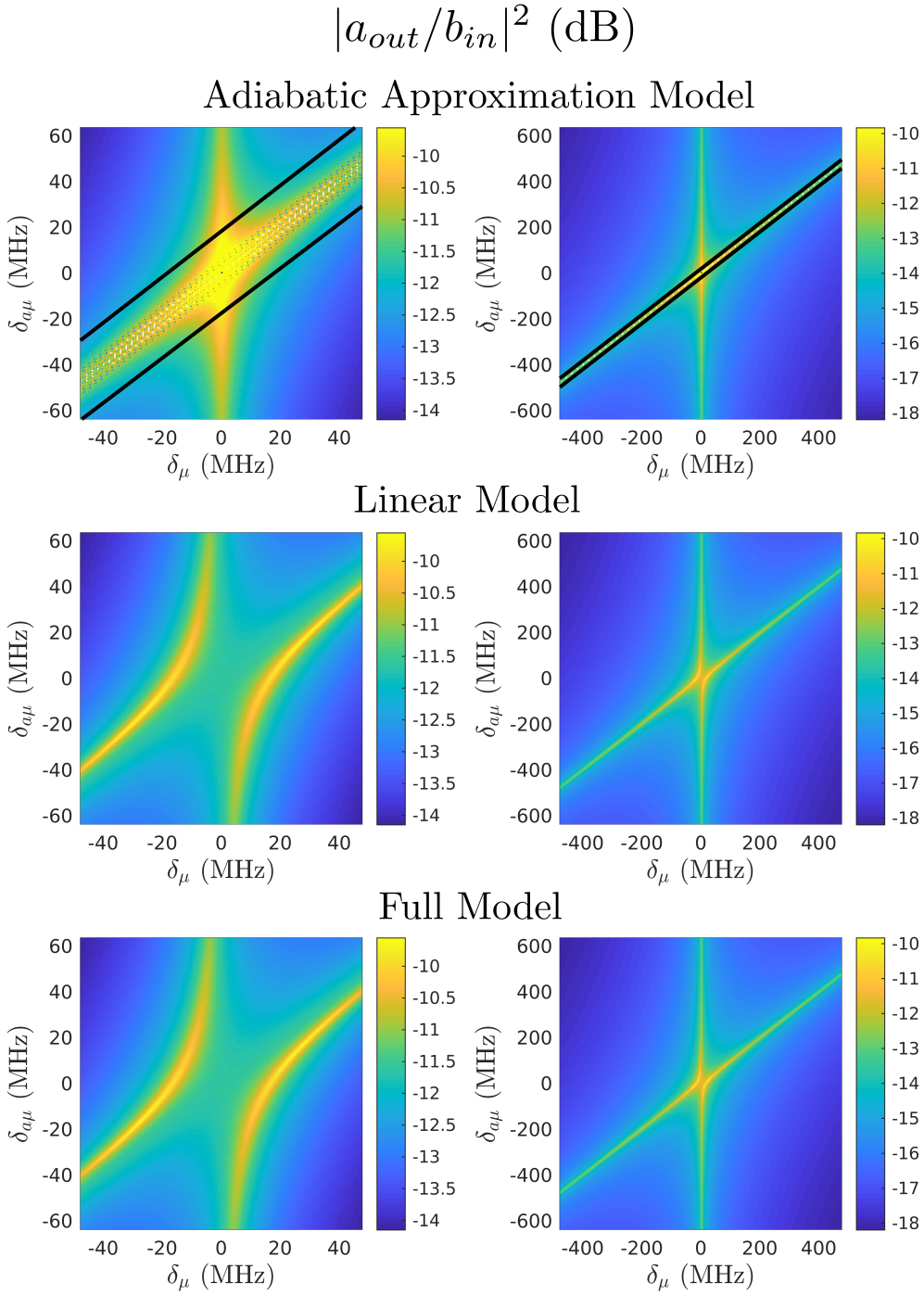

Figure 7.11: The conversion efficiency of the three models in dB. The two columns are for the same parameters, the first column is zoomed in to see the behaviour close to resonance and the second column is zoomed out to see the effects for large detunings. The first row is the results for the adiabatic approximation model, between the black lines the fields are too close to resonance and so the calculation of S (Equation 7.21) will not be accurate. The second row shows the results using the linear model, and the third row is for the full model.

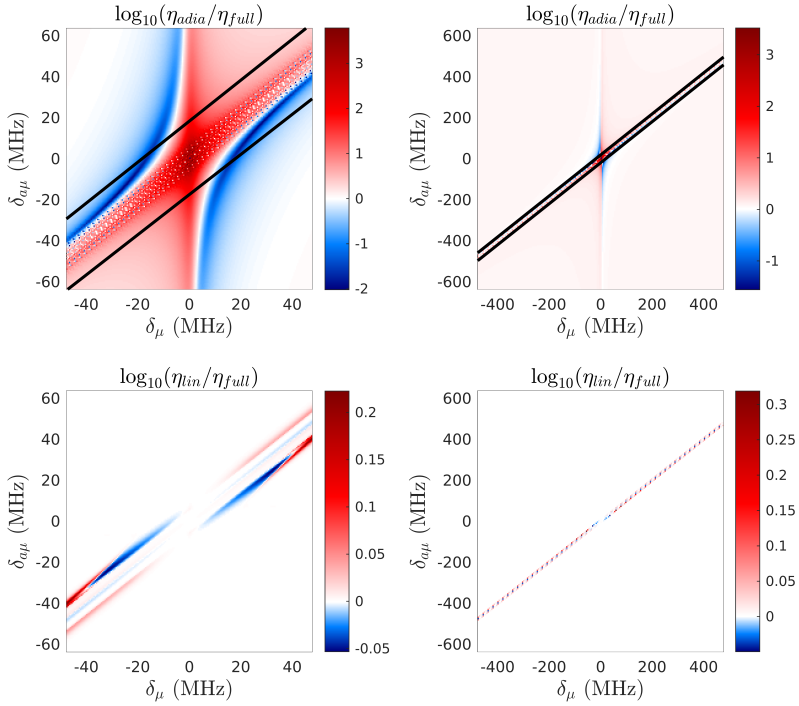

Figure 7.12: Plots showing the difference between the conversion efficiency predicted by the full model and the conversion efficiency from the adiabatic approximation model (top row) and the linear model (bottom row). The columns show a zoomed in view of what happens close to resonance (first column) and a zoomed out view showing the far detuned behaviour (second column), like in Figure 7.11. Red means that the simplified model is predicting higher conversion efficiency than the full model, and blue means it is predicting less. On the plots showing the comparison with the adiabatic approximation model, the area between the black lines indicates where the fields are too close to resonance with the atoms for the adiabatic approximation.

crossing, but these differences are very small, and so we can be reasonably confident using the linear model for very small input fields.

In this chapter we have demonstrated simulations of the experiments where our atoms are in the mode of both a microwave and an optical cavity. We have looked at various effects including the effect of atoms not in the optical beam path that still interact with the microwaves, and saturation effects from temperature and the microwave field. Finally, we have compared the full model with the adiabatic approximation model from earlier work [51], and the linear model developed in Chapter 6. The adiabatic model breaks down in the region where the highest conversion efficiency is and so it not a good model to use for maximising conversion efficiency. The linear model

shows small deviations when the fields are large, but should be accurate for small fields such as are used for the single photon regime of quantum information. In the next chapter we will use the linear approximation model to find ways to maximise the conversion efficiency.

Chapter 8

Optimising Upconversion Efficiency

For this upconversion device to be practical for quantum computing we need to have the conversion efficiency as high as possible. Now that we have an accurate model of the conversion device we can use it to find sensible experimental parameters which will maximise conversion efficiency.

We are looking to maximise for the regime where the fields are very small because this is likely what would be used for quantum computing. In this regime the saturation effects should be negligible. For this reason when maximising the conversion efficiency we can use the linear approximation model developed in Chapter 6. The linear approximation model for calculations is much faster than the full field model, and because it is linear with the fields, the conversion efficiency doesn't depend on the field amplitudes. Using the linear approximation, the output fields are linearly dependent on the input fields,

$$a_{out} = C_{aa}a_{in} + C_{ab}b_{in} \tag{8.1}$$

$$b_{out} = C_{ba}a_{in} + C_{bb}b_{in} \tag{8.2}$$

$|C_{aa}|^2$ and $|C_{bb}|^2$ represent the transmission through the optical and microwave cavities. $|C_{ab}|^2$ and $|C_{ba}|^2$ represent the conversion efficiency from microwave photons to optical photons and vice versa. So the term we are aiming to maximise in this chapter is $|C_{ab}|^2$.

8.1 Cavity Shift and Frequency Locking

To maximise the conversion efficiency we want to have the intra cavity fields as large as possible. Any fraction of the microwave input field that is reflected

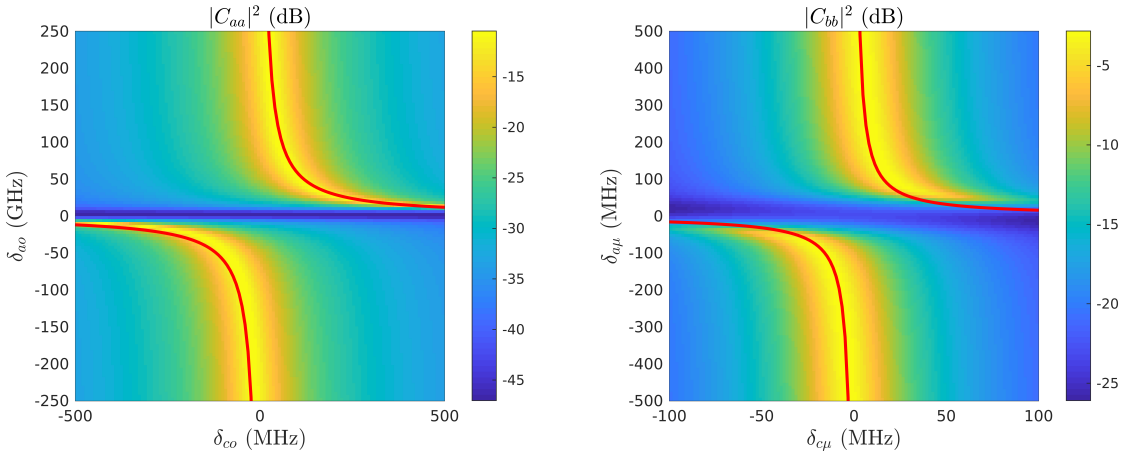

Figure 8.1: The transmission through the optical and microwave cavities when using the ground state microwave transition, as functions of the detunings between the fields and the cavities (δ_{co} or $\delta_{c\mu}$), and the fields and the atomic detunings (δ_{ao} or $\delta_{a\mu}$). The red lines show the dressed state detunings for the transitions, given by Equations 8.3. This simulation used 2.2×10^{15} atoms at a temperature of 150 mk.

rather than entering the cavity cannot contribute to the upconverted signal, and a larger intra cavity optical field directly corresponds to our upconverted signal. For an empty cavity, the intra cavity field is largest when the field is resonant with the cavity. However, when the atoms are in the cavity they will 'pull' the cavity resonance, and the field will be largest around the dressed states of the cavity. This can be seen by holding the input field frequency constant, and varying the cavity central frequency and the atomic transition frequency. From now on the atomic detuning will be used directly, rather than the magnetic field which was used previously.

When using the ground state microwave transition, this will apply for both the microwave and optical transitions as shown in Figure 8.1. These figures show the transmission through the cavity as a function of the detuning of the cavity from the input field and the detuning of the atomic transition frequency and the input field. From the cavity boundary conditions (Equation 2.13) larger cavity transmission means there is a larger intra cavity field amplitude. For a given atomic detuning, the transmission through the cavity will be peaked at the frequency corresponding to the dressed state of the atoms and cavity. Treating the atoms as identical 2 level atoms, the cavity detunings that correspond to the dressed states of the microwave cavity and microwave

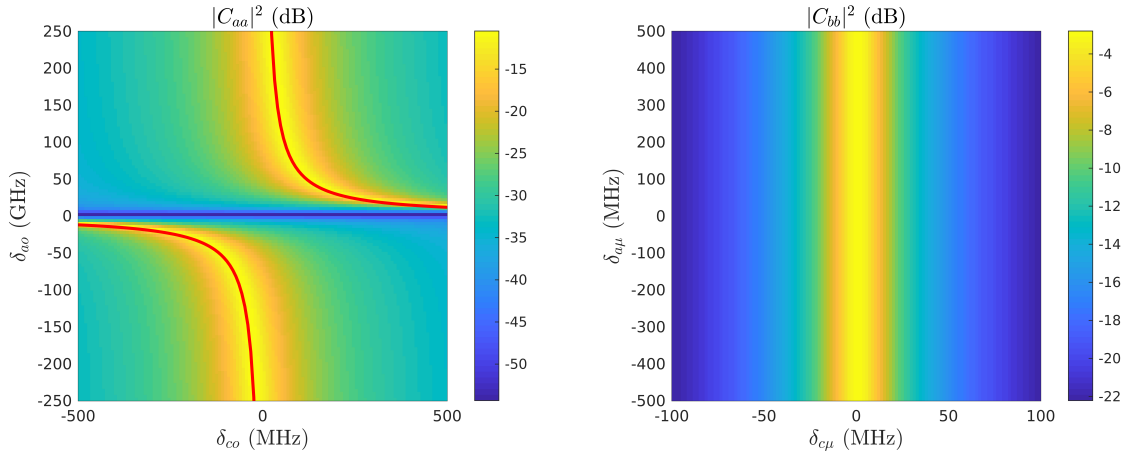

Figure 8.2: The transmission through the optical and microwave cavities when using the excited state microwave transition, as functions of the cavity detunings (δ_{co} or $\delta_{c\mu}$) and the atomic detunings (δ_{ao} or $\delta_{a\mu}$). The red lines in the first plot show the dressed state detunings for the optical transition, given by Equations 8.3. This simulation used 2.2×10^{15} atoms at a temperature of 150 mK.

transition, and the optical cavity and optical transition are

$$\delta_{c\mu} = \frac{N g_\mu^2}{\delta_{a\mu}} \tag{8.3a}$$

$$\delta_{co} = \frac{N_o g_o^2}{\delta_{ao}} \tag{8.3b}$$

Where N and N_o are the effective number of atoms being driven by the microwave and optical fields. The effective number of atoms for the microwave transition will be influenced by the temperature. N, the number of atoms, must be modified by a factor of $\rho_{11} - \rho_{22}$ (Equation 7.18) to account for the significant thermal population in the $|2\rangle$ state.

When using the excited state microwave transition there is the same shift of the cavity resonance for the optical cavity, but not for the microwave cavity (Figure 8.2). This is because there will be not enough atoms optically pumped into state $|2\rangle$ for the coupling between the microwaves and the $|2\rangle \rightarrow |3\rangle$ transition to split the cavity resonance. We have seen this earlier in earlier chapters for both experiments (Figure 5.11) and simulations (Figure 7.3) that do not show an avoided crossing.

8.1.1 Frequency Locking

Experimentally, the microwave and optical cavities can be 'locked' to the input fields using a method such as Pound-Drever-Hall stabilization [74]. Using these methods an error signal is generated based from the phase of the light exiting the cavity and varies with the detuning between the input light and the cavity. When the input light is close to resonant with the cavity, the error signal is linearly proportional to the detuning with a steep negative gradient, and is zero when on resonance. Therefore as the cavity is adjusted to minimise the error signal, this will also minimise the detuning between the resonance and the light and bring the system into resonance.

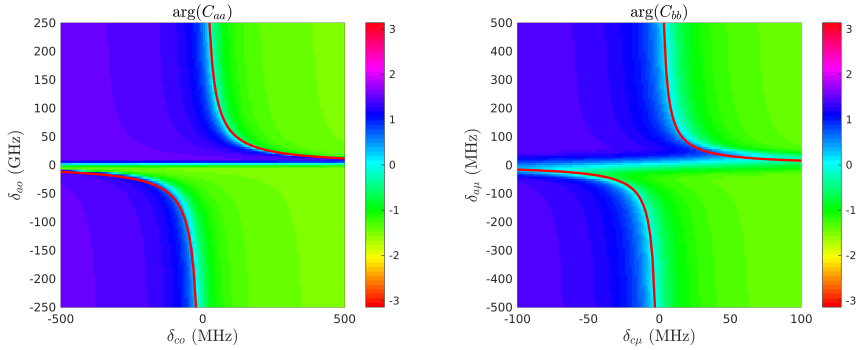

(a) Ground state microwave transition

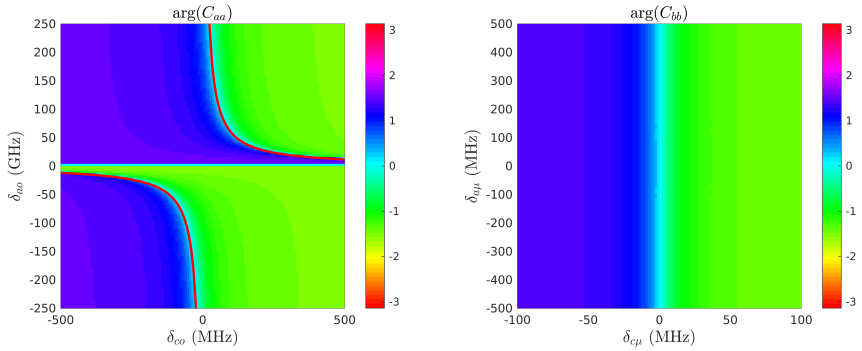

(b) Excited state microwave transition

Figure 8.3: The phase of the transmitted light through the optical and microwave cavities for the atomic schemes using the ground and excited state microwave transitions. These are from the same simulations as Figures 8.1 and 8.2. The red lines show the dressed state detunings, and match well to where the phase difference between the input and output fields is zero, which is coloured cyan on the colourmap.

On resonance, the phase shift of the transmitted light will be zero, and we can see on Figure 8.3 that tuning the cavity to the dressed states described by Equations 8.3 will also result in zero phase shift of the transmitted light. So, in simulations, tuning the cavities to the dressed states will simulate the effect of experimental frequency locking and will maximise the cavity fields. So, in simulations we will use the cavities tuned to the dressed states as a starting guess for the optimal detunings to simulate the effect of frequency locking, and then iterate from here to find the maximum conversion efficiency.

8.2 Comparing Atomic Systems

For this work we have usually been dealing with upconversion process using the ground state microwave transition, and then modifying that work to use the excited state transition. We are working to maximise the conversion efficiency, and so it will be useful to know which of the two atomic systems will have the higher conversion efficiency.

If we ignored the effects of population damping and dephasing in the atoms, then we would expect conversion efficiency to be higher if we used the microwave transition of the electronic ground state because the coupling between the microwave field and the microwave transition is greater. For the ground state microwave transition $g_\mu = 1.04\,\text{Hz}$, and for the excited state $g_\mu = 0.29\,\text{Hz}$. Greater coupling means that more microwave photons will be absorbed by the ensemble of atoms, and so more optical output photons can be emitted.

Additionally, the two systems will differ because of damping effects. For the process using the ground state microwave transition, when a microwave photon excites an atom into state $|2\rangle$ this may decay back to the ground state with a rate given by $\gamma_{12} = 0.09\,\text{Hz}$. If the excited state microwave transition is being used, when a microwave photon has excited the microwave transition from $|2\rangle$ to $|3\rangle$, this may decay back to $|2\rangle$ with a rate given by $\gamma_{23} = 0.09\,\text{Hz}$, but also it may decay back to the ground state with a decay rate given by $\gamma_{13} = 30\,\text{Hz}$. This additional decay mechanism may further decrease the efficiency of the process which uses the excited state microwave transition.

The linear approximation from Chapter 6 which we are using offers us a way to compare these two atomic schemes. In the linear approximation, the density matrix is assumed to contain terms that depend at most linearly on the optical and microwave fields,

$$\rho \approx \rho_0 + a\rho_a + \overline{a}\rho_{\overline{a}} + b\rho_b + \overline{b}\rho_{\overline{b}} \tag{8.4}$$

The term related to the conversion from microwave fields into optical fields is

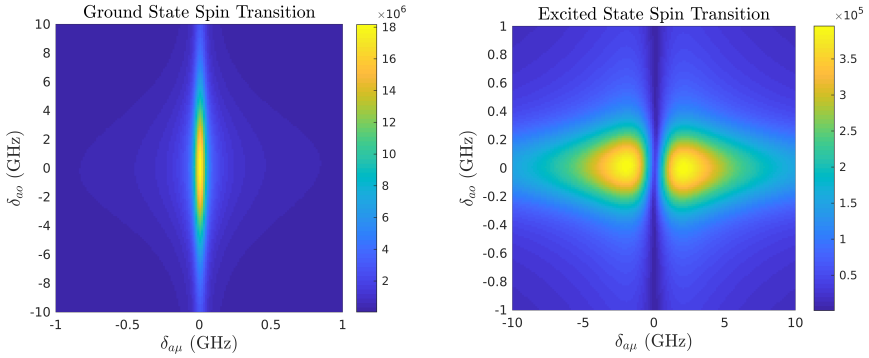

Figure 8.4: $|S_{b,13}|$ in Hz for the atomic schemes using the ground state and excited state spin transitions. Larger $|S_{b,13}|$ will correspond to a higher conversion efficiency. These were calculated assuming 1×10^{16} atoms at a temperature of 150 mK, with 1.74 mW of pump laser power. The scales are different for the two plots because the ground state has a maximum around 45 times larger in magnitude than the excited state.

$\rho_{b,13}$, the (1,3) element of ρ_b. $\rho_{b,13}$ describes how the coherence between states $|3\rangle$ and $|1\rangle$ depends with the intra cavity microwave field. As the intra cavity microwave field b increases, the coherence between the $|3\rangle$ and $|1\rangle$ states will increase as $b\rho_{13,b}$. As this coherence increases, the number of optical output photons will increase.

For the atomic ensemble, $S_{b,13}$ is the sum of all the $\rho_{b,13}$ terms for all the atoms, multiplied by the optical coupling,

$$S_{b,13} = \sum_k g_o \rho_{b,13,k} \tag{8.5}$$

If $S_{b,13}$ is larger it means that more optical output photons will be generated for a given intra cavity microwave field. So larger $S_{b,13}$ will mean the conversion efficiency is greater.

In Figure 8.4, $|S_{b,13}|$ is shown as a function of the optical and microwave atomic detunings for the atomic schemes using the ground and excited state spin transitions.These were calculated for a temperature of 150 mK, 1.74 dBm of pump laser power and 1×10^{16} atoms. We can see that the maximum value for $S_{b,13}$ is around 45 times larger when using the ground state spin transition than when using the excited state transition for these specific parameters. This means we would expect the maximum conversion efficiency to be much greater when using the ground state microwave transition, compared with the excited state transition. Experimentally, to increase conversion efficiency, we would want to select our atomic detunings such that $S_{b,13}$ is large.

8.3 Maximising Conversion Efficiency

We are now in a position to search for parameters which will maximise conversion efficiency.

For these simulations we will be using the ground state spin transition, and will consider a set up where all of the atoms are in the microwave field as well as the optical beam path. This set up reduces unnecessary loss from the atoms in the microwave field that are not in optical field, as described in Section 7.2. We want the intrinsic losses in our cavities to be small, because these will just reduce the conversion efficiency. We will take the intrinsic loss for our microwave cavity to be $\gamma_{\mu i} = 2\pi \times 0.65\,\text{MHz}$. The optical cavity will be treated as having the intrinsic loss of a high-Q whispering gallery mode resonator, with an intrinsic Q factor of 10^9. Whispering gallery mode resonators made from YSO have achieved Q factors this high [75], and Q factors even higher have been achieved with other materials [76, 77, 78].

8.3.1 Tunable Parameters

When attempting to maximise the conversion efficiency we have multiple experimental parameters we can adjust. For fixed microwave and optical field frequencies, we have control over the detunings between the atomic transitions and the fields, as well as the detunings between the cavity frequencies and the fields. We will have control over the power of the pump laser which will determine the Rabi frequency for the $|2\rangle \rightarrow |3\rangle$ transition.

Coupling Rates

Experimentally we also have control over the coupling rates γ_{oc} and $\gamma_{\mu c}$. For the optical coupling rate, when the optical cavity is a Fabry–Pérot cavity γ_{oc} can be modified by changing the reflectivity of the mirrors, or if the optical cavity is a whispering gallery mode resonator γ_{oc} can be modified by the distance between the resonator and the coupling prism or fibre [79]. The coupling into the microwave cavity can be chosen based on the design of cavity [80, 81]. As we can see in Figure 8.5, for fixed atomic and cavity detunings, adjusting the coupling rates can lead to very large increases in the conversion efficiency. For this figure number of atoms is 2.2×10^{15}, the temperature is 100 mK, and the detunings are $\delta_{co} = -1\,\text{MHz}$, $\delta_{ao} = -75\,\text{GHz}$, $\delta_{c\mu} = -1\,\text{MHz}$, $\delta_{a\mu} = -50\,\text{MHz}$, which were selected because they are in the region where the optical and microwave fields are large and close to resonance with the atoms. Conversion efficiency as a function of the coupling rates has a

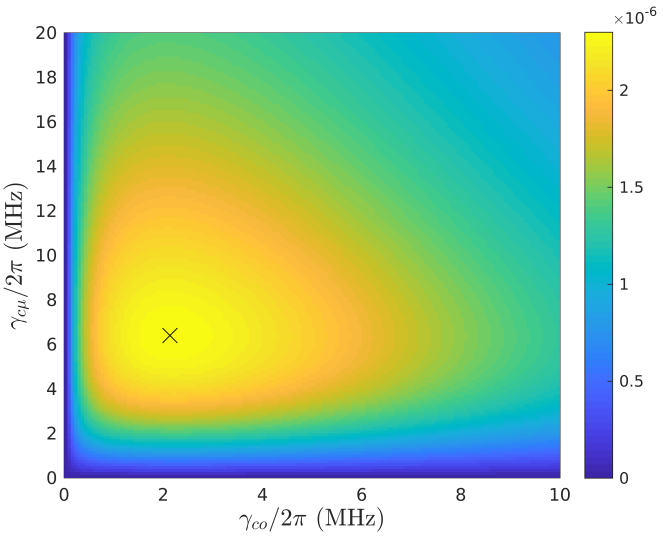

Figure 8.5: Conversion efficiency as a function of the optical cavity coupling rate γ_{oc} and the microwave cavity coupling rate $\gamma_{\mu c}$, the peak conversion efficiency is indicated by the black cross. All the detunings between the fields and the atoms and cavities are held constant. For these fixed detunings we can see that tuning the coupling rates correctly can lead to a dramatic increase in conversion efficiency.

defined peak; taking the coupling rates to infinity, while also being impossible experimentally, is also not desirable.

8.3.2 Scanning the Detunings

As a first step to maximising conversion efficiency it is useful to see how the conversion efficiency changes as a function of the detunings. In Figure 8.6 the conversion efficiency is shown as a function of the two atomic detunings. The cavity detunings are fixed to the dressed states (Equations 8.3), so will change as the atomic detunings change. We can see that the conversion efficiency is the same for each quadrant, so we will only need to search in one quadrant to find the maximum conversion efficiency. The peaks in Figure 8.6 will not be the maximum possible conversion efficiency because tuning the cavities to the dressed states is an approximation, and some perturbation to the detunings may be better. Additionally, we can also modify the coupling rates which will allow us to further increase conversion efficiency. It is also interesting to see the effect of laser pump power, as we can see in Figure 8.7 increasing the power of the pump laser both increases the maximum conversion efficiency and shifts the detunings which correspond to the maximum conversion efficiency. The linear model that we are using does not require that pump laser power is

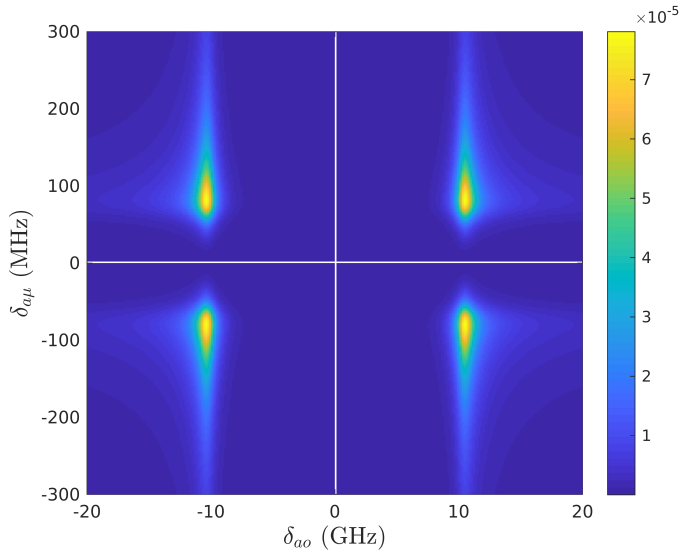

Figure 8.6: The conversion efficiency as a function of the optical and microwave atomic detunings, δ_{ao} and $\delta_{a\mu}$, and 1 mW of laser pump power at 100 mK. The cavity detunings are set to the dressed states, and so are defined in terms of the atomic detunings (Equation 8.3).

small. Some of the values for the pump laser power in Figure 8.7 are very high, and could cause heating and other unwanted effects. This could be mitigated by pulsing the pump laser; rather than continuously shining into the crystal the pump laser could be timed to only turn on for a fraction of a second with the input microwave photons. This would allow for the microwave photons to be converted into optical photons without too much heating of the crystal.

We can use the atomic detunings corresponding to the peaks in Figure 8.7 as initial guesses for finding the maximum conversion efficiency.

8.3.3 Method for Maximising Conversion efficiency

To maximise the conversion efficiency for a given number of atoms and laser pump power we begin by fixing the coupling rates, and using a minimisation algorithm to find the detunings which correspond to the highest conversion efficiency. Here we will adjust the atomic detunings and have the cavity detunings follow the dressed states. This is equivalent to finding the peaks in Figure 8.7, and will give us a reasonable idea of the optimal detuning. From here we fix these detunings, and will find the coupling rates γ_{oc} and $\gamma_{\mu c}$ which give the largest conversion efficiency. This is equivalent to finding the maximum of Figure 8.5.

These detunings and coupling rates provide the initial startpoint for our

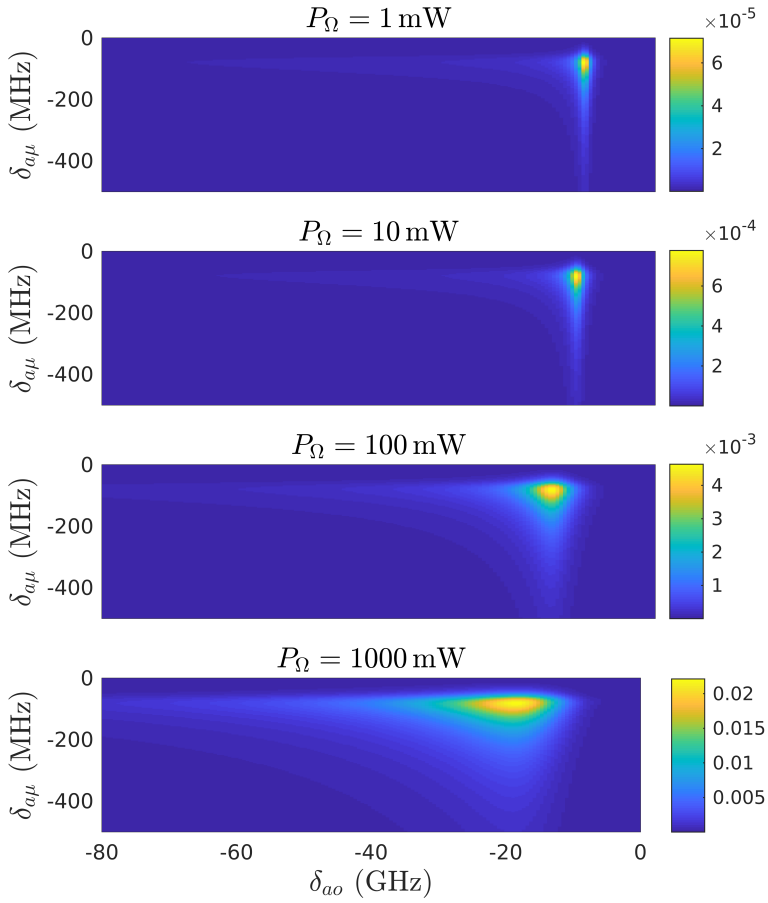

Figure 8.7: The conversion efficiency as a function of the optical and microwave atomic detunings for different laser pump powers P_Ω. The cavity detunings are tuned to the dressed state detunings (Equation 8.3). The temperature is 100 mK and there are 2.2×10^{15} atoms. The detunings correspond to the lower left quadrant of Figure 8.6.

minimisation algorithm to find the maximum conversion efficiency. The conversion efficiency is found as a function of the atomic detunings δ_{ao} and $\delta_{a\mu}$, the cavity detunings δ_{co} and $\delta_{c\mu}$, as well as the coupling rates γ_{oc}, $\gamma_{\mu c}$. This method will require us to find the conversion efficiency many times, for many different values for the parameters, and so the linear model is very well suited to this because it allows the conversion efficiency to be calculated faster than the full model.

8.3.4 Results from Maximising Conversion Efficiency

Using this method, the maximum conversion efficiency was calculated for a range of laser pump powers as shown in Figure 8.8. When there are $N = 2.2 \times 10^{15}$ atoms, we see there is a dramatic increase in the conversion efficiency by increasing the laser pump power from 1 mW to around 100 mW as we can see in Figure 8.8a. For 1 mW of pump power the conversion efficiency is 0.6%, and at 100 mW it increases to 17%. The gains in conversion efficiency from increasing the laser pump power level off, and at 1000 mW the conversion efficiency is 20.8% (Figure 8.8b). Increasing the laser pump power means that atoms which have been excited into the $|2\rangle$ state will have a higher probability of being excited further to $|3\rangle$. The conversion efficiency levels off for high pump power, because as the pump power is increased, the probability of further excitation will approach 100%, but there are still mechanisms which cause losses in other parts of the upconversion process which will reduce the conversion efficiency. Because we have been considering a device where both cavities have two ports, photons lost via output from one of the microwave ports, or from the optical port we are not measuring will decrease the conversion efficiency, as will the intrinsic loss from the cavities. Conversion efficiency will also be reduced due to the damping effects of the $|3\rangle$ state.

If the number of atoms is increased, for example by using a larger crystal, or by increasing the dopant concentration, then the maximum conversion efficiency is also increased, as shown in Figure 8.8. Here the number of atoms is increased by over a factor of four, from 2.2×10^{15} to 1×10^{16}. For low pump power this leads to a large increase in conversion efficiency; for 3 mW of pump power, the conversion efficiency is increased from 5.5% to 12.9%. However for higher power there is only a modest increase in the conversion efficiency. With this greater number of atoms the maximum conversion efficiency is 21% with 100 mW of pump power, and 23% when the pump power is further increased to 1000 mW.

For this process of maximising the conversion efficiency we have been considering a device with two microwave ports and two optical ports, with

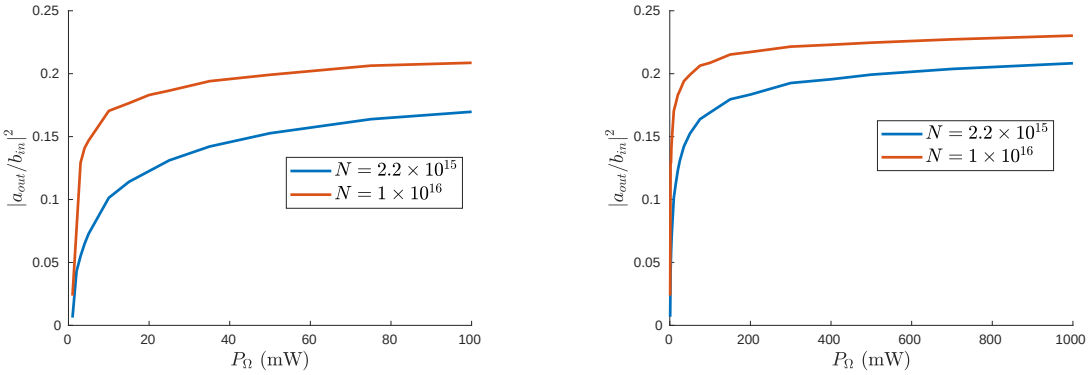

(a) Pump power up to 100 mW

(b) Pump power up to 1000 mW

Figure 8.8: The maximum conversion efficiency $|a_{out}/b_{in}|^2$, as a function of the laser pump power P_Ω. These simulations were performed for 2.2×10^{15} and 1×10^{16} atoms at a temperature of $T = 100$ mK. The detunings between the fields and the cavities, and the fields and the atomic transition, as well as the coupling rates were tuned to give the maximum conversion efficiency.

the only input being into one of the microwave ports. For this setup, we have only been considering the output from one of the optical ports. Combining the output from both optical ports would lead to a doubling of the conversion efficiency. Alternatively we could design our optical cavity to have a single port, which would have the same effect. By doing this we should be able to achieve conversion efficiencies above 40%. Our microwave cavity also has two ports, and so if we switched to a single port microwave cavity this would mean there would be no photons lost via the second port. By only having one port this would mean that for a given microwave input field b_{in}, the intra cavity microwave field b would be larger, which would lead to higher conversion efficiencies. This could lead to a further doubling of the conversion efficiency, potentially leading to maximum conversion efficiencies above 80%.

In this chapter we have worked to maximise the conversion efficiency of our upconversion device, which has been one of the overall goals of this thesis. The conversion efficiency will be greater when the intra cavity fields are greater, and so the cavities can be tuned to the dressed states which is where the cavity fields are greatest. Experimentally we will have control over several parameters, including the detunings and the coupling rates. These parameters were adjusted to find the maximum conversion efficiency. Conversion efficiency increases with laser pump power, and so the maximum conversion efficiency was calculated as a function of the pump power. This showed maximum conversion efficiencies of over 20% for our experimental parameters.

By modifying our device such that the microwave and optical cavities each only have one port, we predict that the conversion efficiency could increase to above 80%.

Conclusion

In this thesis we have worked to develop a theoretical model of a device for the coherent conversion of microwave photons into optical photons. The device has a crystal of $^{170}Er^{3+}$:YSO inside the modes of overlapping microwave and optical cavities, driven by an optical pump laser. The aim is to combine an input microwave photon and an optical pump photon via interactions with the atoms. This will produce an optical photon carrying the information originally encoded in the input microwave photon.

We started by developing equations of motion for the microwave and optical intra cavity fields using input output formalism from [55]. This yielded two equations for the microwave and optical fields, which were coupled via their interaction with the atoms.

Using an open quantum systems approach we developed a model for an atom interacting with the light fields, taking into account the effects of temperature, damping and other dephasing processes. This single atom model was used to develop a description of the ensemble of inhomogeneously broadened atoms; specifically finding the atom-field interaction terms in the input output equations. We developed numerical methods for calculating these terms quickly and accurately. A simplified model was also developed, for the case where the microwave and optical fields are small, which is relevant to the quantum information regime. This model still allows for a strong optical pump.

We compared our full model with single pass experiments, which demonstrated good agreement with few fitted parameters. From here the full model was used to simulate double cavity device. Various effects were investigated including parasitic absorption, and saturation of the microwave transition. The full model was compared with the linear model, and the adiabatic approximation model based on [51]. The full model agrees well with the linear model for small fields, while the adiabatic approximation model generally over estimates the conversion efficiency and breaks down in the regions where the full model predicts large conversion efficiency. So the models we have developed are a necessary extension to be able to predict the maximum

conversion efficiency.

Finally, we used the linear model to find parameters which would maximise the conversion efficiency for small fields, and predict that conversion efficiencies of over 20% should be attainable with current experimental techniques. This is far greater than has so far been experimentally achieved using rare earth ions.

Finally, we used the linear model to find parameters which would maximise the conversion efficiency for small fields. We predict that for using our double cavity device, where each cavity has two ports, the maximum conversion efficiency is above 20%. This is far greater than has so far been experimentally achieved using rare earth ions. Furthermore, if we used a modified device where the cavities each had one port, then the maximum conversion efficiency reach beyond 80%.

Going forward, the numerical models developed in this thesis can be used to inform experiments. These can be used to tune the frequencies and coupling rates to maximise the conversion efficiency, for devices where the cavities have one or two ports. This future work could also include a more thorough investigation of the maximum conversion efficiency using the excited state system.

Although this model was developed in the context of using ^{170}Er, the theory is quite general and could easily be extended to other atoms with similar atomic structure. Additionally, this theory could be developed further, extending the three level model to a four level model to include both Zeeman levels from the ground and excited electronic states.

Bibliography

[1] F. Arute, K. Arya, R. Babbush, D. Bacon *et al.*, "Quantum supremacy using a programmable superconducting processor," *Nature*, vol. 574, no. 7779, pp. 505–510, Oct. 2019.

[2] M. A. Nielsen, I. L. Chuang, and I. L. Chuang, *Quantum Computation and Quantum Information*. Cambridge University Press, Oct. 2000.

[3] R. Horodecki, P. Horodecki, M. Horodecki, and K. Horodecki, "Quantum entanglement," *Reviews of Modern Physics*, vol. 81, no. 2, pp. 865–942, Jun. 2009.

[4] P. W. Shor, "Polynomial-Time Algorithms for Prime Factorization and Discrete Logarithms on a Quantum Computer," *SIAM Review*, vol. 41, no. 2, pp. 303–332, Jan. 1999.

[5] A. Ekert and R. Jozsa, "Quantum computation and Shor's factoring algorithm," *Reviews of Modern Physics*, vol. 68, no. 3, pp. 733–753, Jul. 1996.

[6] L. M. K. Vandersypen, M. Steffen, G. Breyta, C. S. Yannoni, M. H. Sherwood, and I. L. Chuang, "Experimental realization of Shor's quantum factoring algorithm using nuclear magnetic resonance," *Nature*, vol. 414, no. 6866, pp. 883–887, Dec. 2001.

[7] T. Monz, D. Nigg, E. A. Martinez, M. F. Brandl *et al.*, "Realization of a scalable Shor algorithm," *Science*, vol. 351, no. 6277, pp. 1068–1070, Mar. 2016.

[8] E. Martín-López, A. Laing, T. Lawson, R. Alvarez, X.-Q. Zhou, and J. L. O'Brien, "Experimental realization of Shor's quantum factoring algorithm using qubit recycling," *Nature Photonics*, vol. 6, no. 11, pp. 773–776, Nov. 2012.

[9] J. A. Smolin, G. Smith, and A. Vargo, "Oversimplifying quantum factoring," *Nature*, vol. 499, no. 7457, pp. 163–165, Jul. 2013.

[10] A. W. Harrow, A. Hassidim, and S. Lloyd, "Quantum Algorithm for Linear Systems of Equations," *Physical Review Letters*, vol. 103, no. 15, p. 150502, Oct. 2009.

[11] S. Aaronson, "Read the fine print," *Nature Physics*, vol. 11, no. 4, pp. 291–293, Apr. 2015.

[12] G. Wang, "Efficient Quantum Algorithms for Analyzing Large Sparse Electrical Networks," *Quantum Info. Comput.*, vol. 17, no. 11-12, pp. 987–1026, Sep. 2017.

[13] A. Montanaro and S. Pallister, "Quantum algorithms and the finite element method," *Physical Review A*, vol. 93, no. 3, p. 032324, Mar. 2016.

[14] V. Dunjko, J. M. Taylor, and H. J. Briegel, "Quantum-Enhanced Machine Learning," *Physical Review Letters*, vol. 117, no. 13, p. 130501, Sep. 2016.

[15] V. M. Schäfer, C. J. Ballance, K. Thirumalai, L. J. Stephenson, T. G. Ballance, A. M. Steane, and D. M. Lucas, "Fast quantum logic gates with trapped-ion qubits," *Nature*, vol. 555, no. 7694, pp. 75–78, Mar. 2018.

[16] G. K. Brennen, C. M. Caves, P. S. Jessen, and I. H. Deutsch, "Quantum Logic Gates in Optical Lattices," *Physical Review Letters*, vol. 82, no. 5, pp. 1060–1063, Feb. 1999.

[17] C. Monroe, "Quantum information processing with atoms and photons," *Nature*, vol. 416, no. 6877, pp. 238–246, Mar. 2002.

[18] D. G. Cory, A. F. Fahmy, and T. F. Havel, "Ensemble quantum computing by NMR spectroscopy," *Proceedings of the National Academy of Sciences*, vol. 94, no. 5, pp. 1634–1639, Mar. 1997.

[19] D. Loss and D. P. DiVincenzo, "Quantum computation with quantum dots," *Physical Review A*, vol. 57, no. 1, pp. 120–126, Jan. 1998.

[20] B. Trauzettel, D. V. Bulaev, D. Loss, and G. Burkard, "Spin qubits in graphene quantum dots," *Nature Physics*, vol. 3, no. 3, pp. 192–196, Mar. 2007.

[21] T. B. Pittman and J. D. Franson, "Cyclical quantum memory for photonic qubits," *Physical Review A*, vol. 66, no. 6, p. 062302, Dec. 2002.

[22] L. Childress and R. Hanson, "Diamond NV centers for quantum computing and quantum networks," *MRS Bulletin*, vol. 38, no. 2, pp. 134–138, Feb. 2013.

[23] M. H. Devoret, A. Wallraff, and J. M. Martinis, "Superconducting Qubits: A Short Review," *arXiv:cond-mat/0411174*, Nov. 2004, arXiv: cond-mat/0411174.

[24] G. Wendin, "Quantum information processing with superconducting circuits: a review," *Reports on Progress in Physics*, vol. 80, no. 10, p. 106001, Sep. 2017.

[25] P. Krantz, M. Kjaergaard, F. Yan, T. P. Orlando, S. Gustavsson, and W. D. Oliver, "A quantum engineer's guide to superconducting qubits," *Applied Physics Reviews*, vol. 6, no. 2, p. 021318, Jun. 2019.

[26] S. Wehner, D. Elkouss, and R. Hanson, "Quantum internet: A vision for the road ahead," *Science*, vol. 362, no. 6412, Oct. 2018.

[27] R. Van Meter and S. J. Devitt, "The Path to Scalable Distributed Quantum Computing," *Computer*, vol. 49, no. 9, pp. 31–42, Sep. 2016.

[28] N. J. Lambert, A. Rueda, F. Sedlmeir, and H. G. L. Schwefel, "Coherent Conversion Between Microwave and Optical Photons—An Overview of Physical Implementations," *Advanced Quantum Technologies*, vol. 3, no. 1, p. 1900077, 2020, _eprint: https://onlinelibrary.wiley.com/doi/pdf/10.1002/qute.201900077.

[29] R. W. Boyd, *Nonlinear Optics*. Elsevier, Jan. 2003.

[30] M. J. Khan, J. C. Chen, and S. Kaushik, "Optical detection of terahertz radiation by using nonlinear parametric upconversion," *Optics Letters*, vol. 32, no. 22, pp. 3248–3250, Nov. 2007.

[31] D. V. Strekalov, A. A. Savchenkov, A. B. Matsko, and N. Yu, "Efficient upconversion of subterahertz radiation in a high-Q whispering gallery resonator," *Optics Letters*, vol. 34, no. 6, pp. 713–715, Mar. 2009.

[32] A. Rueda, F. Sedlmeir, M. C. Collodo, U. Vogl *et al.*, "Efficient microwave to optical photon conversion: an electro-optical realization," *Optica*, vol. 3, no. 6, pp. 597–604, Jun. 2016.

[33] D. V. Strekalov, H. G. L. Schwefel, A. A. Savchenkov, A. B. Matsko, L. J. Wang, and N. Yu, "Microwave whispering-gallery resonator for efficient

optical up-conversion," *Physical Review A*, vol. 80, no. 3, p. 033810, Sep. 2009.

[34] M. Aspelmeyer, T. J. Kippenberg, and F. Marquardt, "Cavity optomechanics," *Reviews of Modern Physics*, vol. 86, no. 4, pp. 1391–1452, Dec. 2014.

[35] J. Bochmann, A. Vainsencher, D. D. Awschalom, and A. N. Cleland, "Nanomechanical coupling between microwave and optical photons," *Nature Physics*, vol. 9, no. 11, pp. 712–716, Nov. 2013.

[36] R. W. Andrews, R. W. Peterson, T. P. Purdy, K. Cicak, R. W. Simmonds, C. A. Regal, and K. W. Lehnert, "Bidirectional and efficient conversion between microwave and optical light," *Nat Phys*, vol. 10, no. 4, pp. 321–326, Apr. 2014.

[37] A. P. Higginbotham, P. S. Burns, M. D. Urmey, R. W. Peterson *et al.*, "Harnessing electro-optic correlations in an efficient mechanical converter," *Nature Physics*, vol. 14, no. 10, pp. 1038–1042, Oct. 2018.

[38] J. Han, T. Vogt, C. Gross, D. Jaksch, M. Kiffner, and W. Li, "Coherent Microwave-to-Optical Conversion via Six-Wave Mixing in Rydberg Atoms," *Physical Review Letters*, vol. 120, no. 9, p. 093201, Mar. 2018.

[39] J. P. Covey, A. Sipahigil, and M. Saffman, "Microwave-to-optical conversion via four-wave mixing in a cold ytterbium ensemble," *Physical Review A*, vol. 100, no. 1, p. 012307, Jul. 2019.

[40] T. F. Gallagher, "Rydberg Atoms," Sep. 1994.

[41] A. Osada, R. Hisatomi, A. Noguchi, Y. Tabuchi *et al.*, "Cavity Optomagnonics with Spin-Orbit Coupled Photons," *Physical Review Letters*, vol. 116, no. 22, p. 223601, Jun. 2016.

[42] J. Haigh, A. Nunnenkamp, A. Ramsay, and A. Ferguson, "Triple-Resonant Brillouin Light Scattering in Magneto-Optical Cavities," *Physical Review Letters*, vol. 117, no. 13, p. 133602, Sep. 2016.

[43] A. Osada, A. Gloppe, R. Hisatomi, A. Noguchi *et al.*, "Brillouin Light Scattering by Magnetic Quasivortices in Cavity Optomagnonics," *Physical Review Letters*, vol. 120, no. 13, p. 133602, Mar. 2018.

[44] R. Hisatomi, A. Osada, Y. Tabuchi, T. Ishikawa *et al.*, "Bidirectional conversion between microwave and light via ferromagnetic magnons," *Physical Review B*, vol. 93, no. 17, p. 174427, May 2016.

[45] J. R. Everts, M. C. Berrington, R. L. Ahlefeldt, and J. J. Longdell, "Microwave to optical photon conversion via fully concentrated rare-earth-ion crystals," *Physical Review A*, vol. 99, no. 6, p. 063830, Jun. 2019.

[46] X. Fernandez-Gonzalvo, S. P. Horvath, Y.-H. Chen, and J. J. Longdell, "Cavity-enhanced raman heterodyne spectroscopy in Er^{3+}:Y_2SiO_5 for microwave to optical signal conversion," *Phys. Rev. A*, vol. 100, p. 033807, Sep 2019.

[47] N. G. Connelly, T. Damhus, R. M. Hartshorn, and A. T. Hutton, Eds., *Nomenclature of Inorganic Chemistry*. The Royal Society of Chemistry, 2005.

[48] E. C. Ridley, "Self-consistent fields without exchange for Pr^{3+} and Tm^{3+}," *Mathematical Proceedings of the Cambridge Philosophical Society*, vol. 56, no. 1, pp. 41–54, Jan. 1960.

[49] A. Abragam and B. Bleaney, *Electron Paramagnetic Resonance of Transition Ions*. Oxford: Oxford University Press, Jul. 2012, reprint edition.

[50] L. Allen and J. H. Eberly, *Optical resonance and two-level atoms*. Wiley, 1975.

[51] L. A. Williamson, Y.-H. Chen, and J. J. Longdell, "Magneto-Optic Modulator with Unit Quantum Efficiency," *Physical Review Letters*, vol. 113, no. 20, p. 203601, Nov. 2014.

[52] C. O'Brien, N. Lauk, S. Blum, G. Morigi, and M. Fleischhauer, "Interfacing Superconducting Qubits and Telecom Photons via a Rare-Earth-Doped Crystal," *Physical Review Letters*, vol. 113, no. 6, p. 063603, Aug. 2014.

[53] S. Blum, C. O'Brien, N. Lauk, P. Bushev, M. Fleischhauer, and G. Morigi, "Interfacing microwave qubits and optical photons via spin ensembles," *Physical Review A*, vol. 91, no. 3, p. 033834, Mar. 2015.

[54] X. Fernandez-Gonzalvo, Y.-H. Chen, C. Yin, S. Rogge, and J. J. Longdell, "Coherent frequency up-conversion of microwaves to the optical telecommunications band in an Er:YSO crystal," *Physical Review A*, vol. 92, no. 6, p. 062313, Dec. 2015.

[55] C. Gardiner and P. Zoller, *Quantum Noise: A Handbook of Markovian and Non-Markovian Quantum Stochastic Methods with Applications to Quantum Optics*. Springer Science & Business Media, Aug. 2004.

[56] C. W. Gardiner and M. J. Collett, "Input and output in damped quantum systems: Quantum stochastic differential equations and the master equation," *Physical Review A*, vol. 31, no. 6, pp. 3761–3774, Jun. 1985.

[57] M. J. Collett and C. W. Gardiner, "Squeezing of intracavity and traveling-wave light fields produced in parametric amplification," *Physical Review A*, vol. 30, no. 3, pp. 1386–1391, Sep. 1984.

[58] H. J. Carmichael, *Statistical Methods in Quantum Optics 1: Master Equations and Fokker-Planck Equations*, ser. Theoretical and Mathematical Physics. Berlin Heidelberg: Springer-Verlag, 1999.

[59] J. Johansson, P. Nation, and F. Nori, "QuTiP 2: A Python framework for the dynamics of open quantum systems," *Computer Physics Communications*, vol. 184, no. 4, pp. 1234–1240, Apr. 2013.

[60] A. Meurer, C. P. Smith, M. Paprocki, O. Čertík *et al.*, "Sympy: symbolic computing in python," *PeerJ Computer Science*, vol. 3, p. e103, Jan. 2017.

[61] P. Virtanen, R. Gommers, T. E. Oliphant, M. Haberland *et al.*, "SciPy 1.0–Fundamental Algorithms for Scientific Computing in Python," *arXiv:1907.10121 [physics]*, Jul. 2019, arXiv: 1907.10121.

[62] E. Anderson, Z. Bai, C. Bischof, S. Blackford *et al.*, *LAPACK Users' Guide*, 3rd ed. Philadelphia, PA: Society for Industrial and Applied Mathematics, 1999.

[63] L. Yang, L. Zhang, X. Li, L. Han *et al.*, "Autler-Townes effect in a strongly driven electromagnetically induced transparency resonance," *Physical Review A*, vol. 72, no. 5, p. 053801, Nov. 2005.

[64] M. Abramowitz and I. A. Stegun, *Handbook of Mathematical Functions with Formulas, Graphs, and Mathematical Tables*. U.S. Government Printing Office, 1948.

[65] A. Quarteroni, R. Sacco, and F. Saleri, *Numerical Mathematics*, 2nd ed., ser. Texts in Applied Mathematics. Berlin Heidelberg: Springer-Verlag, 2007.

[66] T. Böttger, Y. Sun, C. W. Thiel, and R. L. Cone, "Spectroscopy and dynamics of Er^{3+}:Y_2SiO_5 at 1.5 μm," *Phys. Rev. B*, vol. 74, p. 075107, Aug 2006.

[67] G. G. G. King, 2019, Private communication.

[68] D. J. Griffiths, *Introduction to Electrodynamics*. Pearson, 2013.

[69] B. M. Garraway, "The Dicke model in quantum optics: Dicke model revisited," *Philosophical Transactions of the Royal Society A: Mathematical, Physical and Engineering Sciences*, vol. 369, no. 1939, pp. 1137–1155, Mar. 2011.

[70] M. Tavis and F. W. Cummings, "Approximate Solutions for an N - Molecule-Radiation-Field Hamiltonian," *Physical Review*, vol. 188, no. 2, pp. 692–695, Dec. 1969.

[71] E. Jaynes and F. Cummings, "Comparison of quantum and semiclassical radiation theories with application to the beam maser," *Proceedings of the IEEE*, vol. 51, no. 1, pp. 89–109, Jan. 1963.

[72] N. C. Wong, E. S. Kintzer, J. Mlynek, R. G. DeVoe, and R. G. Brewer, "Raman heterodyne detection of nuclear magnetic resonance," *Physical Review B*, vol. 28, no. 9, pp. 4993–5010, Nov. 1983.

[73] L. A. Williamson, "Complete Conversion Between Microwave Fields and Optical Fields," Hons. thesis, University of Otago, 2012.

[74] E. D. Black, "An introduction to Pound–Drever–Hall laser frequency stabilization," *American Journal of Physics*, vol. 69, no. 1, pp. 79–87, Dec. 2000.

[75] D. Norman, 2019, Private communication.

[76] M. L. Gorodetsky, A. A. Savchenkov, and V. S. Ilchenko, "Ultimate Q of optical microsphere resonators," *Optics Letters*, vol. 21, no. 7, pp. 453–455, Apr. 1996.

[77] D. W. Vernooy, V. S. Ilchenko, H. Mabuchi, E. W. Streed, and H. J. Kimble, "High-Q measurements of fused-silica microspheres in the near infrared," *Optics Letters*, vol. 23, no. 4, pp. 247–249, Feb. 1998.

[78] A. B. Matsko, A. A. Savchenkov, D. Strekalov, V. S. Ilchenko, and L. Maleki, "Review of Applications of Whispering-Gallery Mode Resonators in Photonics and Nonlinear Optics," *Interplanetary Network Progress Report*, vol. 42-162, pp. 1–51, Aug 2005.

[79] M. L. Gorodetsky and V. S. Ilchenko, "Optical microsphere resonators: optimal coupling to high-Q whispering-gallery modes," *Journal of the Optical Society of America B*, vol. 16, no. 1, p. 147, Jan. 1999.

[80] M. Mehdizadeh, T. Ishii, J. Hyde, and W. Froncisz, "Loop-Gap Resonator: A Lumped Mode Microwave Resonant Structure," *IEEE Transactions on Microwave Theory and Techniques*, vol. 31, no. 12, pp. 1059–1064, Dec. 1983.

[81] M. Pierre, I.-M. Svensson, S. Raman Sathyamoorthy, G. Johansson, and P. Delsing, "Storage and on-demand release of microwaves using superconducting resonators with tunable coupling," *Applied Physics Letters*, vol. 104, no. 23, p. 232604, Jun. 2014.

Appendix A

Driven Two Level Atom at Finite Temperature

The Master Equation describing a two level atom at finite temperature, driven by a microwave field is,

$$\frac{\mathrm{d}\rho}{\mathrm{d}t} = -i[\hat{H}, \rho] \tag{A.1}$$

$$+ \frac{\gamma}{2}(N+1)(2\sigma_-\rho\sigma_+ - \sigma_+\sigma_-\rho - \rho\sigma_+\sigma_-) \tag{A.2}$$

$$+ \frac{\gamma}{2}N(2\sigma_+\rho\sigma_- - \sigma_-\sigma_+\rho + \rho\sigma_-\sigma_+) \tag{A.3}$$

Where the Hamiltonian is

$$\hat{H} = \frac{1}{2}\Omega\sigma_z + g_\mu b\sigma_+ + g_\mu^* b^*\sigma_- \tag{A.4}$$

and N is the photon population of the thermal bath, given by the Planck distribution.

The probability of the atom being in the excited state is

$$\rho_{22} = \langle\sigma_+\sigma_-\rangle = \mathrm{Tr}(\rho\sigma_+\sigma_-) \tag{A.5}$$

This has the equation of motion,

$$\dot{\rho_{22}} = \frac{\mathrm{d}}{\mathrm{d}t}\mathrm{Tr}(\rho\sigma_+\sigma_-) \tag{A.6}$$

$$= -i\mathrm{Tr}\left([\hat{H}, \rho]\sigma_+\sigma_-\right)$$

$$+ \frac{\gamma}{2}(N+1)\mathrm{Tr}\left(2\sigma_-\rho\sigma_+\sigma_+\sigma_- - \sigma_+\sigma_-\rho\sigma_+\sigma_- - \rho\sigma_+\sigma_-\sigma_+\sigma_-\right) \tag{A.7}$$

$$+ \frac{\gamma}{2}N\mathrm{Tr}(2\sigma_+\rho\sigma_-\sigma_+\sigma_- - \sigma_-\sigma_+\rho\sigma_+\sigma_- + \rho\sigma_-\sigma_+\sigma_+\sigma_-)$$

The Hamiltonian evolution described by the first line of Equation A.7 evaluates as

$$-i\mathrm{Tr}\left([\hat{H},\rho]\sigma_+\sigma_-\right) = -i(g_\mu b\left\langle\sigma_+\right\rangle - g_\mu^* b^*\left\langle\sigma_-\right\rangle) \tag{A.8}$$

where $\langle\sigma_+\rangle = \mathrm{Tr}(\rho\sigma_+)$ and $\langle\sigma_-\rangle = \mathrm{Tr}(\rho\sigma_-)$. The interactions with the thermal bath, given by the second and third lines of Equation A.7 evaluate as,

$$-\gamma(N+1)\left\langle\sigma_+\sigma_-\right\rangle + \gamma N\left\langle\sigma_-\sigma_+\right\rangle \tag{A.9}$$

Using the normalisation condition,

$$\rho_{11}+\rho_{22} = \left\langle\sigma_-\sigma_+\right\rangle + \left\langle\sigma_+\sigma_-\right\rangle = 1 \tag{A.10}$$

So the equation of motion for the excited state population is

$$\dot{\rho_{22}} = -i(g_\mu b\left\langle\sigma_+\right\rangle - g_\mu^* b^*\left\langle\sigma_-\right\rangle) - \gamma(2N+1)\rho_{22} + \gamma N \tag{A.11}$$

To solve this we will need the equations of motion for the coherences $\langle\sigma_+\rangle$ and $\langle\sigma_-\rangle$

$$\dot{\langle\sigma_+\rangle} = \frac{\mathrm{d}}{\mathrm{d}t}\mathrm{Tr}(\rho\sigma_+) = -i\mathrm{Tr}(g_\mu^* b^*\sigma_-\rho\sigma_+ - g_\mu^* b^*\rho\sigma_-) \tag{A.12}$$

$$+\frac{\gamma}{2}(N+1)\mathrm{Tr}(-\rho\sigma_+\sigma_-\sigma_+) + \frac{\gamma}{2}N\mathrm{Tr}(-\sigma_-\sigma_+\rho\sigma_+) \tag{A.13}$$

$$= -ig_\mu^* b^*(\left\langle\sigma_+\sigma_-\right\rangle - \left\langle\sigma_-\sigma_+\right\rangle) - \frac{\gamma}{2}(2N+1)\left\langle\sigma_+\right\rangle \tag{A.14}$$

And likewise, because $\sigma_- = \sigma_+^\dagger$,

$$\dot{\langle\sigma_-\rangle} = ig_\mu b(\left\langle\sigma_-\sigma_+\right\rangle - \left\langle\sigma_+\sigma_-\right\rangle) - \frac{\gamma}{2}(2N+1)\left\langle\sigma_-\right\rangle \tag{A.15}$$

These can be written using the density matrix terms from Equation A.10,

$$\dot{\langle\sigma_+\rangle} = -ig_\mu^* b^*(2\rho_{22}-1) - \frac{\gamma}{2}(2N+1)\left\langle\sigma_+\right\rangle \tag{A.16}$$

$$\dot{\langle\sigma_-\rangle} = +ig_\mu b(2\rho_{22}-1) - \frac{\gamma}{2}(2N+1)\left\langle\sigma_-\right\rangle \tag{A.17}$$

We down take the derivative of Equation A.11, and substitute in Equation A.16

$$\begin{aligned}
\ddot{\rho_{22}} &= -i(g_\mu b\dot{\langle\sigma_+\rangle} - g_\mu^* b^*\dot{\langle\sigma_-\rangle}) - \gamma(N+1)\dot{\rho_{22}} \\
&= -i(-i|g_\mu b|^2(2\rho_{22}-1) - g_\mu b\frac{\gamma}{2}(2N+1)\left\langle\sigma_+\right\rangle) \\
&\quad + i(i|g_\mu b|^2(2\rho_{22}-1) - g_\mu^* b^*\frac{\gamma}{2}(2N+1)\left\langle\sigma_-\right\rangle) \\
&\quad - \gamma(2N+1)\dot{\rho_{22}} \\
&= -2|\Omega_\mu|^2(2\rho_{22}-1) + i\frac{\gamma}{2}(2N+1)(g_\mu b\left\langle\sigma_+\right\rangle - g_\mu^* b^*\left\langle\sigma_-\right\rangle) - \gamma(2N+1)\dot{\rho_{22}}
\end{aligned}$$

Where $|\Omega_\mu|^2 = |g_\mu b|^2$. We can now rearrange Equation A.11 to

$$i(g_\mu b \langle\sigma_+\rangle - g_\mu^* b^* \langle\sigma_-\rangle) = -\dot{\rho_{22}} - \gamma(2N+1)\rho_{22} + \gamma N$$

and substitute it in to find the equation of motion for ρ_{22} in terms only of derivatives of ρ_{22},

$$\ddot{\rho_{22}} = -\frac{3}{2}\gamma(2N+1)\dot{\rho_{22}} - \left(4|\Omega_\mu|^2 + \frac{\gamma^2}{2}(2N+1)^2\right)\rho_{22} + 2|\Omega_\mu|^2 + \frac{\gamma^2}{2}N(2N+1) \tag{A.18}$$

In steady state, where $\ddot{\rho_{22}} = \dot{\rho_{22}} = 0$, the excited state population is

$$\rho_{22} = \frac{2|\Omega_\mu|^2 + \frac{\gamma^2}{2}N(2N+1)}{4|\Omega_\mu|^2 + \frac{\gamma^2}{2}(2N+1)^2} \tag{A.19}$$

The effective population fraction of the ground state is given by $\rho_{11} - \rho_{22}$, due to normalisation this can be written as,

$$\rho_{11} - \rho_{22} = 1 - 2\rho_{22} \tag{A.20}$$

which is,

$$\rho_{11} - \rho_{22} = \frac{\frac{\gamma^2}{2}(2N+1)}{4|\Omega_\mu|^2 + \frac{\gamma^2}{2}(2N+1)^2} \tag{A.21}$$

As a check, when there is no microwave field interacting with the atom $|\Omega_\mu|^2 = 0$, by substituting in for N this reduces to the exact result from the Boltzmann distribution. And also for high microwave field, this drives atoms into the excited state, reducing the effective number of atoms. This function is strictly bounded between 0 and 1, at $|\Omega_\mu|^2 = N = 0$, $\rho_{11} - \rho_{22} = 1$, and for as either or both $|\Omega_\mu|^2,\ N \to \infty$, then $\rho_{11} - \rho_{22} = 0$.

Appendix B

Adiabatic Atomic Interaction Parameter

In the adiabatic approximation model the interactions between the atoms and the cavity fields are characterised by the parameter S,

$$S = \sum_k \frac{\Omega_k g_{\mu,k} g^*_{o,k}}{(\delta_{ao,k} - \delta_{o,k})(\delta_{a\mu,k} - \delta_{\mu,k})} \tag{B.1}$$

Like the S_{13} and S_{12} terms in the full model this is a sum over all the different atoms. As with the full model we can approximate the sum as an integral over the inhomogeneous broadening of the microwave and optical atomic transitions.

$$S = \Omega g_o g_\mu \int d\delta_{ao} d\delta_{a\mu} \frac{G_o(\delta_{ao}) G_\mu(\delta_{a\mu})}{(\delta_{ao} - \delta_o)(\delta_{a\mu} - \delta_\mu)} \tag{B.2}$$

Assuming the inhomogeneous broadening is given by Gaussian distributions for each transition ($G_o(\delta_{ao})$ and $G_\mu(\delta_{a\mu})$), this becomes

$$S = \Omega g_o g_\mu \int \frac{G_o(\delta_{ao}) d\delta_{ao}}{(\delta_{ao} - \delta_o)} \int \frac{G_\mu(\delta_{a\mu}) d\delta_{a\mu}}{(\delta_{a\mu} - \delta_\mu)} \tag{B.3}$$

$$= \frac{\Omega g_o g_\mu}{2\pi\sigma_o\sigma_\mu} \int \frac{\exp\left(\frac{-(\delta_{ao}-\mu_o)^2}{2\sigma_o^2}\right)}{(\delta_{ao} - \delta_o)} d\delta_{ao} \int \frac{\exp\left(\frac{-(\delta_{a\mu}-\mu_\mu)^2}{2\sigma_\mu^2}\right)}{(\delta_{a\mu} - \delta_\mu)} d\delta_{a\mu} \tag{B.4}$$

These integrals diverge due to singularities at $\delta_{ao} = \delta_o$ and $\delta_{a\mu} = \delta_\mu$, however if input fields are sufficiently detuned from the atomic transitions,

$$|\mu_\mu - \delta_{a\mu}| \gg \sigma_\mu \tag{B.5a}$$

$$|\mu_o - \delta_{ao}| \gg \sigma_o \tag{B.5b}$$

then we can integrate over a finite region of the inhomogeneous broadening distributions (Figure B.1). These regions are $[\mu_\mu - 5\sigma_\mu, \mu_\mu + 5\sigma_\mu]$ and $[\mu_o - 5\sigma_o, \mu_o + 5\sigma_o]$ for the microwave and optical integrals respectively.

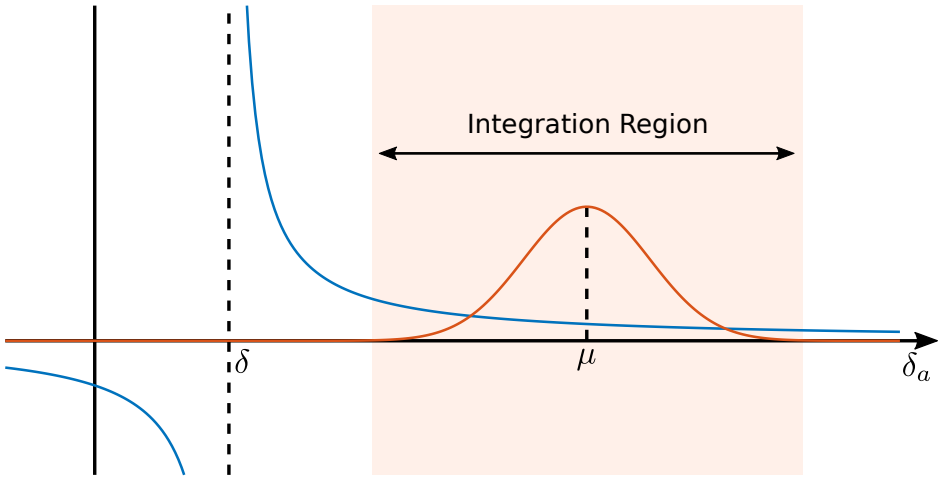

Figure B.1: Diagram demonstrating the integration for the optical or microwave integrals in Equation B.4. For the microwave integral δ in the diagram refers to the input frequency δ_μ, μ refers to the centre of the inhomogeneous distribution μ_μ, and δ_a refers to the atomic detuning $\delta_{a\mu}$; and likewise for the optical parameters. The orange Gaussian represents the inhomogeneous distribution of the atoms, and the blue hyperbola is related to the interaction between the single atom and the cavity field. The integration region is chosen to include almost all of the inhomogeneous line, without diverging due to the singularity at δ.